



ScuDo
Scuola di Dottorato - Doctoral School
WHAT YOU ARE, TAKES YOU FAR



Doctoral Dissertation
Doctoral Program in Materials Science (32.th cycle)

Magnetization dynamics and spintronics of soft magnetic thin films

Gabriel Soares

* * * * *

Supervisors

Prof. Dr. Milena Salvo, Supervisor
Dr. Massimo Pasquale, Supervisor
Dr. Felipe Garcia-Sanchez, Co-supervisor

Doctoral Examination Committee:

Prof. Dr. Hans W. Schumacher, Referee, Physikalisch-Technische Bundesanstalt, Germany
Prof. Dr. Giovanni Carlotti, Referee, Università degli Studi di Perugia, Italy

Politecnico di Torino
July, 2020

This thesis is licensed under a Creative Commons License, Attribution - Noncommercial-NoDerivative Works 4.0 International: see www.creativecommons.org. The text may be reproduced for non-commercial purposes, provided that credit is given to the original author.

I hereby declare that, the contents and organisation of this dissertation constitute my own original work and does not compromise in any way the rights of third parties, including those relating to the security of personal data.

.....
Gabriel Soares
Turin, July, 2020

Summary

Two main topics were discussed in this Phd thesis. a) An experimental part concerning the characterization of soft magnetic thin films by ferromagnetic resonance (FMR) and b) a theoretical part, where numerical simulations of the magnetization inversion of thin films by a spin polarized current were performed.

a) In the case of ultra thin films (a few nanometers) the broadband ferromagnetic resonance experiment has a limited sensitivity, since the absorption is only a small part of measured signal, and depends directly on the volume of the sample. An interferometer setup was implemented, in order to circumvent this problem. The FMR interferometer with two identical diode detectors and a lock-in amplifier was implemented. The experimental signal-to-noise ratio was improved two to three times in comparison to standard state-of-the-art vector network analyzer based experiments. The experiment worked for thicknesses down to 3 nm of Py with in plane anisotropy, but was not able to successfully identify absorptions in ultra thin films (< 2 nm) with perpendicular anisotropy.

Amorphous FeSiB thin films presenting magnetostriction have been investigated for decades for energy and sensors applications. They are very soft magnetic films, with high magnetization saturation. The magnetic properties of those films can be tuned by thermal annealing, releasing the quenched-in stresses. There have been just a few reports in the literature about the microwave dynamic magnetic properties on these films. $Fe_{78}Si_9B_{13}$ thin films with 80 to 300 nm thickness progressively annealed from 200°C to 325°C were characterized by FMR. These materials possess a notable state exhibiting stripe domains regime, where several absorption modes were found, and this peculiar domain configuration was investigated in detail with experiments and micromagnetic simulations to evaluate the possibility of using these films for magnonic applications. The Magnetization saturation obtained was $M_s = 1.65$ T and the magneto-elastic energy could not be exactly quantified due to accuracy issues, but was in close to already published results by our group. The Gilbert damping was found between 1.5 and 2.7×10^{-3} , which is surprisingly low for amorphous thin films. The microwave oscillation modes observed in a specific magnetic configuration exhibiting stripe domains were identified by micromagnetic simulations.

b) Recently Field free switching of magnetic nano elements by spin polarized current have been achieved experimentally. The spin current is generated due to an electric

current passing through a heavy metal underlayer by spin Hall effect. This is very promising for spintronic applications, such as magnetic random access memories. In order to obtain the switching in perpendicular anisotropy films, the energy symmetry of the system needs to be broken spatially. The symmetry of the system can be broken mainly in two ways: either by introducing a tilt in the anisotropy axis or by applying an external bias field using a heavy metal antiferromagnet such as IrMn or PtMn. In this thesis a comparison is presented between the two methods, done both analytically and by macrospin simulations. We have shown that the energy barrier is degraded by the use of a bias field, and thus the tilt method has more potential for minimization and faster operation speed.

Acknowledgements

I would like to thank my supervisors, Massimo Pasquale , Felipe Garcia-Sanchez, and Milena Salvo, for everything they taught me, the patience and the great opportunity that has been going through the the doctorate program. I would also like to thank my laboratory colleagues: Sola, Magni, Michaela, Gianfranco, Fausto, Carmen, Vittorio, Arianna, Elena, Luca, Enzo, Cinzia ,Appino, Ragusa, Bashkar, Daniele, Paola, Marco, Mohammad, Carlo, Federica, Gabriele for all the discussions and support, making my stay in Turin and INRIM such a wonderful and fruitful experience.

And I would like to acknowledge Mark Bieler and Sibylle Sievers for the supervision at PTB Braunschweig, and my colleagues Hans, Jantje, Alexander, Cristoph, Carl, Paul, Manuela and Baha for all the discussions and leisure time (beers!) while I was in Germany.

I am also very grateful to my flatmates Ylenia, Manuela, Cristina and Gabriele, for their caring friendship for all these PhD years. To the folk dancing community in Turin, and to the Squadra Corse C. Artigiana, for introducing me to two great passions: dancing and cycling in the alps. And finally to Fabio, Luca ,uncle Ivo and the whole veneto gang, for all the the alcohol they drowned me in the vacations.

The work here presented was supported by the following grants: EMPIR-NANOMAG, EMPIR-TOPS 17FUN08-RMG1 and Quantumet.

Contents

List of Tables	IX
List of Figures	X
1 Introduction	1
2 Magnetization Dynamics	5
2.1 Introduction	5
2.2 Angular momentum and spin	5
2.3 Magnetic Free energy	9
2.3.1 Demagnetizing field and shape anisotropy	11
2.3.2 Exchange energy	15
2.4 Magnetic damping	16
2.5 Uniform precession and Ferromagnetic resonance	17
2.5.1 Magnetic susceptibility at the resonance	18
2.5.2 Smith-Beljers Formula	20
2.5.3 Uniaxial anisotropy solution	21
2.6 Spin transfer torques	22
3 Experimental Methods	27
3.1 Ferromagnetic resonance experiment	27
3.1.1 Measurement of the FMR in broadband frequencies	28
3.2 Magnetic constants extraction	37
3.3 Interferometric BBFMR techniques	42
3.3.1 Lock-in type interferometer	43
4 Amorphous FeSiB dynamics	53
4.1 Introduction	53
4.1.1 Fe-Si-B amorphous alloys	55
4.2 FeSiB Ferromagnetic Resonance	58
4.2.1 Analysis of FMR results	58
4.2.2 Broadband-FMR characterization	60

4.2.3	Discussion	61
4.2.4	Error Propagation	66
4.3	Micromagnetic Simulations	67
4.3.1	Mumax3 simulation parameters	69
4.3.2	Simulation Procedures	70
4.3.3	Results and Discussion	71
4.4	Conclusion and future perspectives	74
5	Field Free switching spintronic devices	75
5.1	Introduction	75
5.1.1	Magnetic recording devices	75
5.1.2	Spin orbit torques devices	76
5.2	Energy barrier modeling	78
5.2.1	Equilibrium positions	79
5.2.2	Energy barriers of the two systems	80
5.3	Critical currents	83
5.3.1	Anisotropy tilt case	84
5.3.2	Bias case	86
5.3.3	SOT switching efficiency	87
5.4	Switching dependence on pulse duration	88
5.5	Conclusions	90
6	Final Remarks	91
	Bibliography	93

List of Tables

3.1	Relevant resonance parameters obtained from Magnetic susceptibility fit.	39
3.2	Magnetic parameters obtained from the 20 nm Py fit.	40
4.1	Parameters obtained from the peak fit of the 230 nm thick sample at 12 GHz	61
4.2	Summary of the magnetic anisotropy and damping constants obtained from the Broadband FMR experiments. The uncertainties are an indication of the quality of the fit, and not of the constant value itself. The plots are presented in Figs. 4.8 and 4.9	63

List of Figures

2.1	The precession of a magnetic moment as an analogue of a rapidly spinning top. a) The spinning top vectors and torque. b) magnetic moment suffering a torque from the effective field.	7
2.2	Vector scheme with the added damping torque.	8
2.3	Spherical coordinates as a function of the magnetization direction \vec{M}	10
2.4	Vector scheme for the integration of the demagnetizing field of a generic magnetic sample.	11
2.5	\vec{H}_d the demagnetizing field of a generic magnetic sample.	12
2.6	Illustration of the magnetostriction effect. Since the atoms are not completely spherical, the applied magnetic field changes the electron cloud distribution due to the spin orbit coupling, and a change in the dimension of the material can be observed.	15
2.7	Centered and normalized resonance plot of the real (χ'_+) and imaginary (χ''_+) susceptibility components as a function of frequency. The vertical lines are highlighting the FWHM and its relationship between the imaginary and real components.	19
2.8	Normalized resonance frequency as a function of IP and OOP static fields. Plots 1 and 2 with IP static field; 3 e 4 with OOP; $K_{eff} < 0$ e $K_{eff} > 0$ respectively.	22
2.9	Spin transfer torque added vector scheme on the LLG equation.	24
2.10	Spin transfer torque induced oscillator. The field like torque b_j is set to zero, and the damping like a_j is set to compensate the Gilbert damping. Hard axis on \hat{z} direction. No external field applied, only a current.	25
2.11	Final magnetization as a function of the STT induced torques. $b_j = -a_j$, in red decreasing from positive to negative, in blue otherwise. Hard axis on \hat{z} direction. No external field applied.	26
3.1	Coplanar waveguide cross-section illustration. Excitation field shown by h_{rf}	29
3.2	Experimental schematics of the BFMR with the VNA.	30
3.3	scheme with a_j/b_j waves	31

3.4	Comparison between different subtraction methods with the same dataset. Py 20 nm. a) Substraction of a reference in a frequency sweep. The reference and measurement field are respectively 74 mT and 250 mT. b) Converting the subtracted frequency sweep data for a field sweep dataset.	34
3.5	Lock-in-BFMR schematics.	35
3.6	Scheme of the amplitude modulation generating and reading process. The carrier microwave can be seen at a), the combined RF AM modulation and carrier wave at b) and finally the rectified signal by the diode at c). The lock-in then reads the average of the signal, namely the V_{RMS} . Thus, any change in the amplitude of the carrier microwave will reflect directly on a change on V_{RMS} .	36
3.7	Color plot of the uncalibrated permeability $U''(H, f)$. Colors are amplitude in dbs. It is highlighted the origin of the applied field, indicating a slight offset in the measured field.	37
3.8	Rotation of the magnetic susceptibility complex plane observed experimentally.	38
3.9	Example of non-linear fit of a 9 GHz slice of uncalibrated permeability $U(f,H)$ for a 20 nm Py thin film. The real part is shown in black and the imaginary part in red.	39
3.10	Py 20 nm final non-linear fits for obtaining the magnetic parameters.	41
3.11	Scheme of the Lock-in based interferometric BFMR experiment. The conections in purple are done by u.h.f(GHz) cables and conectors, while the ones in black with standard RF (KHz)	43
3.12	L-pad type attenuator. The ideal potentiometer to be used is a multiturn, to allow a more precise control of the resistance.	44
3.13	a) Point probe station. b) 20 nm thick Py stripes with varying widths. Numbers are in mm.	45
3.14	Comparison between measuring only the sample arm (Ch A) against the subtraction from the reference arm (Ch A-B). Py sample width of 0.5 mm.	45
3.15	Effect of decreasing the width of the stripe in contact with the CPW. No signal at 0.25 mm	46
3.16		47
3.17	a) Photo of the actual setup inside the electromagnet. b) Southwest connectors input loss.	48
3.18	5 GHz spectra of 3 nm thick Py film. a) Lock-in interferometer. b) VNA Rode-Schwarz	49
4.1	Hysteresis curves for a) different film thicknesses and b) different annealing temperatures (60 min) on the 230 nm thick sample.	57
4.2	Diagram of the expected domain profile in a cross section of the FeSiB film at remanence, in the presence of stripe domains with alternating OOP magnetization.	57

4.3	Series of FMR absorption peaks measured from 2 to 6 GHz on the t=230 nm sample. From left to right, top to bottom: annealing temperatures= 200, 225, 250, 275, 300, 325 °C.	59
4.4	Temperature plot of the FMR spectra for the 230 nm thick film with 200 ⁰ C. The square root law of the frequency dispersion shown is typical of films with a dominant in-plane dominant anisotropy component.	60
4.5	Non-linear fit of the resonances for the 230 nm thick film with 200 ⁰ C. Fixed $\gamma/2\pi = 29.25$ GHz/T and $\mu_0 H_a = 1.582 \pm 0.003$ T	61
4.6	Non-linear fit (Eq. 2.53) of the resonances for the 230 nm thick film with 200 ⁰ C. Fixed $\gamma/2\pi = 29.25$ GHz/T and the output $\mu_0 H_a = 1.582 \pm 0.003$ T	62
4.7	Non-linear fit of the linewidths for the 230 nm thick film with 200 ⁰ C. Fixed $\gamma/2\pi = 29.25$ GHz/T, $\mu_0 \Delta H_0 = 4 \pm 1$ mT and $\alpha = 2.9 \pm 0.2 \times 10^{-3}$	62
4.8	Summary of the obtained anisotropy field values for all the samples. The error was propagated for $\Delta H_{res} = 2\%$	65
4.9	Summary of the obtained intrinsic damping values found for all the samples. They were corrected for the capacitive coupling between the sample and the CPW	66
4.10	Propagated uncertainty in the anisotropy field $\mu \Delta H_a$ as a function of a) the resonance frequency f_{res} and b) the uncertainty of the resonance field $\mu_0 \Delta H_{res}$	68
4.11	Change in the demagnetizing factor as a function of the ratio of width to thickness. $n_c = 1$ in the ideal oblate ellipsoid. 250 PBC gives around $n_c = 0.999$	70
4.12	a) Cross section of the 150 nm thick film with the domain structure simulated at remanence. The yellow arrows indicate the magnetization direction. The stripe domains have a magnetization that points in the out-of-plane direction only in the center of the domain (red and blue areas) and then becomes parallel to the film surface. b) Hysteresis curves. Orange is the experimental data, and blue the simulated one. Both have a transcritical shape, with the remanence and saturation field closely matched.	72
4.13	Temperature plot of the dynamics simulation of the t=150 nm film with applied field up to 20 mT. Multiple FMR modes are observed at low applied field.	73
4.14	Slice of frequency modes at 10mT (simulation) and 3 mT (experimental).	73
4.15	Cross section of the temporal progression of a half a period for a) 2.34 GHz and b) 4.15 GHz. c) Vector directions for reference.	74

5.1	(a) Vector diagram of the bias case and (b) tilt case. The anisotropy tilt angle is in the yz plane for the tilt case. Energy landscape for (c) Perpendicular anisotropy, (d) Bias case and (e) Tilt case. In the graphs, the blue color is the minimum value and red is the maximum value. The magnetization may switch if the applied current is sufficient to traverse the separatrix line plotted in green. Energy-conserving trajectories are shown in black.	79
5.2	Energy barrier for coherent rotation and domain wall nucleation as a function of the exchange-bias field.	81
5.3	OOP magnetization map (m_z color coded) with different b_j values $b_j = a_j$; $b_j = 0$; $b_j = -a_j$ as a function of the intensity a_j of a current pulse lasting t_p : from a) to c) m_z is the bias case as a function of the bias in plane field (H_X) at the end of current pulse time $t_p = 100ns$, d) to f) the relaxed m_z for the bias case after 100 ns ($t = 2 * t_p$) upon removal of the current pulse; g) to i) Anisotropy tilt case as a function of the anisotropy tilt angle β at the end of current pulse time $t_p = 100ns$, j) to l) the relaxed m_z for the tilt case after 100 ns ($t = 2 * t_p$) upon removal of the current pulse;. Column-wise we observe the effect of the field-like torque b_j in the systems.	85
5.4	Simulation of the magnetization trajectory for field free switching with $a_j = -10$ mT and $b_j = -a_j$. Black arrow indicates the initial state, blue lines and dots dynamics with the current pulse and red lines and dots the relaxation upon removing of the current. a) Tilt case, $\beta = 3.5^\circ$. b) Bias case, $H_X = -10$ mT.	86
5.5	Figure of merit $a_{j,c}/E_B$ for (a) Tilt case as a function of the tilt angle β and (b) Bias case as function of the bias field H_X	88
5.6	SOT switching in the tilt case for different pulse duration t_p as a function of tilt angle β for (a) field-torque equal to damping-torque $b_j = a_j$ (b) no field-like torque $b_j = 0$ (c) and inverted sign between torques $b_j = -a_j$. In the next row, SOT switching in the bias case for different pulse duration t_p as a function of the bias field H_x for (d) field-torque equal to damping-torque $b_j = a_j$ (e) no field-like torque $b_j = 0$ (f) and inverted sign between torques $b_j = -a_j$. Black dot means switched state and white dot not switched.	89

Chapter 1

Introduction

Magnetic phenomena have been a subject of study since ancient past, since the discovery of the lodestone attracting pieces of iron. Modern magnetism started with William Gilbert, with his treaty *De Magnet* in 1600, where, to explain the behavior of compasses he proposed the Earth to be a magnet itself[1]. From the 1820s onward, the relationship between electricity and magnetism began to be investigated, and these investigations culminated with Maxwell's equations at the end of the century. Since then, magnetism, electricity and optics were unified in the electromagnetic field.

All materials respond to an external magnetic field, albeit in a different manner. Materials can then be classified depending on their response to a magnetic field.

Diamagnetism occurs when the electron cloud of the material is repelled by Faraday's law due to the magnetic field, and the resulting magnetic moment is in the direction opposite to the field. All materials are Diamagnetic, but the effect is usually small as long the external field is not abnormally large.

Paramagnetism is present in many metals and oxides, where the spin of uncoupled electrons is free to align with the magnetic field. The effect is stronger than Diamagnetism, but smaller than the thermal agitation at room temperature, and thus is only seen in the presence of an external magnetic field.

Ferromagnetism and Antiferromagnetism, on the other hand, are present even in the absence of an external field. They derive from the Heisenberg interaction, which aligns neighboring free electron spins either parallel or anti-parallel. For Ferromagnetism, the interaction is strong in transition metals with an incomplete 3d shell, more specifically Iron, Nickel and Cobalt; and in rare earths with an incomplete 4s shell such as Gadolinium. These phenomena are irreversible, meaning that once a sample is magnetized it will remain magnetized even in the absence of an external magnetic field. The lodestone mentioned in the first paragraph, is a ferromagnetic material¹.

¹Actually a ferrimagnetic material, pertaining to a subgroup of ferromagnetic materials

Ferromagnetic materials are widely used in a range of applications: sensors, actuators, transformer cores, inductors and for data storage. The dimension of ferromagnetic materials influences directly in their magnetic properties, and in the past decades research has been focused on nanometer scale magnets. Two relevant applications of nanosized thin films are the data storage disk and read-out sensors of hard drives. Giant magnetoresistance allowed to read smaller and smaller data elements through electric signals, and opened the whole new field of spintronics.

Spintronics relates to several phenomena connecting spin polarized currents and magnetism - and it was verified that it is possible to switch magnetization of a magnetic element through a spin current even in the absence of an external magnetic field.

The original work that was carried out in this thesis is divided in two major parts: the first part is devoted to the characterization of amorphous FeSiB ferromagnetic thin films including their interesting microwave properties; the second part is related to spintronics, the comparison by simulation of two field-free switching magnetization methods. In both parts, all the physics employed was already available and well established, and my original contribution to the research is associated to the study of the magnetic and the spintronic behavior of specific materials, for possible high relevance technology applications. The first chapter is the introduction. The second chapter covers the fundamentals of dynamics of magnetization used throughout the text. Magnetization dynamics are described using an analogy with a spinning top. The description starts from the Landau-Lifshitz-Gilbert equation and its solution for the uniform precession mode, or the ferromagnetic resonance. The ferromagnetic resonance is a well understood phenomenon that can be used to obtain certain magnetic properties of materials, such as the anisotropy and losses. A detailed description of the underlying magnetic phenomena necessary to model experimental cases is described, together with the specific solution for uniaxial anisotropy thin films. Finally, the Landau-Lifshitz-Gilbert-Slonczewski equation is presented, with the added torques caused by a spin current, of specific relevance to the field of spintronics.

The third chapter covers experimental methods used in this thesis, and concerning the ferromagnetic resonance. In the first part the experimental setups and data analysis fittings procedures are detailed, together with their limitations. In the second part an attempt is presented to implement an improvement of the experimental setup using interferometry techniques.

The fourth chapter covers the characterization of amorphous FeSiB thin films. The thin films present stresses quenched-in during deposition, which influence their magnetic properties. Further thermal treatments at different temperatures progressively released the internal stresses. Ferromagnetic resonance was used to characterize these films and their stress, and the analysis was supported by micromagnetic simulations.

The fifth chapter is related to the theoretical background. It is the comparison between two families of methods to attain the switching of a ferromagnetic layer in the absence of an external magnetic field. We show that the switching is possible by exploiting the spin polarization of an electric current passing through an adjacent heavy

metal layer. However, the energy barrier landscape symmetry of the system needs to be broken to successfully complete the switching on a thin film with perpendicular anisotropy. This is done either by introducing a fixed bias field from one of the layers, or tilting the anisotropy axis by a few degrees. The investigation was done both analytically - to understand the energy landscapes - and numerically - to observe the trajectories taken by the magnetization. Both results are then combined for the comparison.

Chapter 2

Magnetization Dynamics

2.1 Introduction

Magnetization dynamics investigates how the trajectory of the magnetization evolves in time. It is of great importance, being used from the understanding of several complex magnetic phenomena to characterize materials. This chapter lays the groundwork of physical concepts used for both the experimental and simulation procedures in this thesis.

The chapter starts with an introduction of the Landau-Lifshitz-Gilbert equation, an analogous equation to a spinning top, and the main equation in the field. It then follows to the description of magnetic energies and their connection to the effective field. Ferromagnetic Resonance is described and how to obtain a general equation to each specific case defining the magnetic energies of interest. This general equation is then used to describe the uniaxial anisotropy case, which is commonly used in thin film and extensively in this thesis.

Last, the Landau-Lifshitz-Gilbert-Slonczewski equation is described, of interest to the subfield of spintronics. It is the same as the Landau-Lifshitz-Gilbert equation, except of two additional terms related to the change of magnetization by a spin current.

2.2 Angular momentum and spin

Being a fundamental particle, the electron has its physics governed by quantum mechanics. It is thus considered a one dimensional point in space, with two properties: electric charge and spin. The electric charge properties and its consequences are well explained by the classical Maxwell equations, from electrical currents to generation of magnetic fields and electromagnetic waves. However, the spin, i.e., its intrinsic magnetic moment, cannot be directly explained by classical physics.

The first direct experimental observation of the spin, the Stern-Gerlach experiment [2, 3], is one of the stepping stones of the development of the quantum mechanics. The experiment consisted in sending a beam of silver atoms through a gradient of magnetic field - they were then deflected and concentrated in two discrete points, either up or down. Initially, the experiment was developed to verify the hypothesis from the Bohr-Sommerfeld model that the orbital angular momentum of silver atoms were quantized, since by the classical model a continuous of points should be detected. In reality though, it not only invalidated the classical mechanics but also created problems for the Sommerfeld model - which predicted 3 points of deflection. They were solved after the introduction of the concept of a spinning electron, by George Uhlenbeck and Samuel Goudsmit and it was later modeled by Pauli [4].

Fundamental particles then have an intrinsic property analog to an angular momentum. It is as if they "spin" around their axis, albeit being one dimensional objects. The Stern-gerlach experiment can be used to probe also the spin of charged particles (as the electron), as long as there is an electrical field to compensate the deflection by the Lorentz force ¹. The electron then is found to have two values of spin, $\pm 1/2\hbar$, in the direction of the discretization (defined by the inhomogeneous field direction on the experiment).

Ferromagnetism has its roots on the Heisenberg interaction, given by the dot product of two neighboring spins. Electrically non-compensated atoms are then either attracted (ferromagnetism) or repulsed (antiferromagnetism). Thus, one may argue that magnetism is a purely quantum phenomena, and should be treated and dealt as such. However, in materials one is dealing with large amounts of atoms grouped together, that gives birth to spontaneous magnetization which behaves in a continuous way, without quantization. Together with the wave mechanics approach of quantum mechanics, the resultant equations are often inconvenient, happening to be over complicated with the phenomena in question to be studied.

Therefore, a semi-classical approach is used. The idea is of treating the magnetic moments as sums of spins grouped together, and use an analogue of classical newtonian mechanics of motion for rotating rigid bodies. The image is that of a spinning top, precessing due to the force of gravity \vec{F}_g (see Fig.2.1.a). The total torque of the system $\vec{\tau}_{total}$ is equal to the torque caused by the gravity on the rotating body $\vec{\tau}_g$:

$$\vec{\tau}_{total} = \vec{\tau}_g. \quad (2.1)$$

Since $\vec{\tau}_{total}$ is the rate of change in time t of the angular momentum $d\vec{L}/dt$, and the $\vec{\tau}_g$ depends in the lever arm \vec{d} , one gets:

$$\frac{d\vec{L}}{dt} = \vec{d} \times \vec{F}_g. \quad (2.2)$$

¹ $F = q\vec{E} + q\vec{v} \times \vec{B}$

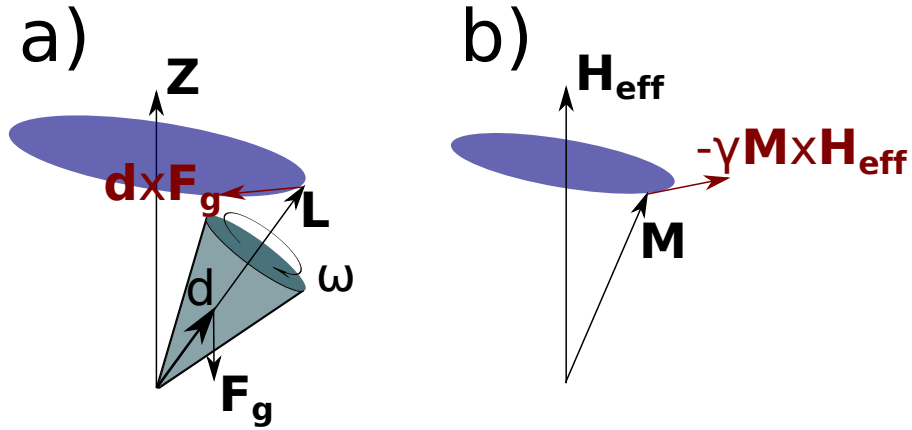


Figure 2.1: The precession of a magnetic moment as an analogue of a rapidly spinning top. a) The spinning top vectors and torque. b) magnetic moment suffering a torque from the effective field.

The spin of an i electron \vec{S}_i is an angular momentum, and their sum the magnetization \vec{M} of the body:

$$\vec{M} = \sum_i \vec{S}_i. \quad (2.3)$$

The torque suffered by such magnetization in an applied field \vec{H}_{eff} ² is comparable to $\vec{\tau}_g$, as long as the ratio between the angular momentum and magnetic moment, i.e. the gyromagnetic ratio γ , is considered (Fig.2.1.b):

$$\frac{d\vec{M}}{dt} = -\gamma\mu_0\vec{M} \times \vec{H}_{eff}. \quad (2.4)$$

The last equation does not agree with experimental observations though. The precession of the magnetization is observed to be a damped oscillation, and thus in Eq.2.4 it is missing a second torque responsible for losses on the system (see Fig.2.2), which was introduced by "hand" by Landau and Lifshitz in 1935 [5]. The Landau-Lifshitz equation is:

$$\frac{d\vec{M}}{dt} = -\gamma\mu_0\vec{M} \times \vec{H}_{eff} - \frac{\lambda}{M_s^2}\vec{M} \times (\vec{M} \times \vec{H}_{eff}), \quad (2.5)$$

where λ is a phenomenological damping parameter and M_s the saturation magnetization.

²In ferromagnetic materials, the magnetization suffers the torque from the external applied field and its own generated field. This effective field is denoted by \vec{H}_{eff} , and will be dealt with in the following sections.

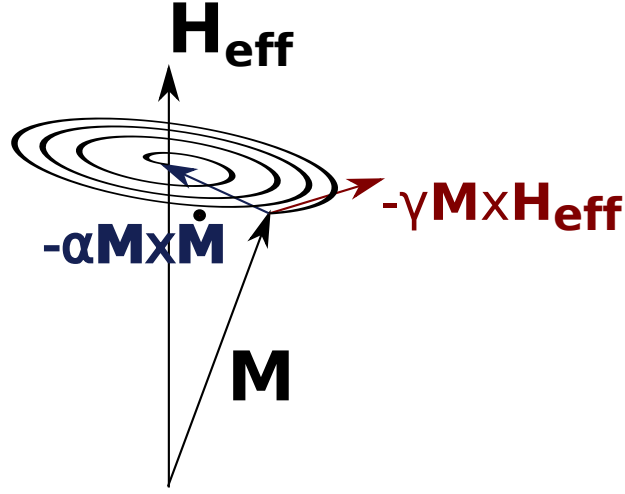


Figure 2.2: Vector scheme with the added damping torque.

However, the Landau-Lifshitz equation does not properly work for larger magnetic dampings, causing a slight mismatch between experiments and theory in these cases. To solve this, Gilbert in 1955 [6] proposed a time-dependent term, and justified it through Lagrangian equations of motion. Known as the Landau-Lifshitz-Gilbert equation, it is given by:

$$\frac{d\vec{M}}{dt} = -\gamma(1 + \alpha^2)\mu_0\vec{M} \times \vec{H}_{eff} - \frac{\alpha}{M_s}\vec{M} \times \frac{d\vec{M}}{dt}, \quad (2.6)$$

where \vec{M}_s is the saturation magnetization, α is the Gilbert damping and \vec{H}_{eff} is the effective field felt by the magnetization:

$$\vec{H}_{eff} = -\frac{1}{\mu_0}\nabla_{\vec{M}}F(\vec{M}), \quad (2.7)$$

where F is the magnetic free energy density of the system.

Both equations are equivalent, with the following relation:

$$\alpha = \frac{\lambda}{\gamma M_s}, \quad (2.8)$$

$$\gamma^* = (1 + \alpha^2)\gamma. \quad (2.9)$$

The largest damping α observed in the 1950s was of about 0.1, and as such the $(1 + \alpha^2)$ correction is about 1%. In this thesis, all dampings are smaller than 0.01, and the correction on γ will not be considered.

The LLG equation is non-linear, meaning there is no universal analytical solution. However, there are analytical solutions to specific cases, considering the sample completely magnetic saturated with $\vec{M} \approx M_s$, as in the case with the modes of oscillation. The magnetization can precess uniformly (FMR), or not, generating spin waves in analogy to oscillations in a rope. The equation can also be solved numerically, both in a macrospin or micromagnetic approach. In the macrospin approach, the magnetization is considered to be a single unit vector, and the \vec{H}_{eff} terms are introduced as separate fields each generating a different torque. On the other hand, with the micromagnetic approach the magnetic sample is broken into many small regions, solving the LLG for each one of those.

The analytical solution of the ferromagnetic resonance will be presented in the next sections, and it is used for the analysis of the experimental data obtained in this thesis. The micromagnetic and macrospin approaches will be used in chapters 4 and 5 respectively, and will be described in detail there.

2.3 Magnetic Free energy

In a ferromagnetic material, the magnetization suffers a torque not only by the applied external field, but also from internal fields from and the magnetization of neighboring regions. We define the effective field as:

$$\vec{H}_{eff} = -\frac{1}{\mu_0} \nabla_{\vec{M}} F(\vec{M}), \quad (2.10)$$

where F is the magnetic free energy density of the system.

Subjected to their own field generated by its strong magnetization, ferromagnetic materials display several interesting phenomena. They can generate domains with different magnetization directions and magnitudes, anisotropy due to shape and crystalline arrangement, field dependent internal stresses, etc. These effects are mainly a consequence of a complex interplay between the exchange and magnetic dipolar field interactions. Since these phenomena were found experimentally in different specific situations, it is common practice to model them separately. The free magnetic energy terms are:

$$F = F_{Zeeman} + F_s + F_{crys} + F_{m-s} + F_{ex} + F_{DW} \quad (2.11)$$

where:

- F_{Zeeman} : the dipolar energy from the torque of the magnetization with the applied field;
- F_s : the shape anisotropy energy;
- F_{crys} : the crystalline anisotropy energy;

- F_{m-e} : the magnetoelastic energy
- F_{ex} : exchange interaction energy in the spin waves context[7];
- F_{DW} : magnetic domain wall energy.

Each of these terms will be described in the following pages, with emphasis on the terms most important for the chapters 4 and 5. They will all be described in a system of spherical coordinates defined by the magnetization vector (see Fig.2.3)

$$\hat{e}_\rho = \begin{bmatrix} \sin \theta \cos \phi \\ \sin \theta \sin \phi \\ \cos \theta \end{bmatrix}; \quad \hat{e}_\theta = \begin{bmatrix} \cos \theta \cos \phi \\ \cos \theta \sin \phi \\ -\sin \theta \end{bmatrix}; \quad \hat{e}_\phi = \begin{bmatrix} -\sin \phi \\ -\cos \phi \\ 0 \end{bmatrix}; \quad (2.12)$$

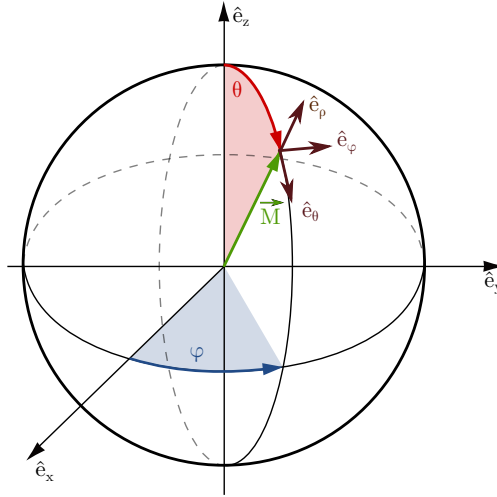


Figure 2.3: Spherical coordinates as a function of the magnetization direction \vec{M}

Zeeman energy

The Zeeman energy is the torque exerted on the magnetization by the applied field. It is at a maximum when the vectors are orthogonal to each other, and minimum when parallel. It is defined as:

$$F_{Zeeman} = -\frac{1}{V} \int_V \vec{M} \cdot \vec{B} dV, \quad (2.13)$$

the magnetic induction $B = \mu_0(H + M)$ gives two terms:

$$F_{Zeeman} = \frac{1}{V} - \mu_0 \int \vec{M} \cdot \vec{H} dV - \mu_0 \int \vec{M} \cdot \vec{M}' dV. \quad (2.14)$$

The first term on the left side of this equation is uniform in the volume as long as the sample is fully magnetized, and the integral is straightforward. The second term, however, depends on the boundary conditions on each sample. It will generate an external field, opposing the change in magnetization known as the demagnetizing field, and it will be described in the following section.

The Zeeman energy in spherical coordinates is:

$$F_{Zeeman} = \mu_0 H M_s (\sin \theta \sin \phi). \quad (2.15)$$

2.3.1 Demagnetizing field and shape anisotropy

The magnetization of a ferromagnetic material is strong enough to interact with itself - generating an internal field which may oppose or help the torque of an external field. Named as the demagnetizing field, it depends on the shape of the material. This effect is a de facto anisotropy: by applying an external field one will need less field to magnetize in the longest direction of the material against the shortest. For example, in a thin film, less field is needed to magnetize in the plane of the sample, against perpendicular to plane.

The demagnetizing field is a consequence of the interaction between the magnetic dipoles inside the material. They compensate each other internally, but accumulate on the boundaries of the material, with the magnetic flux closing on the opposite direction. The consequence is a strong field \vec{H}_d acting to demagnetize the material (see Fig 2.4).

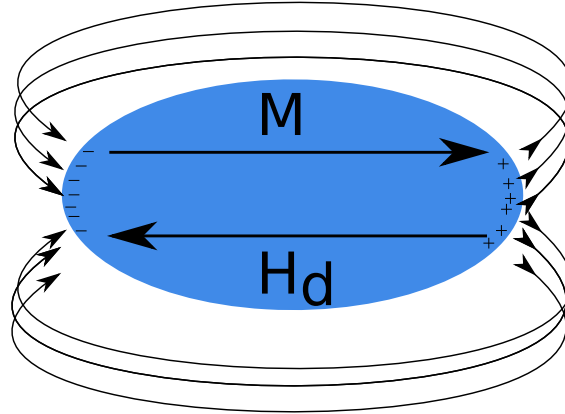


Figure 2.4: Vector scheme for the integration of the demagnetizing field of a generic magnetic sample.

To calculate the demagnetizing field, one needs to integrate the magnetic potential over the surface and volume magnetic charges of a material:

$$\phi_M(\vec{r}) = -\frac{\mu_0}{4\pi} \int_V \nabla' \cdot \frac{\vec{M}(\vec{r}')}{|\vec{r} - \vec{r}'|} dV' + \frac{\mu_0}{4\pi} \oint_S \hat{n} \cdot \frac{\vec{M}(\vec{r}')}{|\vec{r} - \vec{r}'|} dS'. \quad (2.16)$$

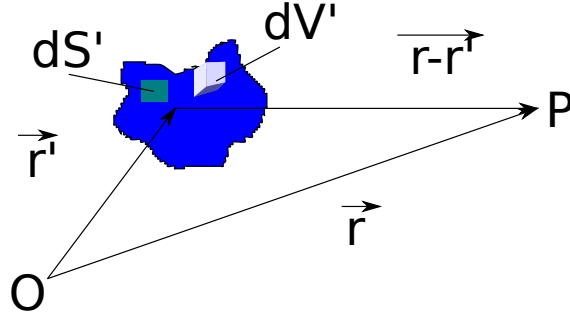


Figure 2.5: \vec{H}_d the demagnetizing field of a generic magnetic sample.

A scheme of the integration vectors can be seen on Fig.2.5. If the sample is fully magnetized in one direction, \vec{M} is uniform in the space and thus $\nabla \cdot \vec{M}(\vec{r}') = 0$, and we are left with:

$$\phi_M(\vec{r}) = \frac{\mu_0}{4\pi} \vec{M} \cdot \oint_S \hat{n} \frac{1}{|\vec{r} - \vec{r}'|} dS', \quad (2.17)$$

where \hat{n} is the unit vector perpendicular to the surface and dS' the surface infinitesimal element.

Now, the demagnetizing field is given by $\vec{H}_d = -\nabla\phi_M$, and will depend uniquely on the geometry of the sample. For an ellipsoidal material we have:

$$\vec{H}_d = -\vec{N}\vec{M}, \quad (2.18)$$

where \vec{N} is the rotational ellipsoid tensor, respecting $N_a + N_b + N_c = 1$:

$$N = \begin{bmatrix} N_a & 0 & 0 \\ 0 & N_b & 0 \\ 0 & 0 & N_c \end{bmatrix}. \quad (2.19)$$

In this thesis, all the samples are thin films, which we approximate with an oblate ellipsoid. Thus, $N_a = N_b = 0$ and $N_c = 1$. Comparing with the Zeeman energy (Eq.2.13), but changing the applied field for the demagnetizing field we have:

$$\begin{aligned} F_s &= -\frac{\mu_0}{2} \vec{M} \cdot \vec{H}_d \\ &= \frac{\mu_0}{2} M_s^2 \cos^2 \theta. \end{aligned} \quad (2.20)$$

Hence, this energy is part of the effective field, accounting for the anisotropy caused by the shape of the sample. In the plane of a thin film $\theta = \pi/2$, and $F_s = 0$. If one now tries to switch to an out-of-plane magnetization, F_s is maximum and the applied field will have to compete against it to switch the magnetization. It is a uniaxial anisotropy,

in the sense that it depends only on θ . This anisotropy energy then works in favor of maintaining the magnetization in the plane of the sample [8]. There are other two forms of anisotropy, one originated from the crystalline structure and the from the internal stresses of the material. In this thesis, the samples we used are either amorphous (FeSiB) or present negligible crystalline anisotropy ($Ni_{20}Fe_{80}$).

Crystalline anisotropy energy

The crystalline lattice influences the preferred magnetization directions in a ferromagnetic material, generating an internal field that acts with or against the applied field depending on the direction of the magnetization. In a crystalline lattice, there are three different couplings possible: spin-spin, spin-lattice and spin-orbit. The spin-spin coupling comes from the Heisenberg interaction and is isotropic, not contributing to the anisotropy.

The spin-lattice coupling comes from the crystalline field. This field is a consequence of the interaction of electric field generated by the uncompensated spins on neighboring atoms, distorting their electric charge distribution. Depending on the element or alloy, it will favor certain structures: e.g. tetragonal, hexagonal and variations. In the case of Iron and Nickel, at room temperature it is found to be cubic, with body centered and face centered respectively. In this cases, the electric cloud of each atom on the vertices is elongated on the direction of the axis of the cube, coupling with the lattice.

Applying a magnetic field, the spins of the uncoupled electrons should be free to align to the field, but the orbital magnetic moments are not. This effect is known as the angular momentum quench. However, the spins are also coupled to their orbits by the spin-orbit coupling. Thus, the applied field needs to overcome the spin orbit coupling from the site, which in turn depends on the lattice directions and symmetry.

The role of the spin-orbit coupling in the crystalline anisotropy are well established, but predictions of its intensity from first principles are seldom reliable. More so, even the spin density in an axis does not corresponds in an easy or hard axis. For example, the highest atomic density direction on a body centered structure (as iron) is [111] and results in a hard magnetization axis, while in face centered structures (as Nickel) is [110], which is a medium hard axis. Therefore, the crystalline anisotropy is treated in a phenomenological fashion, as an expansion of the direction cosines α_1 , α_2 , α_3 from the angles between the magnetization and the cristalline axis, and for a cubic system is:

$$F_{cris} = K_0 + K_1(\alpha_1^2\alpha_2^2 + \alpha_2^2\alpha_3^2 + \alpha_3^2\alpha_1^2) + K_2(\alpha_1^2\alpha_2^2\alpha_3^2), \quad (2.21)$$

where K_0 , K_1 e K_2 are the anisotropy constants. In spherical coordinates, this equation takes the form:

$$F_{cris} = K_0 + K_1\left(\frac{\sin^2 \theta \sin^2 \phi + \cos^2 \theta}{4} + \cos^2 \theta\right) \sin^2 \theta + K_2\left(\frac{\sin^2 2\phi}{16} \sin^2 2\theta\right) \quad (2.22)$$

Another way of writing the energy for a general system is:

$$F_{cris} = K_0 + K_1(\vec{u} \cdot \vec{m})^2 + K_2(\vec{u} \cdot \vec{m})^4 \quad (2.23)$$

where \vec{u} and \vec{m} are direction unitary vectors of the crystalline axis and the magnetization respectively. Thus, an hexagonal close packed system like Co, the anisotropy takes the form of a uniaxial one:

$$F_{cris} = K_0 + K_1 \sin^2 \theta + K_2 \sin^4 \theta \quad (2.24)$$

Magnetoelastic energy

The strain of a material is defined by $\lambda = \Delta l/l$, where Δl is the variation and l is the length. When a material is exposed to a magnetic field, the alignment of its magnetic moments and/or electron clouds generate a strain, called magnetostriction (see Fig.2.6). It is a weak effect, often neglected. Ferromagnets with strong magnetization, however, may present strains of the order of 10^{-5} and compared to the thermal expansion coefficient in typical metals and alloys ($\approx 2 \times 10^{-7}$ 1/K), this strain would be equivalent to the expansion due to 0.5 K [8], which is still relatively small, but combined with stress may have important consequences in the magnetic permeability and magnetization behavior.

The origin of magnetostriction is the spin-orbit interaction and the non spherical shape of the atoms due to the electron cloud distribution. The first ties the atoms to a crystalline structure, and the second may generate a strain depending on their physical orientation at their sites inside the structure. In the case of a cubic crystalline structure, such as iron, the [100] directions (edges of the cube) expand when the material is magnetized in these directions. This fact means that the material is longer on the direction of [100], and not perfectly cubic as the X-ray crystallography results show.

FM materials often are polycrystalline, meaning they are composed with a variety of randomly oriented crystalline grains. However, deposition conditions often favor a preferred orientation of these grains, or a texture. The magnetostriction is then given by λ_θ as a function of the angle between the strain and magnetization direction (θ) is [8]:

$$\lambda_\theta = \frac{3}{2} \lambda_p (\cos^2 \theta - \frac{1}{3}) \quad (2.25)$$

where λ_p is the magnetostriction polycrystalline constant. Typical values are -7×10^{-6} for Fe and -34×10^{-6} for Ni[8]. Here it is considered an isotropic approximation of the magnetostriction, or that is equal in every crystallographic direction. This is a good approximation only for materials without a well defined texture, as some polycrystals and amorphous materials.

In the presence of stress σ , a change in magnetization is observed mediated by the magnetostriction. Depending on the strength of the stress, this reverse phenomenon

may have profound impacts on the shape of the hysteresis curves, reducing or increasing the applied field necessary to magnetic saturation, acting as an extra internal field. The energy stored in the system by the stress, or the magnetoelastic energy E_{me} , is simply the work done on the material by the former as a function of the angle between the stress and the magnetization θ ³:

$$\int_0^{E_{me}} dE_{me} = -\sigma \int_{\lambda_p}^{\lambda_\theta} d\lambda \quad (2.26)$$

$$E_{me} = \frac{3}{2} \lambda_p \sigma \sin^2 \theta. \quad (2.27)$$

Thus, the combination of stress and magnetostriction results in a uniaxial anisotropy, and can be written in the form:

$$E_{me} = K_{me} \sin^2 \theta, \quad (2.28)$$

with $K_{me} = 3/2 \lambda_p \sigma$. with its hard or easy axis as function of its sign. If it is compressive it is negative, or tensile if positive.

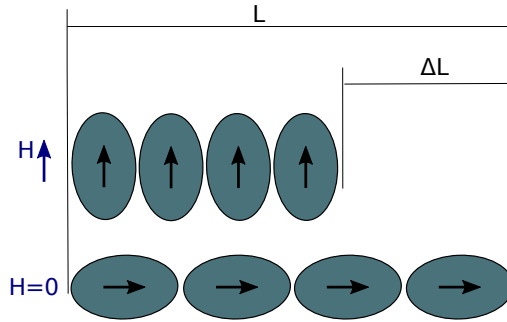


Figure 2.6: Illustration of the magnetostriction effect. Since the atoms are not completely spherical, the applied magnetic field changes the electron cloud distribution due to the spin orbit coupling, and a change in the dimension of the material can be observed.

2.3.2 Exchange energy

The main phenomenon in ferromagnetism is the Heisenberg interaction: $-J\vec{S}_1 \cdot \vec{S}_2$. In a ferromagnetic medium, neighboring spins tends to become aligned, making them

³It is just the area below a stress x strain curve

behave as a single identity over large portions of the material. Ferromagnets can then be treated as a continuous medium, as a function of the sum of the spin moments in that region, i.e, the magnetization.

Small variations of orientation between these regions can then be seen as a dot product - with an increase in the system energy caused by the misalignment of the magnetization. As such the energy in a continuous medium should depend on the gradient of the magnetization in all directions. If the change in the direction are not too abrupt, one can perform a Taylor expansion and obtain[9, 7]:

$$F_{ex} = \frac{A}{M_s^2} (\nabla \vec{M})^2 \quad (2.29)$$

where A is the exchange interaction constant. A is a phenomenological interpretation of the exchange constant in the material, changing its value for different materials and alloys.

Competing with the other energy terms, specially the anisotropy ones, the exchange energy has important consequences. One of them is the formation of domain walls, which will be briefly covered in chapter 5. Another is the exchange length l_{ex} :

$$l_{ex} = \sqrt{\frac{2A}{\mu_0 M_s^2}} \quad (2.30)$$

The exchange length is the distance in which the neighboring spins behave as one single entity, and it is used to give physical meaning to micromagnetic calculations. In a fully magnetized material, in the directions when the dimensions are bigger than the exchange length, a phase difference in the precession between neighboring regions may occur, generating spin waves.

2.4 Magnetic damping

The most common measurement of damping is the Gilbert magnetic damping α of equation 2.6. It is defined as dimensionless quantity and strictly positive. Experimentally, it is mainly obtained either by time-resolved or frequency domain linewidth in FMR experiments, as in this thesis, and the technique used will be used and described in detail in the following sections and in Chapter 3. The obtained raw parameter from FMR characterization is often referred as α_{eff} , since it is a combination of several physical processes converting the magnetic oscillations (precession) in lattice vibrations (phonons) and consequently heat.

The processes involved in the damping of the precession are divided in two broad categories: intrinsic and extrinsic phenomena. The intrinsic damping is related to phenomena that are inherent of the material or alloy of interest, and would be present even in an ideal perfect sample without any kind structural defects. The extrinsic damping

covers phenomena caused by structural defects, such as surface roughness, holes, crystalline discontinuities and impurities.

The intrinsic damping is a combination of a group of effects, all caused by the same underlying physical process: the conversion of magnons (local oscillations of magnetization) into phonons (local vibration of atoms in their sites). This is caused by distortions of the electron band structure in the material, mainly by spin-orbit coupling (SOC).

On the other hand, the extrinsic damping is originated from inhomogeneities in the structure of the material, such as crystalline grains, defects and doping materials. Since there are local structural differences in the material, the extrinsic damping might reflect in a non completely uniform precession of the FMR, generating a phase difference between the oscillations from region to region, i.e, spin-waves. These spin-waves interact with the main uniform mode and with themselves, increasing the linewidth and the damping. This effect is known in the literature as two-magnon scattering.

Spin pumping and spin-mixing at interfaces are common in FM samples with an adjacent NM material, especially heavy metals. The spin angular momentum is transferred through the interface into the NM metal by SOC, generating a spin current, that might even reflect back inside the FM. All this scattering causes another channel of energy dissipation, increasing the linewidth.

Hence, the intrinsic damping comprehends all the phenomena that are associated to a material, and does not change from sample to sample, while the extrinsic damping are from small variations on fabrication conditions, and may change from sample to sample.

2.5 Uniform precession and Ferromagnetic resonance

The Eq. 2.6 is non-linear, and with no universal analytical solutions. Nevertheless, it can be solved by means of approximations for specific situations of interest. In the case of the FMR, which is defined by a uniform precession of the magnetic moments of the material around the effective applied field H_{eff} , the analytical solution can be found by setting the component of the magnetization vector to have the same magnitude as the saturation magnetization $M_0 \approx M_s$. In other words, if the precession is small enough to cause a negligible effect on the magnetization.

Using this approximation, one cannot utilize standard static magnetization experiments anymore, since they rely directly on the magnetization. By utilizing the Poynting theorem and the Maxwell equations, one can find the relationship of the absorbed alternated current (AC) power (generating an AC oersted field \vec{h} acting on a magnetic material), and the magnetic susceptibility χ [10]:

$$P_{abs} = -\frac{1}{2} \int_V \omega \chi'' |\vec{h}|^2 dV + i \frac{1}{2} \int_V \omega (1 + \chi') |\vec{h}|^2 dV \quad (2.31)$$

where V is the volume of the magnetic material, ω the frequency in radians per second, χ' and χ'' the real and imaginary parts of the susceptibility.

Thus, one can measure χ by means of an AC field on a magnetic material at the resonance. In other words, it is of interest to understand how the resonance conditions, i.e., the applied field and the frequency are related to each other to extract magnetic constants imbued in the effective field. Hence, we are now interested in two solutions of the linearized LLG equation: one for the susceptibility $\chi(\omega)$ and another one for the resonance frequency $\omega(H)$.

2.5.1 Magnetic susceptibility at the resonance

For this solution, the effects of the effective field are not considered, as if there were only the applied field H . The magnetization \vec{M} and applied field \vec{H} vectors are given by:

$$\vec{M} = \vec{M}_0 + \vec{m}(t); \quad (2.32)$$

$$\vec{H} = \vec{H}_0 + \vec{h}(t); \quad (2.33)$$

where \vec{M}_0 and \vec{H}_0 , $\vec{m}(t)$ and $\vec{h}(t)$ are respectively the static and alternating components of the magnetization and applied field. These are then inserted on the LLG equation, considering the alternating components in the form $\propto \exp[i\omega t]$. Since $M_0 \approx M$, the resulting equation of motion is:

$$\frac{d\vec{m}}{dt} = \gamma\mu_0\vec{M}_s \times \vec{h}. \quad (2.34)$$

The equation of motion can then be rewritten in the following way:

$$\vec{M} = \vec{\chi}\vec{H} \quad (2.35)$$

where $\vec{\chi}$ is the Polder susceptibility vector:

$$\vec{\chi} = \begin{bmatrix} \chi & i\kappa \\ -i\kappa & \chi \end{bmatrix}. \quad (2.36)$$

Finally, the solution is found to be⁴:

$$\chi_+ = \chi'_+ + i\chi''_+; \quad (2.37)$$

$$\chi'_+ = \frac{\omega_m(\omega_0 - \omega)}{(\omega_0 - \omega)^2 + \omega^2\alpha^2}; \quad (2.38)$$

$$\chi''_+ = \frac{\omega_m\alpha\omega}{(\omega_0 - \omega)^2 + \omega^2\alpha^2}; \quad (2.39)$$

⁴The full step by step solution can be found at [11, 12]

where $\omega_m = -\gamma\mu_0 M_S$ and $\omega_0 = -\gamma\mu_0 H_0$.

The normalized plot of the real and imaginary parts of χ_+ can be seen in Fig.2.7. The imaginary component is responsible for the power loss at the resonance, and the real part for a phase dispersion. Here χ_+ is different due to considerations of the geometry of the alternating field, since we approximate it to be only with one perpendicular component, as if in a TEM (transverse electromagnetic mode) case, of specific interest for experiments.

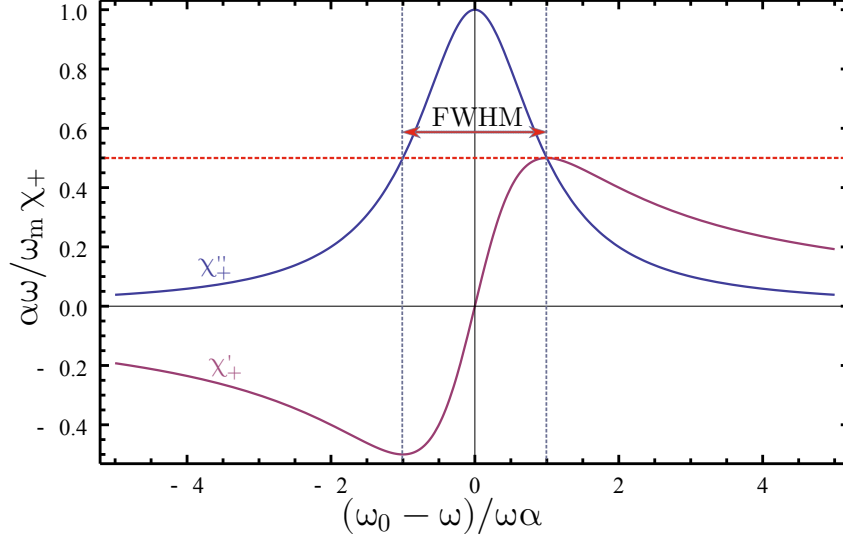


Figure 2.7: Centered and normalized resonance plot of the real (χ'_+) and imaginary (χ''_+) susceptibility components as a function of frequency. The vertical lines are highlighting the FWHM and its relationship between the imaginary and real components.

The linewidth of the absorption derived from the imaginary component of χ_+ carries information about the magnetic losses. It is thus a term of great importance, and is defined as the full width at half maximum (FWHM) of the χ''_+ peak in Fig.2.7 . Its relationship to χ is given by:

$$\Delta\omega = \omega_2 - \omega_1 = 2\alpha\omega_0 \quad (2.40)$$

This relation is found by subtracting the the value of two solutions ω_2 and ω_1 of $\chi''(\omega) = \chi''(\omega_{res})/2$.

One can then extract the resonance conditions and FWHM from the absorbed power. The next step is to find how these conditions are connected to each other, or more precisely, to the effective field H_{eff} in order to obtain the magnetic anisotropy.

2.5.2 Smith-Beljers Formula

The next formula was developed by Smith and Beljers in [13]. It is a general way to obtain the resonance dispersion relations, by defining the free magnetic energy density terms of the system of interest. The resonance dispersion relations are defined by:

$$\omega_{res} = \gamma H_{eff} \quad (2.41)$$

and the effective field H_{eff} :

$$\vec{H}_{eff} = -\frac{1}{\mu_0} \nabla_{\vec{M}} F(\vec{M}). \quad (2.42)$$

Basically, the solution to be found connects the free magnetic energy F of the system with the effective field and the resonance frequency. The gradient acting on F is on the magnetization axis system of coordinates, that is not necessarily the same as the applied field one. It is compulsory then to use the appropriate coordinate system, and it is more convenient doing so a spherical reference frame, which was already defined in 2.3:

$$\hat{e}_\rho = \begin{bmatrix} \sin \theta \cos \phi \\ \sin \theta \sin \phi \\ \cos \theta \end{bmatrix}; \quad \hat{e}_\theta = \begin{bmatrix} \cos \theta \cos \phi \\ \cos \theta \sin \phi \\ -\sin \theta \end{bmatrix}; \quad \hat{e}_\phi = \begin{bmatrix} -\sin \phi \\ -\cos \phi \\ 0 \end{bmatrix}; \quad (2.43)$$

In this new system, the same linearization condition of small precessions of the last section is used:

$$\vec{M} = M_s \hat{e}_\rho \quad (2.44)$$

$$\theta = \theta_0 + \delta\theta; \quad \delta\theta \ll \theta_0 \quad (2.45)$$

$$\phi = \phi_0 + \delta\phi; \quad \delta\phi \ll \phi_0 \quad (2.46)$$

So that the magnetization vector has the fixed magnitude of the saturation magnetization M_s , and it is allowed to have small oscillations $\delta\phi$ and $\delta\theta$ around the equilibrium position θ_0 and ϕ_0 . For example, in a thin film, when the applied field is either perpendicular or parallel to the sample surface, the equilibrium position of the magnetization will be the same as of the applied field.

The general formula is given by:

$$\omega_{res} = \gamma^* (1 + \alpha^2)^{1/2} \frac{1}{M_s \sin \theta_0} [F_{\theta\theta} F_{\phi\phi} - F_{\theta\phi}^2]_{(\theta=\theta_0, \phi=\phi_0)}^{1/2}, \quad (2.47)$$

and the linewidth by:

$$\Delta\omega = \frac{\alpha\gamma^*}{M_s} [F_{\theta\theta} + (\sin^2 \theta_0)^{-1} F_{\phi\phi}]_{(\theta=\theta_0, \phi=\phi_0)} \quad (2.48)$$

Formally there is a $(1 + \alpha^2)^{1/2}$ factor in these equations, but are significant only with high damping of around 0.1, and while the values found in this thesis are in the order of 10^{-3} .

2.5.3 Uniaxial anisotropy solution

Since all the uniaxial energy terms ($F_{uni} = F_{shape} + F_{crys} + F_{m-e}$) have the same form, changing only by a constant, they can be grouped together with a K_{eff} constant⁵:

$$K_{eff} = -\frac{1}{2}\mu_0 M_s^2 + K_{crys} + K_{m-s} \quad (2.49)$$

From now on, it is possible to obtain an equation to extract K_{eff} from experiments. This is extremely helpful, since one can use the same method for different samples as long as their anisotropy depends only in one axis. Hence, for a fully magnetized thin film with uniaxial anisotropies the free magnetic energy is:

$$F = F_{Zeeman} + F_{shape} + F_{crys} + F_{m-e} \quad (2.50)$$

$$= -\mu_0 \vec{M} \cdot \vec{H} + K_{eff} \sin^2 \theta \quad (2.51)$$

Defining:

$$\mu_0 H_A \equiv \frac{2K_{eff}}{M_s} \quad [T], \quad (2.52)$$

one can substitute it on Eqs.2.47 and 2.48 and obtain the general ferromagnetic resonance equation for uniaxial anisotropic materials:

$$\frac{\omega_{res}^2}{\mu_0 \gamma} = [H \cos(\theta_H - \theta_0) + H_A \cos 2\theta_0] \cdot [H \cos(\theta_H - \theta_0) + H_A \cos^2 \theta_0]; \quad (2.53)$$

and the linewidth:

$$\Delta\omega = \alpha\gamma\mu_0[2H \cos(\theta_H - \theta_0) + H_A(3 \cos^2 \theta_0 - 1)], \quad (2.54)$$

with the equilibrium angle θ_0 given by⁶:

$$H \sin(\theta_H - \theta_0) = H_A \sin \theta_0 \cos \theta_0. \quad (2.55)$$

The equilibrium condition is an implicit non-linear equation, and it can be solved only numerically. It cannot be substituted in Eqs.2.53 and 2.54. However, it does have trivial solutions if the measurement is performed with the applied field H either in-plane ($\theta = \pi/2$) or out-of-plane of the sample ($\theta = 0$).

⁵the terms can be added remembering that: $\cos^2 \theta = 1 - \sin^2 \theta$

⁶the angles ϕ and ϕ_0 are not relevant, since it is a uniaxial anisotropy system!

To this end, the equations for the in-plane field are:

$$\omega_{res} = \gamma\mu_0\sqrt{H_A^2 - H^2}, \quad \text{if } |H_A| > |H|; \quad (2.56)$$

$$= \gamma\mu_0\sqrt{H[H - H_A]}, \quad \text{if } |H_A| < |H|; \quad (2.57)$$

and for the out-of-plane field:

$$\omega_{res} = \gamma\mu_0[H - H_A] \quad \text{if } |H_A| < H \quad (2.58)$$

The linewidth for both in-plane and out-of-plane orientations is given by:

$$\Delta\omega = 2\alpha\gamma\mu_0[H - H_A], \quad (2.59)$$

The normalized solutions for each combination of IP and OOP anisotropies and fields are plotted in Fig.2.8. By fitting the experimental resonance data with these equations, one can obtain the anisotropy field H_A , and its effective constant K_{eff} . A step by step example will be shown in the next chapter.

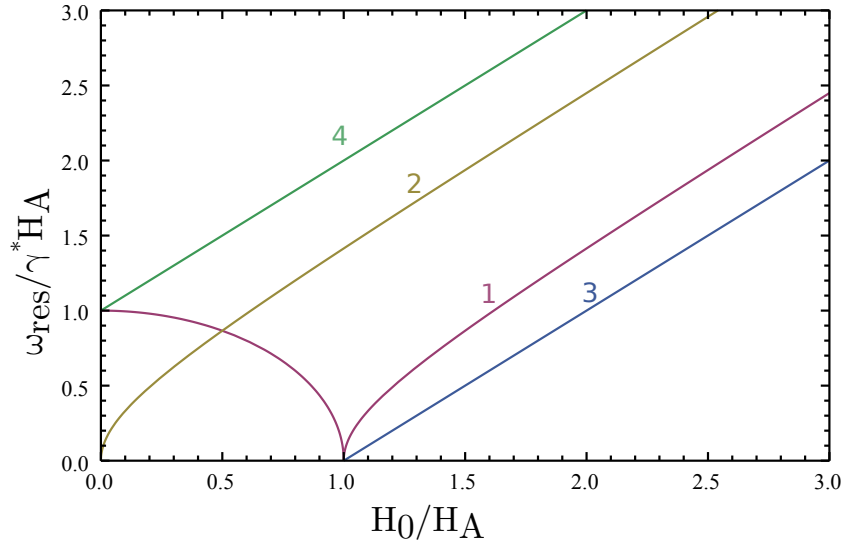


Figure 2.8: Normalized resonance frequency as a function of IP and OOP static fields. Plots 1 and 2 with IP static field; 3 e 4 with OOP; $K_{eff} < 0$ e $K_{eff} > 0$ respectively.

2.6 Spin transfer torques

When there is an electron flow in a ferromagnetic material, the spins in the current are randomly oriented, and their average effect on the magnetization is zero. However, if by

any means they become polarized, they interact to exert a torque on the magnetization. The phenomena is called either spin transfer torque (STTs) [14] or spin orbit torque (SOTs) [15], depending on the physical origin of the spin polarization mechanism.

The first theoretical prediction of STTs came at the end of the 1970s by the group of L. Berger, when they predicted a canting on domain walls caused by an electron current [16, 17], followed by an experimental verification of domain wall motion in 1980s [18, 19]. With mm wide Py thin films, the necessary current for moving the domain wall was < 40 A ($1 \sim 2 \times 10^{-11}$ Am^{-2}). It did not sparked much interest in the community, until the discovery of the interlayer exchange coupling [20] and giant magneto resistance [21, 22], following the development magnetic tunnel junction (MTJ) devices.

The MTJs are a trilayer structure, two ferromagnets separated by an ultrathin non magnetic insulating barrier. If both ferromagnetic layers have the same orientation of magnetization, the resistance is minimum, if they have opposite orientation, the resistance across the barrier is maximum. The mechanism is due to the spin polarization of the electron current passing through the first FM layer. The polarized current then interacts with the magnetization of the second layer, increasing its scattering and consequently the electrical resistance. At the end of the 1990s Slonczewski [23] predicted that a dc current flowing perpendicular to the plane in such kind of device could switch the layer's magnetization, and the low resistance of the layers could tolerate the high currents necessary to produce the effect, which was called STT.

It was found later that a greater degree of spin polarization can be achieved in heavy metals, due to their high spin orbit coupling. An electron current flowing through the thickness of a HM thin film will produce a flux of spin current with opposite orientations on its surfaces (known as the Spin Hall effect). If one of the surfaces is now attached to a ferromagnetic layer, its magnetization will feel the torque from the transferred spin current. Here, since the underlying cause is the spin orbit coupling and the spin Hall effect, the torques are called spin orbit torques.

The torques are referred as damping-like (a_j) and field-like (b_j) torque. The first has an opposite direction to the damping, and the second one acts as an extra external field (see Fig. 2.9). The LLG equation with added torques is then:

$$\frac{d\vec{M}}{dt} = -\gamma(1 + \alpha^2)\mu_0\vec{M} \times \vec{H}_{eff} - \mu_0\vec{M} \times b_j\hat{p} - \frac{\alpha}{M_s}\vec{M} \times \frac{d\vec{M}}{dt} - \frac{a_j}{M_s}\vec{M} \times (\vec{M} \times \hat{p}). \quad (2.60)$$

There are several interesting consequences of these added torques. For example, the electrical current flowing through the film cross section can be set in such a manner to make the damping-like torque fully compensate the magnetic damping - allowing the system to precess indefinitely as an oscillator (see Fig.2.10). If attached to another HM layer on the opposite side of the FM, this layer will then generate an electric microwave current by the inverse spin Hall effect.

Another consequence is the possibility of obtaining a complete inversion of the magnetization in an adjacent film layer as a function of the spin polarized current intensity, as can be seen in the loop in Fig.2.11.

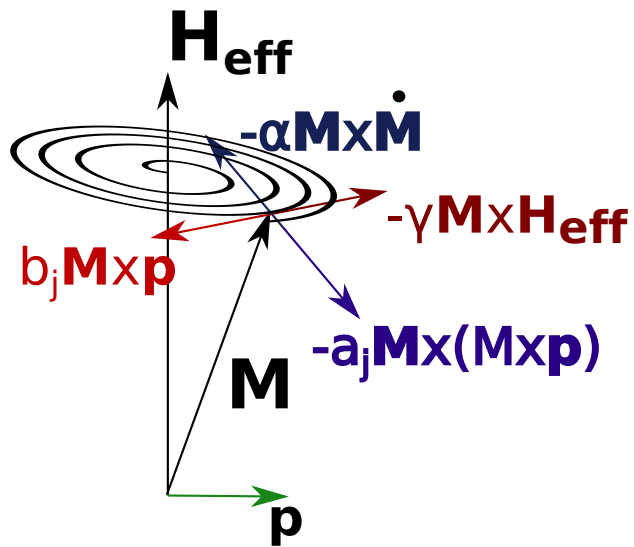


Figure 2.9: Spin transfer torque added vector scheme on the LLG equation.

For the two examples mentioned above the anisotropy was set to an in-plane easy axis ($K < 0$). The case with out-of-plane easy axis is of more interest to technological applications, but comes with some caveats. It will be explored in more detail on chapter 5.

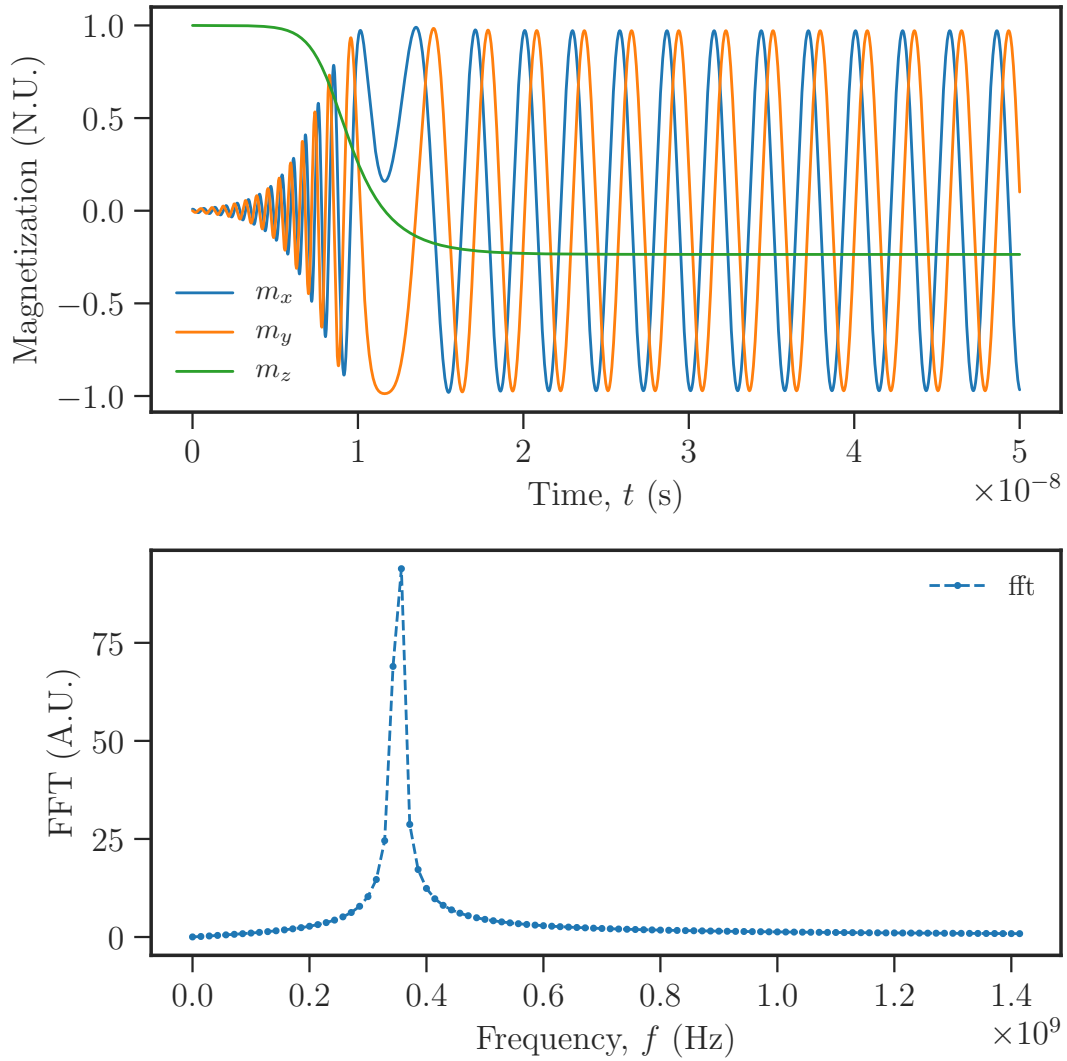


Figure 2.10: Spin transfer torque induced oscillator. The field like torque b_j is set to zero, and the damping like a_j is set to compensate the Gilbert damping. Hard axis on \hat{z} direction. No external field applied, only a current.

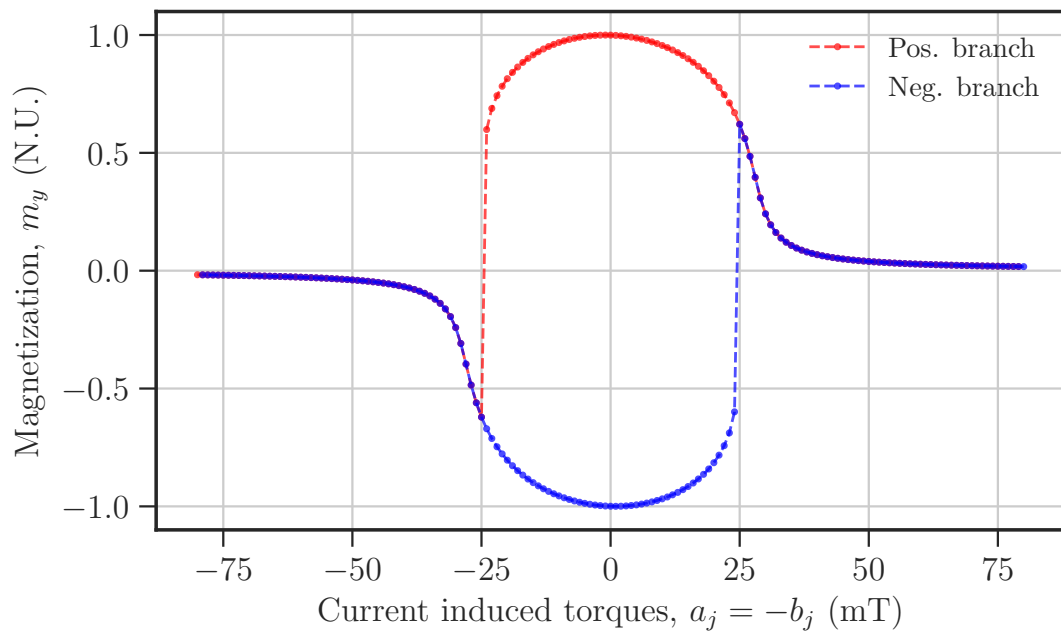


Figure 2.11: Final magnetization as a function of the STT induced torques. $b_j = -a_j$, in red decreasing from positive to negative, in blue otherwise. Hard axis on \hat{z} direction. No external field applied.

Chapter 3

Experimental Methods

In this chapter the experimental methods utilized in this thesis will be described, more specifically about the ferromagnetic resonance experiment.

The first section covers the basics about the ferromagnetic resonance experiment, from a brief historical introduction to modern broadband experiments. Afterwards is detailed the functionality of the two common approaches for the broadband experimentation: using the Vector Network analyzer (VNA) or the Lock-in amplifier + diode detector. With the VNA, the text is focused in the mathematical analysis of the extracted data and the meaning of its measured quantities. On the other hand, with the Lock-in amplifier approach, the measured quantities are directly linked to the resonance, so the focus is shifted to explaining the internal functionality of the instrument and its peculiarities on the experimental setup. In both cases, it is presented an example of absorption spectra of the resonance.

The second section covers the step by step process to use the resonance to characterize magnetic materials. It uses adapted versions of the equations shown in the last chapter with a Permalloy sample.

The third section covers the investigation about interferometer techniques applied to the ferromagnetic resonance, performed abroad at the Physikalisch-Technische Bundesanstalt in Braunschweig - Germany.

3.1 Ferromagnetic resonance experiment

The first ferromagnetic resonance (FMR) experiments were performed by V. K. Arkad'yev in a series of works between 1911 and 1913[11], observing an absorption by applying centimeter waves in Ni and Fe wires. Ya. G. Dorfman (1923) [24] gave the first qualitative explanation based on the Zeeman effect, in which the absorption was a transition between Zeeman multiplets caused by the excitation wave. The matter was further progressed by L.M. Landau and E.M. Lifshitz in 1935, when it was proposed the equation about the dynamics of the magnetization. In the next decades, the efforts of the scientific

community shifted towards the electron paramagnetic resonance (EPR), both theoretically and experimentally [25, 26]. With this new found experimental techniques, they were applied to ferromagnetic materials in 1946 simultaneously in the UK and USSR, where Griffiths[27] and Zavoisky [28] published experimental works with Ni,Fe,Co and FeSi, opening up to the first quantitative interpretations of the phenomena by Kittel [29, 30] and Van Vleck [31], generalizing the Landau-Lifshitz equations and developing the modern interpretation of the phenomena. Since then this model has been vastly used to characterize magnetic parameters such as the anisotropy field, gyromagnetic constant and gilbert damping of ferromagnetic alloys. The FMR characterization has superior accuracy in obtaining specifically two magnetic parameters: the magnetic damping and the anisotropy field.

The basic principle of the FMR experiment is to find the field and frequency parameters where there is a resonant absorption, which translates to a loss in transmitted or reflected microwave power at the receiver. Physically, the experiment is composed by two general important ingredients: an external magnetic field and a small alternating excitation field. The external field aligns the magnetic moments with himself, and together with its internal field dictates its natural precession period, called the Larmor precession. The alternating excitation field is introduced by means of an ac electromagnetic wave, in such a way that its ac magnetic component is perpendicular to the static one, tilting the magnetization axis of the system slightly inducing a short lived precession. If both frequencies are the same, the precession is persistent and the ac signal is absorbed by the sample and converted in heat. This frequencies are typically in the GHz range, since the magnetic moments are given by the free electron spins of the ferromagnet and depends on the gyromagnetic ratio.

In order to find the resonant absorption, one then needs to sweep either the frequency or the field, while fixing the other quantity and search for and absorption in the measured ac signal. In the classical EPR experiment mentioned above the ac signal is introduced on a resonant cavity that has its own fixed resonance frequency, dependent on its geometrical dimensions. The cavity is then fine tuned (either physically or by adjusting the frequency) without field so there is a resonance of the electromagnetic field inside, reflecting near zero power signal to the receiver. By sweeping the external field, when the FMR condition is met the whole electromagnetic characteristics of the cavity are changed, and some signal is reflected. Although this method has an incredible sensitivity, since only the difference in signal due to the FMR is measured, one needs to change the whole cavity to change substantially the frequency - almost invalidating the use of the Kittel equations. To circumvent this problem, the broadband FMR (BBFMR) techniques were developed.

3.1.1 Measurement of the FMR in broadband frequencies

To measure the FMR in a wide span of frequencies (BBFMR), instead of using a resonant cavity to introduce the excitation field, one uses design variations of a planar open

wire called striplines. There are several ways of implementing them: a wire covered in a casing for grounding, a line on a face of substrate with a ground on the opposite face, etc.

A widely used variation is called coplanar waveguide (CPW), in which a central stripe carries the signal, and have two ground planes on the same face of the substrate separated by small gaps. The resulting effect is a confinement of the excitation field to a very narrow area around the central strip (see Fig.3.1). This mitigates a bit the loss of quality factor in comparison to resonant cavities, and permits to control precisely its impedance to match the whole system. The expression for the CPW can be found in page 79 of [32].

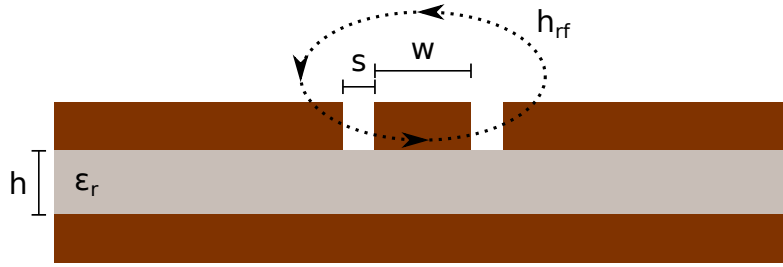


Figure 3.1: Coplanar waveguide cross-section illustration. Excitation field shown by h_{rf} .

The impedance of the line is mostly determined by the signal line and gap widths, which also determine the probed volume of the sample, and hence critical to the amplitude of the measured absorption. Thus, the bigger the central conductor, the larger the sample volume probed, and the larger the signal. The trade-off of a larger center conductor is loss a of sensitivity of higher frequencies. Our CPW is matched to 50Ω up to 50 GHz, and has the following dimensions: $w = 2$ and $s = 0.1$ mm with a ROS404 substrate.

Therefore, in order to perform a BBFMR experiment one needs to detect a microwave power absorption by a sample positioned on top of a CPW, as a function of both frequency and static field. The absorbed power at the resonance P_{abs} is given by [10]¹:

$$P_{abs} = -\frac{1}{2} \int_V \omega \chi'' |\vec{h}|^2 dV + i \frac{1}{2} \int_V \omega (1 + \chi') |\vec{h}|^2 dV \quad (3.1)$$

where ω is the frequency in radians per second, h the excitation field, V the volume of the sample and $\chi = \chi' + i\chi''$ the complex permeability.

There are basically two ways of performing the BBFMR experiment: one by using a Vector Network Analyzer (VNA) and other utilizing a combination of a microwave

¹Refer to Appendix for demonstration

source, diode detector and a lock-in amplifier. The first approach is the most used, since it has a direct experimental setup - the VNA is responsible for generating the signal and measuring it on the same device. Also it is capable of measuring both the real and imaginary components, but the conversion to the permeability units is not straight forward. The second is a modular approach, in which the signal produced from a microwave generator reaches the CPW, then a diode detector and finally is read by a lock-in amplifier. The measured signal is a voltage directly proportion to the transmitted power, so no extra mathematical conversion is needed. This approach only probes the imaginary part of the magnetic susceptibility at the resonance.

BBFMR experiment with the Vector network analyzer (VNA-BBFMR)

The BBFMR-VNA experiment scheme can be seen in Fig.3.2. The CPW is connected between the two Vector Network Analyzer (VNA) ports P1 and P2, and inserted in the electromagnet applying the static magnetic field. The applied field is controlled by a Power Supply and measured by a Gaussmeter. The experiment is done by sweeping the microwave (MW) frequency of the signal with a fixed applied field. In this section it will be described in detail the VNA measured quantities and their relationship with the magnetic susceptibility and the FMR.

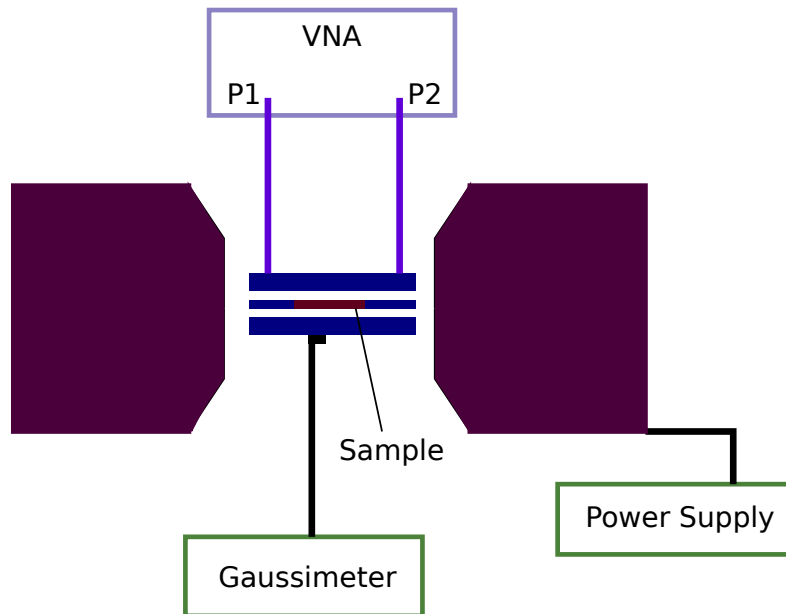


Figure 3.2: Experimental schematics of the BFMR with the VNA.

When the wavelength of an alternated signal is comparable to the components dimensions in a circuit, as is the case with microwaves, one needs to consider the signal interfering with itself due to possible internal interference and diffraction. As such, the voltage, current and impedance (lumped parameters) are not uniform in the circuit, and

may change locally due to constructively or destructively interference of its traveling waves. A more convenient way of interpreting the system is by using distributed parameters instead, which takes in consideration the fact that the circuit changes both in time and space. The Vector Network Analyzer is an equipment optimized to measure these distributed parameters, and it is vastly used in high frequency applications [33].

The scattering parameters is one of them, and is defined by the scattering matrix $\sum_{i,j} S_{ij}$. The S_{ij} matrix components are the ratio between the received and emitted wave at a determined port. At Fig.3.3 one can see the scheme for a two-port setup, considering both ports and the device under test (DUT). For example, the S_{12} parameter is the ratio between the wave emitted by port 1 (a_1) and the resultant wave arriving at the port 2 (b_2). The wave b_2 is then the result of the traveling wave a_1 by being partially reflected by the left and right side of the DUT and its possible interference in a given period of measured time. This is the equivalent of a scattering, caused by the impedance discontinuity induced by the DUT in the circuit, and hence the name.

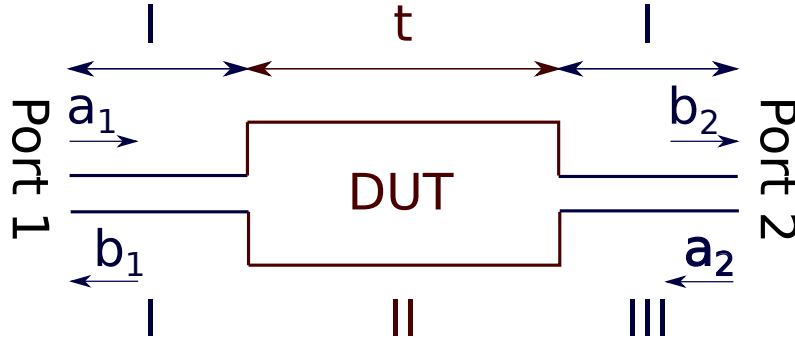


Figure 3.3: scheme with a_j/b_j waves

Albeit being more convenient to deal with the scattering parameters instead of the direct voltage and power of conventional circuits, one still needs to do the backward path to obtain the magnetic susceptibility and finally the power loss due to the resonance (Eq. 3.1). The first conversion method from scattering parameters to permittivity and permeability was described by W.S Barry [34]. In the case of the FMR, only the permeability changes with the field, and thus variations of the Barry method have been proposed: either by simplifying the post processing neglecting the reflections [35], or to correct geometrical asymmetries of the system [36].

The relationship between the relative magnetic permeability μ_r ² and relative dielectric constant ϵ_r in a circuit as Fig.3.3 is given by [34]:

²The relative magnetic permeability μ_r is the ratio between the permeability of interest and the free space permeability μ_0

$$\epsilon_r = A \frac{k}{k_0} \frac{1-R}{1+R} \quad (3.2)$$

$$\mu_r = A \frac{k}{k_0} \frac{1+R}{1-R}, \quad (3.3)$$

where A is an adjustment parameter to compensate imperfections on the circuit, $k_0 = 2\pi f \sqrt{\mu_0 \epsilon_0}$ is the wave vector of free space. The wave vector k and reflection constant R are related to the scattering parameters as:

$$kt = \cos^{-1} \left(\frac{e^{-i4k_0 l} + S_{12}^2 - S_{11}^2}{2e^{-i2k_0 l} S_{12}} \right) = \cos^{-1}(arg) \quad (3.4)$$

$$R = \frac{S_{11}}{e^{-2ik_0 l} - S_{12}e^{-ikt}}. \quad (3.5)$$

Breaking k in real and imaginary components:

$$Re[kt] = \Theta_G \pm 2n\pi, \quad n = 0, 1, 2, \dots \quad (3.6)$$

$$Im[kt] = \ln G, \quad (3.7)$$

considering:

$$\Theta_G = \arctan \left[\frac{Im(arg - \sqrt{arg^2 - 1})}{Re(arg - \sqrt{arg^2 - 1})} \right] \quad (3.8)$$

$$G = \sqrt{Re[arg - \sqrt{arg^2 - 1}]^2 + Im[arg - \sqrt{arg^2 - 1}]^2} \quad (3.9)$$

where t is the sample length and l is the empty spaces of the CPW.

Here, there are several geometrical quantities to be inserted related to the positioning and geometry of the sample (t and l), which can be a considerable source of errors. To circumvent this problem, Bilzer makes a geometrical average of S_{11} and S_{22} , instead of considering only the S_{22} value[36]:

$$S'_{11} = \sqrt{S_{11} S_{22}}, \quad (3.10)$$

and subsequently substituting S_{11} by S'_{11} on equation 3.3. Next, on the frequency range of interest for the FMR described, the electrical permittivity is constant, and can be scaled off. Thus, the permeability can be seen as:

$$\mu_r \propto \left(\frac{kt}{k_0(t+2l)} \right)^2. \quad (3.11)$$

Nonetheless, the final equations are still of considerable complexity, and its applicability is dependent on a precise calibration of the VNA and circuitry - that needs to be redone on each repositioning of cables, connectors and CPW.

Kalarical et.al. proposed a very elegant simplification [35], relying on the fact that the reflection parameters S_{11} and S_{22} are a few orders of magnitude smaller than the transmission coefficients S_{12} and can be neglected. This simplifies greatly equation 3.3, removing also the geometrical associated inputs. More importantly, the method also subtracts a reference measurement with a different static field intensity, serving as an more situational accurate calibration. The final expression is then given by:

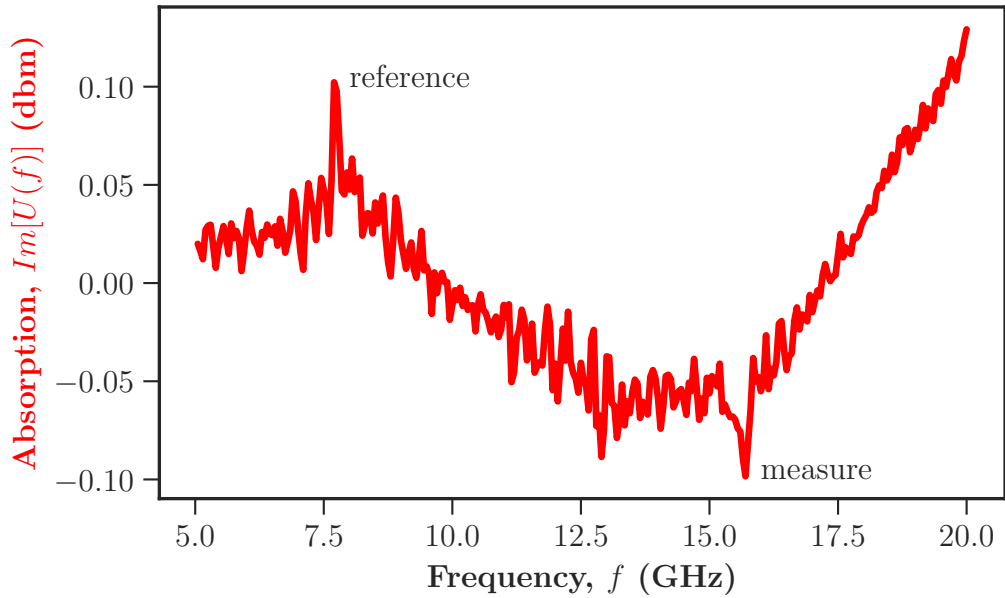
$$\text{Re}[U(f)] = \arctan \frac{\text{Im}[S_{21mes}]}{\text{Re}[S_{21mes}]} - \arctan \frac{\text{Im}[S_{21ref}]}{\text{Re}[S_{21ref}]} \quad (3.12)$$

$$\text{Im}[U(f)] = \frac{A}{2\pi f} \ln \frac{|S_{21mes}|}{|S_{21ref}|} \quad (3.13)$$

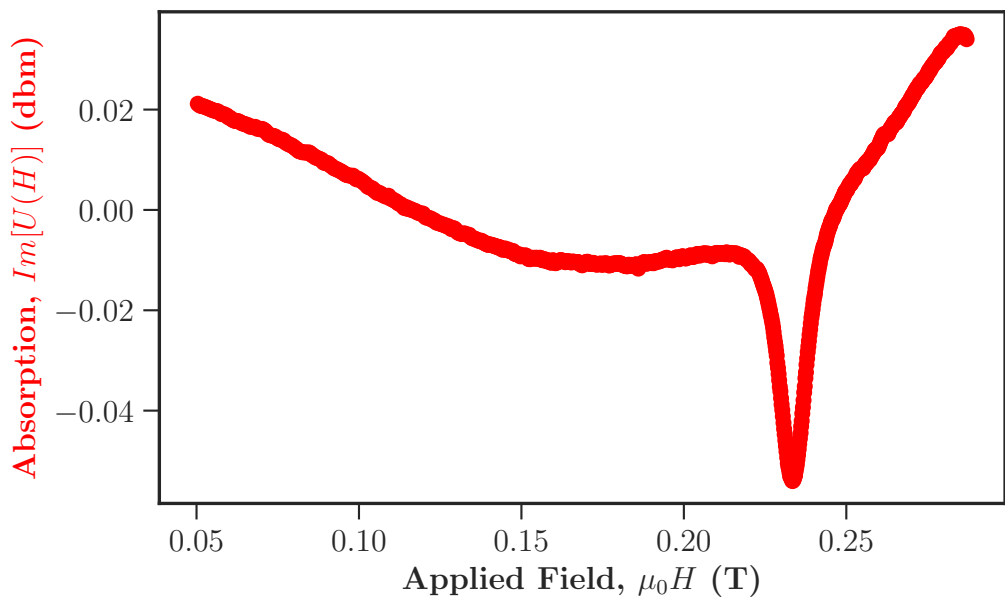
where the $U(f)$ is the uncalibrated magnetic permeability, f is the measured frequency, and A an amplitude scaling constant.

An example of a 20 nm permalloy($Fe_{80}Ni_{20}$) measured absorption spectra is shown in Fig.3.4a. Here one can see the results of the subtraction, with a positive absorption peak of the reference, and the negative peak of interest. Even though the subtraction of the reference should account for clearing the systematic errors of a thorough calibration, they still are present to a smaller degree. This happens due to the fact that even small variations of temperature can cause a change of the impedance of the contacts, causing a drift on the measured signal compared to the reference one. A simple manner of circumvent this problem, which is to perform a field sweep at a fixed frequency instead, since in principle only the magnetic related phenomena (at GHz range should only be the FMR) modifies with the received signal. Performing the experiment like this would remove completely the needs of calibration, but rejects the advantage of subtracting a reference measurement in Eqs.3.12 and 3.13. Moreover, the VNA is not optimized to work with a monochromatic wave, and as such introduces harmonics at other frequencies. Also, each field step needs to have a time delay in order to stabilize the static field. Since one needs the find the relationship of frequency and field of the absorption, the result is a too much time consuming process.

The solution I found was to perform the experiment as a conventional frequency sweep and convert the dataset for a field sweep numerically. The experimental frequency sweep dataset is composed by fixed field files of frequency per S parameters. One can add them all together in a big tensor, and rebuild the dataset. The result is a file for each fixed frequency, with field per S parameters. The subtraction can also be performed now, as long as is done before the conversion. A spectra can be seen in Fig.3.4b, with the same exact experimental dataset from Fig.3.4a and resonance conditions.



(a)



(b)

Figure 3.4: Comparison between different subtraction methods with the same dataset. Py 20 nm. a) Subtraction of a reference in a frequency sweep. The reference and measurement field are respectively 74 mT and 250 mT. b) Converting the subtracted frequency sweep data for a field sweep dataset.

BBFMR experiment with the Lock-in amplifier (BBFMR-Lock-in)

Broadband FMR experiments can also be done without the VNA by a modular approach, exciting the sample via a microwave generator and reading the power with a diode detector and a Lock-in. The schematics of the experiment can be seen on Fig.3.5. The microwave generator inputs the signal on the CPW, the transmitted signal is then rectified by a diode detector and read by the Lock-in amplifier. This is a direct power measurement, that depends on the impedance, which changes with the frequency. Hence the experiment have to be necessarily done by sweeping the applied field at a fixed frequency, otherwise the absorption may not be seen.

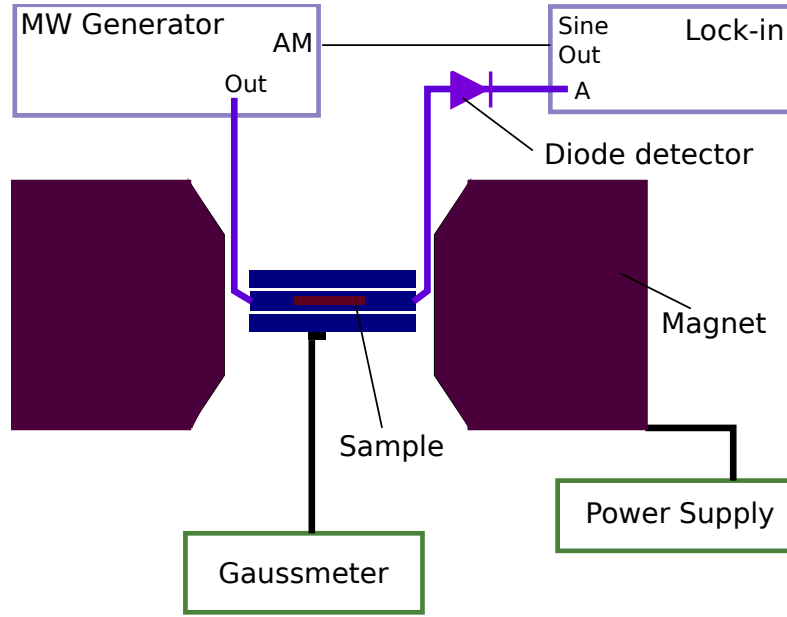


Figure 3.5: Lock-in-BFMR schematics.

The lock-in amplifier is capable of extracting of very weak signals from extremely noise environments by reading the signal only at a specific predetermined frequency f_m . Any oscillatory signal can be expanded in an Fourier series [37], or an infinite series of sines or cosines, and so the input signal can be written as:

$$V_{input} = \sum_n V_n \sin(2\pi f_n t - \phi_{input}), \quad (3.14)$$

where V_n is the voltage component of the series, and ϕ_{input} a possible phase offset from the input signal.

The lock-in then multiplies the received V_{input} by a reference $V_{ref} = V' \sin(2\pi f_m t - \phi_{ref})$ at the desired frequency f_m and then integrates it in a total period T :

$$V_{mes} = \int_0^T V_{input} V_{ref} dt \quad (3.15)$$

By utilizing the orthogonality property of trigonometric functions, which states that the integration over a full period of two multiplied sines (cosines) is equal to zero as long the frequencies are different, and proportional to $1/\sqrt{2}$ if equal [37], the measured signal becomes:

$$V_{mes} = V'V_{f_m}/\sqrt{2} = V_{rms}, \quad (3.16)$$

where V' is the reference amplitude and V_{f_m} the input voltage amplitude of the series at the frequency f_m of the reference.

Finally, the result is the resultant root mean square value V_{rms} , which is directly proportional to the measured power. It is worth stressing that the amplitude V' of the reference multiplies the signal only at the reference frequency, amplifying only the signal of interest against the random noise. Also, by increasing the integration time T (Lock-in's Time constant) to several periods, one averages the measurement. Thus, the lock-in amplifier is an extremely elegant and sensitive instrument.

There are a few important details to consider when using the lock-in amplifier to BBFMR experiments. First, since it is a power measurement, only the imaginary part of the permeability can be probed, and the real part of Eq.3.1 is lost. Second, the internal frequencies of the instrument works at radio-frequency (RF) range (KHz): implying in the use of a rectifying diode and a modulation wave on top of the carrier microwave signal.

Initially, a microwave is generated with the desired frequency in the GHz range (see Fig.3.6a). Then, the combined modulating and microwave signal can be seen in Fig.3.6b). This combined signal is then fed in the CPW, and produces the alternate excitation field h_{rf} applied to the sample. Afterwards, in Fig.3.6c), it is rectified by the planar-doped barrier diode (Schottky) and only one of the polarities survives - depending on the diode chosen positive or negative specifications. Finally the Lock-in reads the average of this value V_{RMS} , which in this case is directly proportional to the power. If the sample enters in the vicinity of a resonance in relationship to the applied field H , it absorbs power, transmitting a smaller amplitude in the carrier wave - that propagates to the modulated RF and to the V_{RMS} .

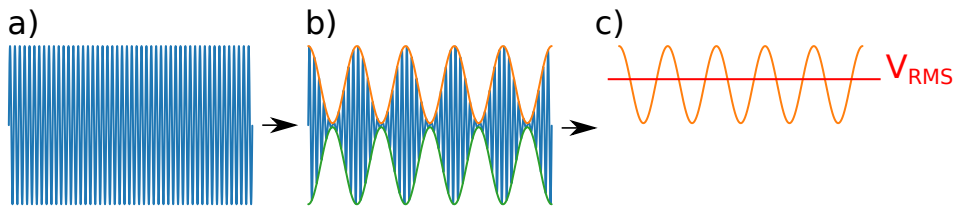


Figure 3.6: Scheme of the amplitude modulation generating and reading process. The carrier microwave can be seen at a), the combined RF AM modulation and carrier wave at b) and finally the rectified signal by the diode at c). The lock-in then reads the average of the signal, namely the V_{RMS} . Thus, any change in the amplitude of the carrier microwave will reflect directly on a change on V_{RMS} .

3.2 Magnetic constants extraction

The BBFMR experiment allows the characterization of three magnetic constants: the gyromagnetic factor γ , the anisotropy field H_a and the Gilbert damping α . The characterization consists in two steps: obtaining the resonances frequency and fields and their linewidth, and then fit them with the Kittel equations. In this section I show only the VNA spectra, since the Lock-in experiments are the same as the imaginary part of the former.

The color plot of the imaginary $U''(f, H)$ frequency x field spectra of a 20 nm Py can be seen in Fig.3.7. Here one can see clearly the sharp resonances following a square root function, as expected of a magnetic thin film with an in-plane easy axis. Apart from the FMR signal there are also several artifacts evolving in frequency the with the applied field - indicating they have a magnetic component. Most likely they are either resonances of magnetic coatings from the connectors and adapters and giant magneto impedance around zero field.

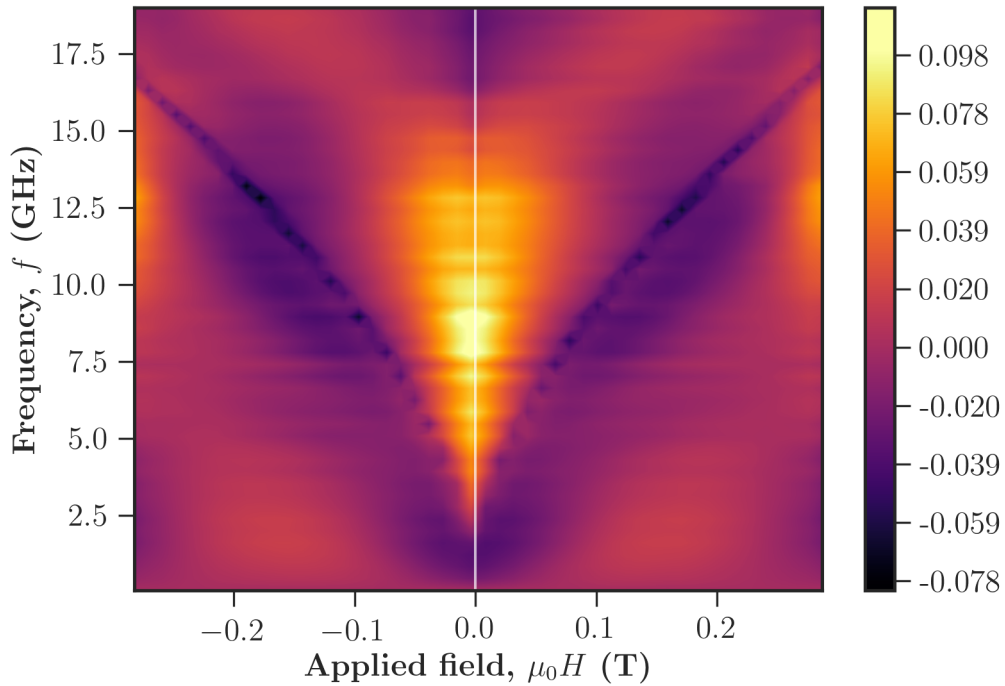


Figure 3.7: Color plot of the uncalibrated permeability $U''(H, f)$. Colors are amplitude in db. It is highlighted the origin of the applied field, indicating a slight offset in the measured field.

The next step is the to take slice per slice, and obtain the resonance field (H_{res}) and linewidth ΔH for each frequency. Normally, one would expect to fit to the following

equations³:

$$\chi'(H) = A \frac{H_{res}^2 - H^2}{(H_{res}^2 - H^2)^2 + (2H\Delta H)^2} \quad (3.17)$$

$$\chi''(H) = -A \frac{2H\Delta H}{(H_{res}^2 - H^2)^2 + (2H\Delta H)^2}, \quad (3.18)$$

where A is a parameter amplitude and ΔH is the full width half maximum (FWHM) linewidth. However, its observed empirically in the experiments a small rotation on the complex plane (see fig3.8), and needs to be corrected [38]:

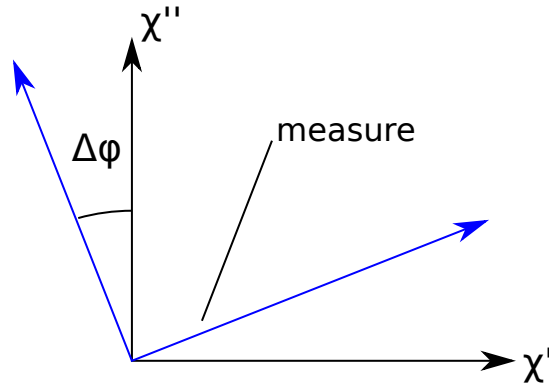


Figure 3.8: Rotation of the magnetic susceptibility complex plane observed experimentally.

$$\chi_{exp} = \chi(H)e^{i\Delta\phi}. \quad (3.19)$$

Finally, to relate to the permeability one them does:

$$U(f) = 1 + \chi_{exp} \quad (3.20)$$

Ideally, one should get the higher field possible (a proxy for infinite field), obtain $\Delta\phi$ by fitting the two equations and proceed with the other points with its fixed value. Since the lock-in experiments can only probe the the imaginary part of $U(f)$, the phase is obtained by fitting of only one spectra and may not correspond to its the actual value due to the high number of fitting parameters. For this reason, we chose to work with the VNA for the materials characterization in chapter 4.

An example of fitting can be seen in Fig.3.9. It is shown simultaneously the fit of both the real and imaginary parts of the 9 GHz slice, with 0 dbm power. The parameters obtained are in Table 3.2.

³These equations are experimentally convenient forms of equation 2.39.

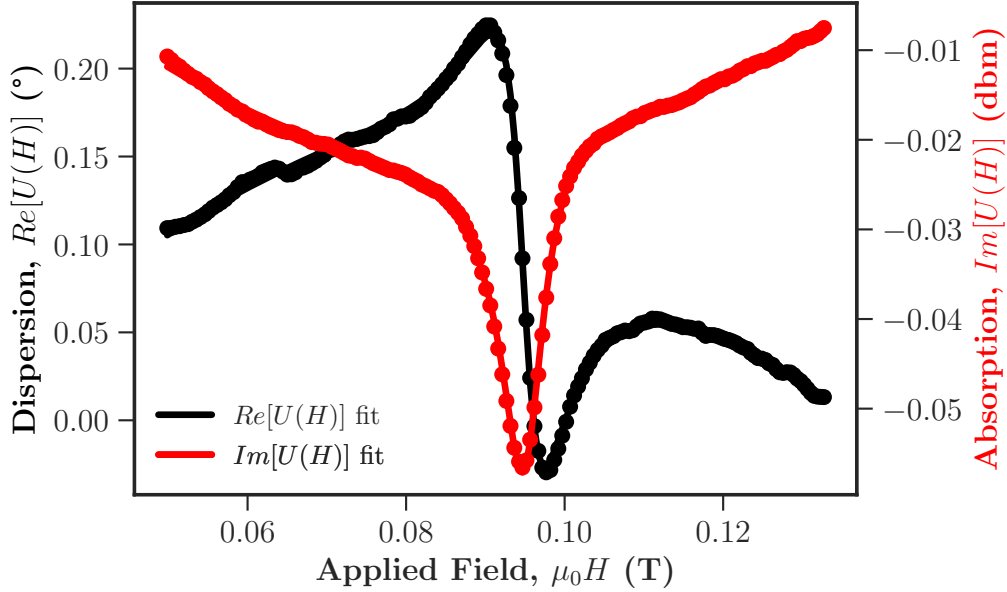


Figure 3.9: Example of non-linear fit of a 9 GHz slice of uncalibrated permeability $U(f,H)$ for a 20 nm Py thin film. The real part is shown in black and the imaginary part in red.

$U(H)$	A (10^{-4})	$\mu_0 H_{res}$ (mT)	$\mu_0 \Delta H$ (mT)	$\Delta\phi$ (rad)
Re	1.42 ± 0.01	95.05 ± 0.03	3.11 ± 0.03	14.3 ± 0.6
Im	2.32 ± 0.02	95.18 ± 0.03	3.27 ± 0.03	16.6 ± 0.06

Table 3.1: Relevant resonance parameters obtained from Magnetic susceptibility fit.

Here it is important to double check the fitting parameters, specially the phase difference $\Delta\phi$. They should be equal considering its error parameters. The bigger than confidence interval differences in the values obtained may be due to the baseline. As mentioned before, there are significant baseline signal caused by other magnetic phenomena and thermal variations at the connectors and adapters. As rule of thumb, ΔH is slightly more precise at Re spectra, in opposition to H_{res} in relationship to the Im spectra. This fact will be considered on the next stage of the analysis.

The next step is to obtain this parameters for a series of frequencies, and fit them with Eq.2.53 and 2.54. Nonetheless, it is not guaranteed that values obtained are correct. The problem was first pointed out by Shaw et al [39]. where they investigated the effect of the considered frequency spans, showing that a bigger range (up to 50 GHz) yields more accurate results for γ - errors on this variables makes for drastically higher H_a s. Another issue on the matter was demonstrated by Gonzales-Fuentes et al [40], where they calculated the error propagation for the fitting equations. They found that smaller errors in the detection of the applied field due to the positioning of the the Hall probe

accumulates to the magnetic constants quite significantly, and may give values out by 10% or more. The workaround goes by adjusting the field axis offset (see white line in Fig.3.7), evidenced by the resonances. This is achieved by simply considering for the fit:

$$H'_{res} = \frac{H_{res}^+ + H_{res}^-}{2}, \quad (3.21)$$

where H_{res}^+ and H_{res}^- are the resonances obtained respectively with a positive field and negative fields at the same frequency.

Next, the least squares fit is performed on the resulting values, for an in plane magnetized film and applied field with⁴:

$$f = \frac{\gamma}{2\pi} \sqrt{H'_{res}(H'_{res} - H'_a)} \quad (3.22)$$

$$\Delta H = \Delta H_0 + \frac{4\pi\alpha}{\gamma} f, \quad (3.23)$$

where $\gamma/2\pi$ is the gyromagnetic ratio in GHz/T, and ΔH_0 is an experimental offset value connected to internal inhomogeneities. The results for our Py example can be seen in fig.3.10, and the obtained parameters and its respective errors on table 3.2. The difference between the fits of the real and imaginary parts are not visible graphically, so just the best fit was shown - Im for the resonance fit and Re for the linewidth. One can see the obtained values are equal inside the confidence intervals. The obtained values are inside the expected at the literature for Py, with the exception of the anisotropy field H_a , that is typically found to be around 1 T [40].

	Im[U(H)]	Re[U(H)]	
$\gamma/2\pi$	29.55 ± 0.08	29.3 ± 0.1	GHz/T
H_a	-0.868 ± 0.005	-0.88 ± 0.01	T
ΔH_0	1.33 ± 0.08	1.31 ± 0.05	mT
α	3.5 ± 0.1	3.67 ± 0.08	$\times 10^{-3}$

Table 3.2: Magnetic parameters obtained from the 20 nm Py fit.

⁴see section.2.5.3

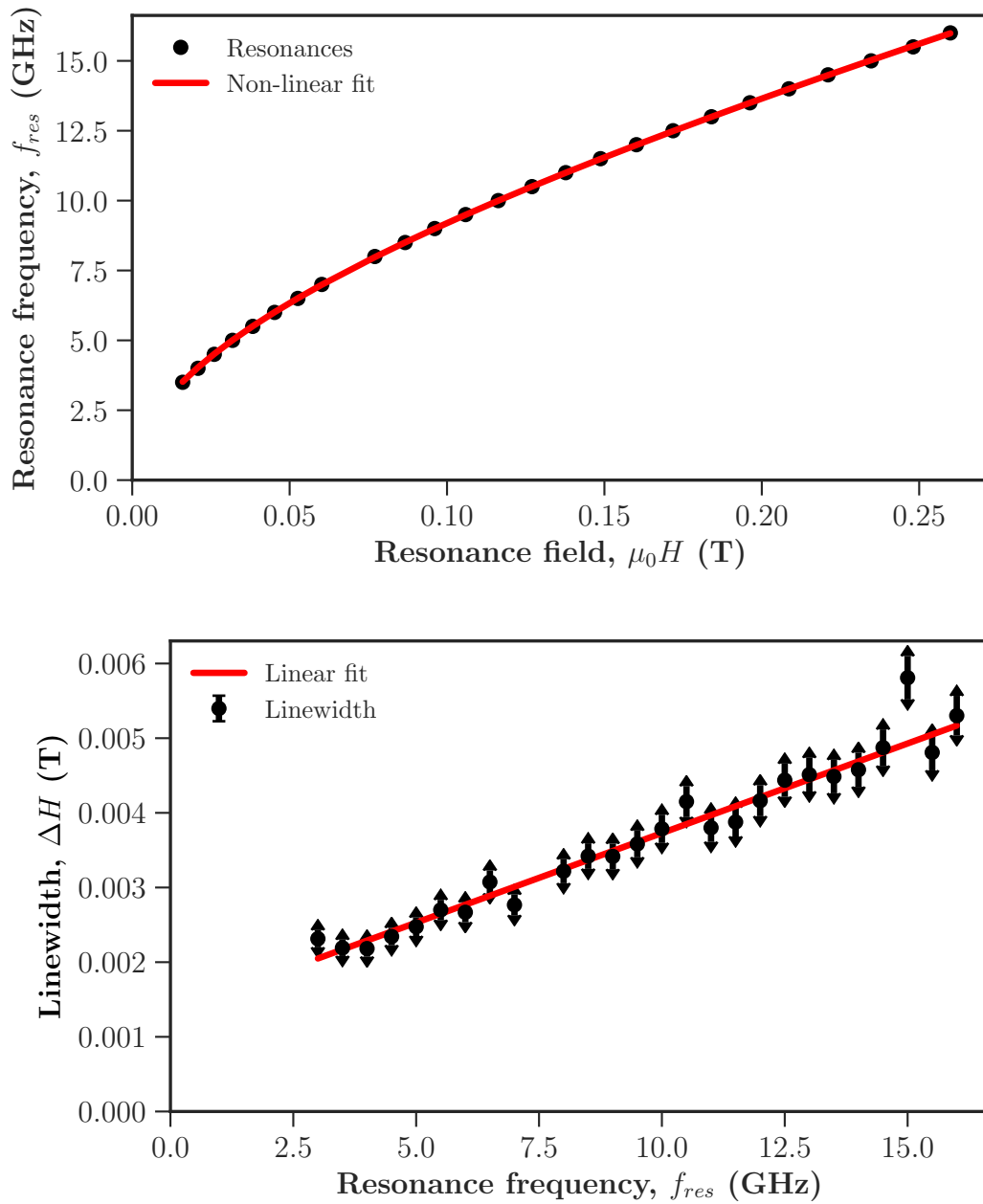


Figure 3.10: Py 20 nm final non-linear fits for obtaining the magnetic parameters.

3.3 Interferometric BBFMR techniques

The Nanomagnetism division at INRIM is part of a Joint Research Project within the European Metrology Research Programme EMPIR entitled the Metrology of Topological Spin Structures (EMPIR-TOPS). One of the main activities of the project is a round robin to establish the accuracy of obtaining the Dzyaloshinskii-Moriya interaction (DMI) [41, 42] constant using different experimental methods⁵. Among them there are methods utilizing asymmetric propagation of spin waves, a similar experiment to the BBFMR. Here, a spin wave is propagated from right to left, and vice and versa, on a ferromagnetic material with DMI. A slight difference in spin-wave resonance frequency is verified between the propagation directions caused by the DMI. To extract the DMI constant from this frequency variation [43], one needs to utilize both γ and α - which are commonly obtained by BBFMR characterization.

The biggest disadvantage of the BBFMR techniques is that the measured absorption may be several orders of magnitude smaller than the detected signal, and in most of the cases is lost due to an overload of the dynamic range of the Lock-in amplifier or the VNA. Moreover, the absorption amplitude scales with the volume of the probed sample, and thus the thickness of the sample is directly linked with the final sensitivity of the measurement. One of the pre-requisites of the interfacial DMI to be present in thin films is the broken symmetry between the upper and bottom interfaces and thus thickness below 2 nm are often employed. Consequently, they are very hard - if not impossible - to measure by conventional BBFMR techniques.

Inspired by the EPR experiment, where the signal measured is in principle only the absorption of the FMR, recently there has been some interesting developments in adapting interferometric techniques for the BBFMR experiments [44, 45, 46, 38]. The idea is to divide the input microwave signal in two arms, one with the sample and one without, and make them interfere destructively before measuring at the VNA or Lock-in. In this way, the dynamic range is better employed only to measure the absorption, and if needed, extra amplification might be used. In fact, in the VNA interferometer designed by [45], claimed a 43 db improvement in signal to noise ratio, by systematically taking care of each source of noise.

As part of the TOPS project, I spent a period at the Physikalisch-Technische Bundesanstalt in Braunschweig - Germany. Supervised by Drs. Sybille Sievers, Mark Bieler and Hans Schumacher, I implemented the lock-in type interferometer, to further characterize the ultra thin (< 2 nm) HM/CoFeB/MgO samples of the Round Robin. The choice of the Lock-in type interferometer [46] was due to the modularity and simplicity of the implementation. Here, the interferometry is done after the diode rectification, so the wave manipulation is done in the RF (KHz) regime, without the need of expensive microwave dedicated components. Moreover, the Lock-in already has a two port differential input,

⁵The DMI is given by $D\vec{s}_1 \times \vec{s}_2$, where D is the DMI constant, and \vec{s}_1 and \vec{s}_2 are neighboring spins

so no phase manipulation between the two arms is required.

3.3.1 Lock-in type interferometer

The scheme of the experiment can be seen on Fig.3.12. The main difference from the BBFMR-Lock-in setup described in section 3.1.1 is the second arm used for the interference. The AM modulated microwave is first divided by a power divider, then one of the arms goes to the CPW and sample and the other serves as a reference. The reference arm incorporates an identical diode detector as the sample arm plus and L-pad resistive attenuator (Fig.3.12). The two arms are connected at the channel ports A and B of the Lock-in Amplifier and the differential input mode is chosen. In this input mode, the signal from both channels is subtracted before any stage of raw signal manipulation of the Lock-in (filters, amplification, digital to analog conversion). The attenuator is then used to imitate the attenuation of the sample, connectors and CPW, focusing the Lock-in amplifier dynamic range to work optimally in the scale of the FMR absorption.

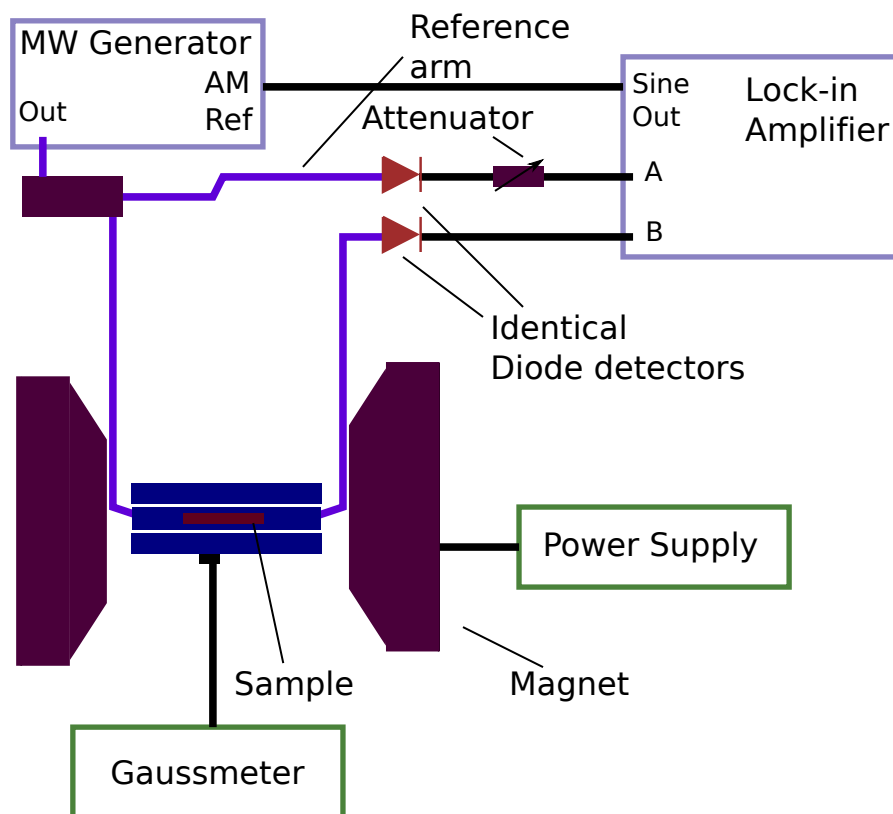


Figure 3.11: Scheme of the Lock-in based interferometric BFMR experiment. The connections in purple are done by u.h.f(GHz) cables and connectors, while the ones in black with standard RF (KHz)

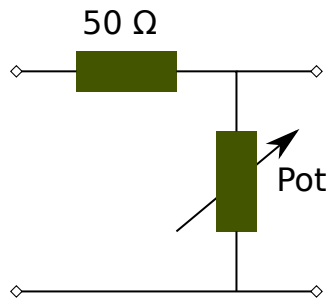


Figure 3.12: L-pad type attenuator. The ideal potentiometer to be used is a multiturn, to allow a more precise control of the resistance.

First experimental implementation and optimization

We initiated the process by assembling the Lock-in interferometer in a microwave probe station inside of a electromagnet (see Fig.a3.13). The probe station is composed of a 3-terminal probe that makes contact superficially with the CPW, instead of using typical end launch coaxial connectors⁶. This was done in order to employ the same batch of samples used in the VNA interformeter work published at PTB[44]. The samples are 20 nm thick Py thin films with fixed length and varying width in a wafer substrate (see Fig.3.13b). Since the FMR absorption is proportional to the volume, variations in width may be used to simulate different thickness.

At Fig.3.14 it can be seen the effective comparison at 5 GHz of a continuous 0.5 mm stripe measuring only channel A (conventional BBFMR-Lock-in), and the interferometric A-B. The attenuator was set to remove only 1 db (10 times) out of the sample arm (channel A), and the results are already impressive.

⁶For more information on point probes please refer to

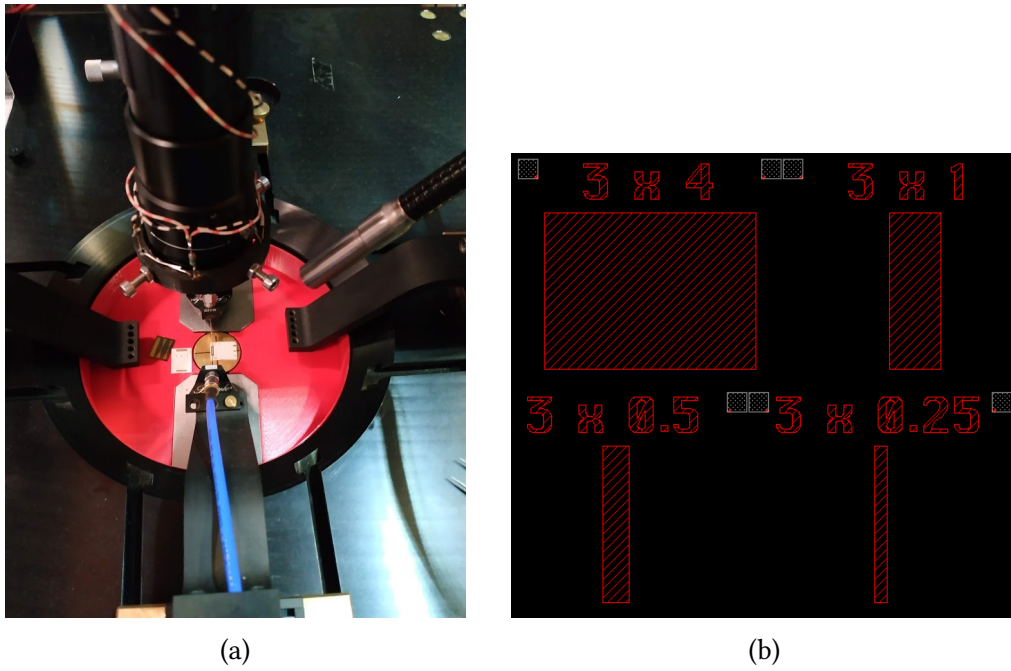


Figure 3.13: a) Point probe station. b) 20 nm thick Py stripes with varying widths. Numbers are in mm.

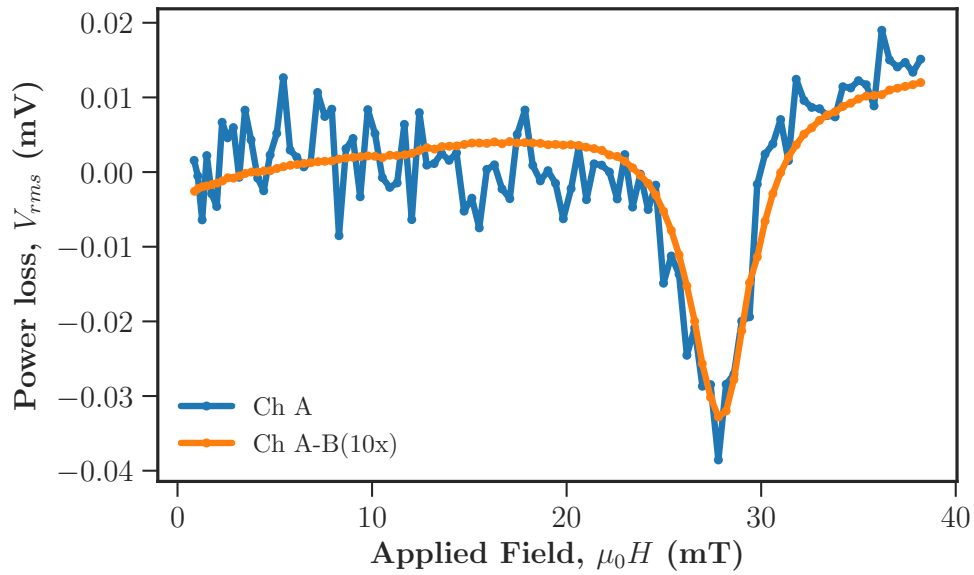


Figure 3.14: Comparison between measuring only the sample arm (Ch A) against the subtraction from the reference arm (Ch A-B). Py sample width of 0.5 mm.

The full batch of absorption at 5 GHz with different widths can be seen in Fig3.15. One can see the decrease in absorption amplitude due to decreasing probed volume, and below 1 mm width the SNR was degraded considerably. An optimization "sweet spot" needs to be found. The parameters that can be optimized are: the amplitude compensation of the reference arm, the AM modulation frequency, the lock-in time constant and the total MW power applied to the system.

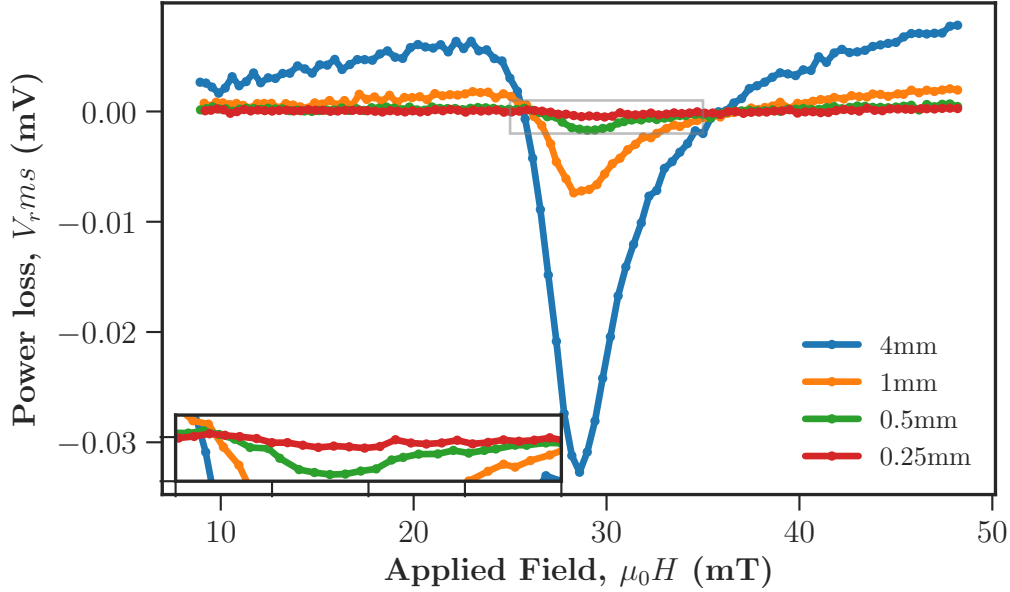


Figure 3.15: Effect of decreasing the width of the stripe in contact with the CPW. No signal at 0.25 mm

The reference arm amplitude is individual to each measurement, due to the CPW dimensions causing a frequency dispersion. The result is a change in the baseline measured power (away from the absorption) from the sample arm from frequency to frequency. Since the A-B channel does the subtraction at the first stage at the input, the reference arm cannot be set compensate exactly the sample arm: if the Lock-in receives zero resultant signal, it cannot perform the signal processing needed⁷. Also, if the baseline power is smaller than the the absorption peak, the Lock-in phase will change during the measurement, distorting dramatically the shape of the absorption. Hence, the reference arm needs to be adjusted for each performed measurement whenever the frequency is modified and not fully to allow proper functioning of the Lock-in amplifier.

⁷see section 3.1.1

The MW power is the parameter with biggest potential to improve SNR in MW measurements, and is of the same importance to the reference arm compensation in interferometric experiments. The higher the input power, the higher the ratio of the measurement and random noise will be. However, one of the main conditions of the FMR discussed in section 2.5 is that the induced precession by the excitation field does not change significantly the projection of the magnetization around the static field ($M_z \approx M_s$). Otherwise, it is verified by increasing the power at first by an enlargement of the linewidth, followed by an secondary absorption peak formation [47]. So, by increasing the power over a certain limit, an actual loss in the SNR is seen for FMR measurements. The ideal MW input power was found to be 0 db and we managed to properly obtain the absorption peak of the 0.25 mm length sample with outstanding sensitivity as can be seen in Fig.3.16.

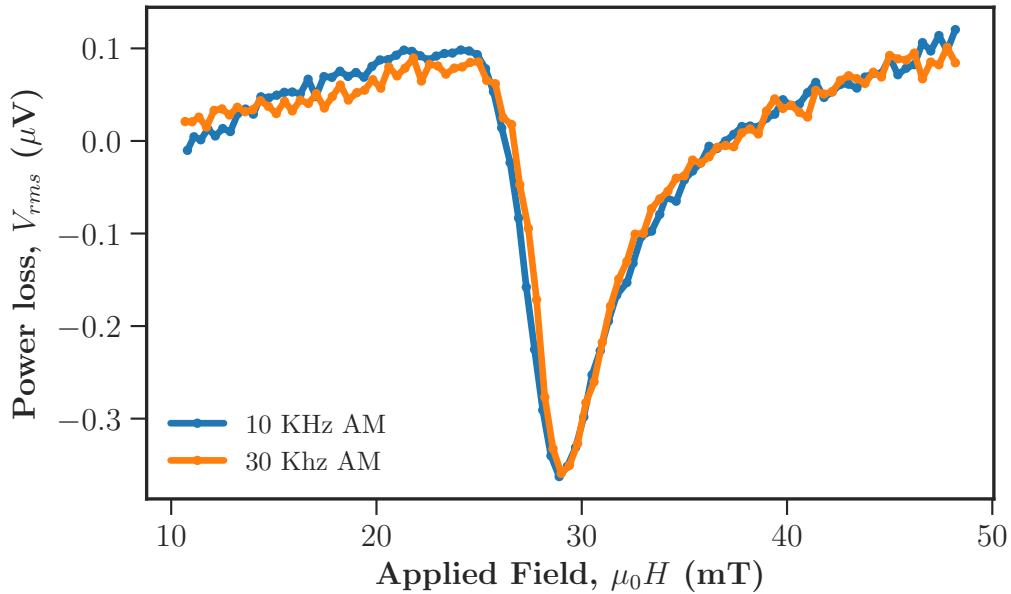


Figure 3.16

The time constant (TC) is basically the averaging of the signal over the multiple RF periods contained in the AM modulation frequency⁸. A TC of 0.1 S is then the same as averaging 10 thousand times the measurement at 1 KHz. Hence there is not much room for improvement at the cost of increased measurement time. As a matter of fact, by increasing above 10 KHz of AM, artifacts from the L-pad attenuator starts to appear due to its frequency limitations (see Fig.3.16).

⁸see section. 3.1.1

Second implementation: Southwest connectors and water-cooled electromagnet

The probes station setup has several limitations. First, the procedure to touch down the point probe on the CPW inevitably damages it, to a point to render the CPW useless after a few iterations. Second, in our case it only allows small static magnetic fields, due to the size of the gap between the poles of the electromagnet - also limiting the sample filling size and probed volume. Since the samples needs to be magnetically saturated for the FMR, the electromagnet is necessary to be capable of a wide range of field values to account for the varied anisotropies of different magnetic materials.

We then transferred the experiment to a bigger water cooled electromagnet (see Fig.3.17a), capable to apply up to 2 T, and with the end launch Southwest connectors. They are BeCu military grade connectors, are extremelly resistant to fatigue and have similar insertion losses to the point probes(see Fig.3.17b). Although the decrease in volume by length should be the equivalent to a decrease in thickness, we chose to deposit a 3 nm thick Py thin film to directly verify a sample with reduced thickness. This also accounts for the increased sample filling factor provided by the bigger electromagnet and connectors, being closer to the experimental conditions for the round robin samples.

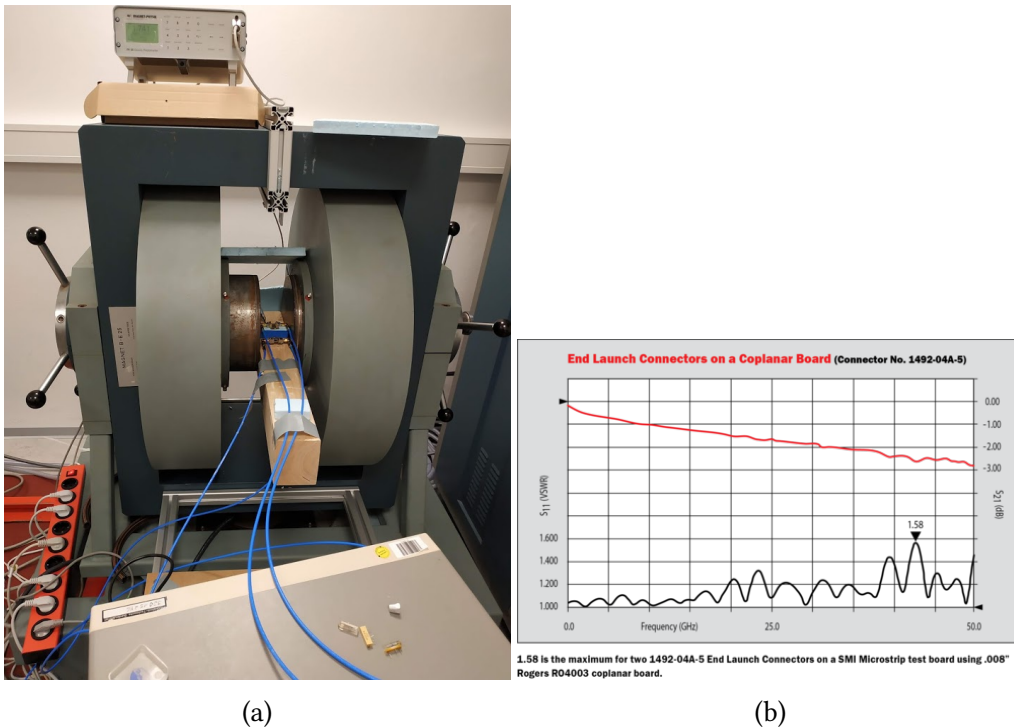


Figure 3.17: a) Photo of the actual setup inside the electromagnet. b) Southwest connectors input loss.

A comparison spectra of the 3 nm Py thin film at 9 GHz between the Lock-in interferometer and a BBFMR-VNA (same procedure as in Section.3.1.1) with a state of the art VNA Rode-Schwarz can be seen in Fig3.18. The interferometer improves the SNR approximately two-fold against BBFMR-VNA. The measurement was performed at 0 dbm MW power and around 34 dbm was removed from the baseline. As with the point probes setup, the results are again very optimistic.

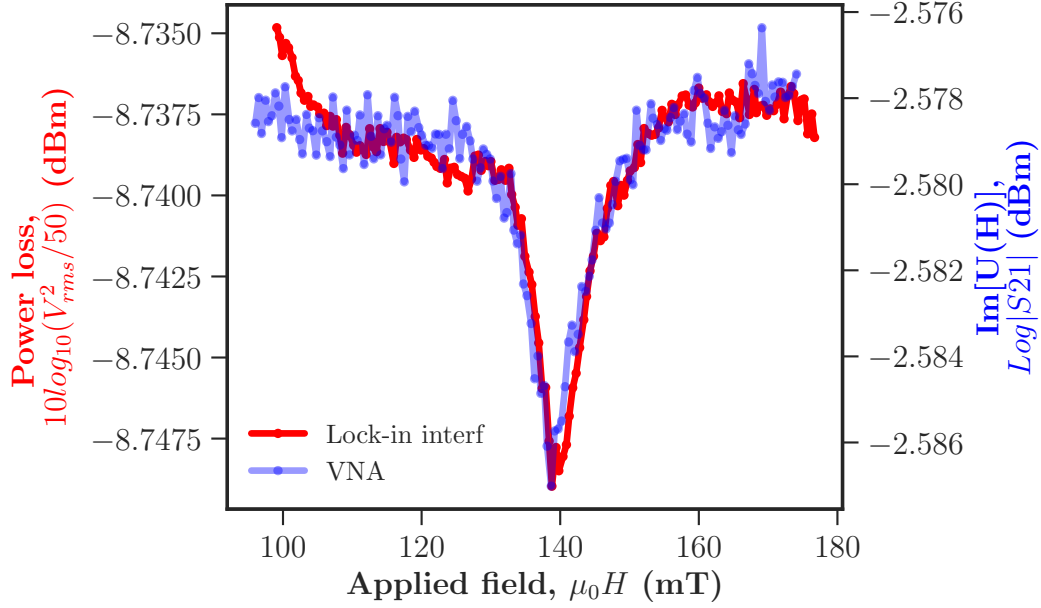


Figure 3.18: 5 GHz spectra of 3 nm thick Py film. a) Lock-in interferometer. b) VNA Rode-Schwarz

The uniaxial anisotropy fits⁹ for the 3 nm Py resulted in: $\gamma/2\pi = 29 \pm 1$ GHz/T, $H_a = -0.56 \pm 0.02$ T, $\Delta h = 0.28 \pm 0.06$ mT and $\alpha = -5.9 \pm 0.7 \times 10^{-3}$. Out of those, only the anisotropy field H_a differs from the literature accepted value of 1 T. This is mainly due to effects of the OOP interface anisotropy which increases as a factor of $1/t$ with the thickness. Moreover the magneto elastic and crystalline anisotropies might also be present and competing to a certain degree, and further structural characterization of the sample is needed to draw a full model on this regard.

⁹Not shown. The procedure was given in the last sections, and there is no observable differences from the graphs alone. The information is basically contained on the results of the minimum square fit.

Final sensitivity considerations and limitations

In order to generalize the 3 nm thick Py results to other samples, it is important to establish the relationship of the expected absorption amplitude in respect to the magnetization saturation M_s and the linewidth ($\propto \alpha$). The absorbed power P_{abs} is given by the real part of Eq.3.1. Since the sample is saturated, and we assume the fields to be homogeneous inside the sample, we can integrate on the volume and obtain:

$$P_{abs} = -\frac{1}{2}2\pi f \chi'' h_{rms} V \quad (3.24)$$

χ'' is then given by Eq.2.39. At the resonance, $H_{res} = H$ and after some simple algebraic manipulations we have:

$$\chi''_{max}(H) = \frac{\gamma \mu_0 M_s}{2H \Delta H} \quad (3.25)$$

Now, ΔH is given by Eq.3.23. ΔH_0 is an experimental variable, which depends mainly on the inhomogeneities of the sample, or its imperfections. It cannot be predicted experimentally, and it is typically a few times smaller than the total linewidth. For the sake of the argument¹⁰, it will be approximated to zero. Putting all together, one can find:

$$P_{abs} \approx -h_{rms} \frac{1}{2} \frac{\gamma}{2\pi} \frac{\mu_0 M_s}{\alpha} V \quad (3.26)$$

h_{rms} is directly related to the input MW power, and it was already discussed the limitations of optimizing this value. $\gamma/2\pi$ ranges of about 5% difference between Co,Ni,Fe so it is not responsible for big changes from sample to sample. Thus, the important relation to be compared to the baseline noise is the relative amplitude A_{rel} dependent of the volume V , the magnetization saturation M_s and the Gilbert damping α :

$$A_{rel} \propto \frac{\mu_0 M_s V}{\alpha} \quad (3.27)$$

At this point, it is good to remember that A_{rel} is only a guideline for comparison, since ΔH_0 and other anisotropies different than shape anisotropy were not considered. In any case, this would decrease its value even more, so it is good practice consider the requirements for A_{rel} s a few times bigger than the baseline noise.

The round robin series of samples are Ta/CoFeB/MgO with below 2 nm thicknesses. Similar samples can be found in the literature [48] to have $\mu_0 M_s \approx 1.88T$ and $\alpha = 0.02$. Comparing with the 3 nm Py values obtained in the last section, they have around double $\mu_0 M_s$ and ten times more α . Thus we can expect at least 5 times less signal.

¹⁰see section.2.5.3

The obtained SNR for Py was around 5, and considering extra room for non accounted unpredictable variables, it should not be enough to measure it. As a matter of fact, we did not find any meaningful data after several weeks of extensive experimentation.

The question to be made is what are the sources of systematic noise of the system, and how to enhance it even further - to around one order of magnitude. The connectors, cables and CPW can certainly be improved but all together could account for at most a few percent. Fluctuations in the input MW signal during the measurement sweep could also be an issue. All in all, this systematic errors in principle are accounted by the interferometry, and furthermore the Lock-in is already working optimally. An insight can be given by referring to Fig.3.18a), from 30-40 and 60-70 mT (away from the absorption). The oscillations seem here are common from temperature variations, and in fact the order of magnitude is in line with what is expected by 0.5 °C in Copper (from the CPW conductors). Could it be then by inserting the experiment in a Cryostat and precisely controlling temperature would solve the issue? It is unlikely. The order of magnitude of oscillations are already below what is guaranteed by the diode detector datasheet ¹¹. The main problem is that the interference is done after the rectification process of the diode detector, so **the sensitivity is ultimately limited by the diode dynamic range**. In other words, the FMR peak is again only a small part of the signal detected by the diode. The interferometry is then not being used in its full potential.

Other BBFMR interferometric experiments depends on the VNA, but the MW from port 1 has to be manipulated - amplitude matched and phase inverted - before arriving at the Port 2, increasing considerably the complexity of the setup. One simple solution would be to add an extra length of cable on the reference arm and verify in which frequencies there are destructive interference, and use it in the continuous wave mode with field sweeps. This would change from sample to sample though, once its electric length is changed by the new sample + CPW system. This approach was used at PTB in a previous work [44], and the same set of Py mentioned in the point probe analysis in this thesis were used. It worked, but they found artifacts caused by slightly off destructive phase interference. Moreover, at MW frequency, the impedance needs to be matched, and continuous attenuators like the L-pad type we used are not available, so the amplitude compensation will not be as precise. In the Tamaru work [45], the one with the most impressive improvements of SNR, they do not specify what was used for the phase manipulation. The instruments available in the market are not broadband, typically spanning a few GHZ, inside the known MW band standards. In fact, also their measurements seems like to be done only at the C band. Finally, in defense of the VNA type interferometry, the VNA has around one third more dynamic reserve than the diode detector and certainly is worth to keep pursuing solutions of the mentioned problems.

¹¹8474C Planar-Doped Barrier Diode Detector, 0.01 to 33 GHz

Nonetheless, optical techniques as the TR-MOKE [48] had been successfully employed for investigating magnetization dynamics in ultra thin films. They also utilize interferometric concepts, are commercially available and thus are far more suitable tool to such small signals - if the considerably higher budget is available.

Chapter 4

Amorphous FeSiB dynamics

4.1 Introduction

Magnetic amorphous and nanocrystalline alloys are present everywhere in our lives. Miniaturized power supplies, digital compasses, motion detector in smartphones, hard drives were possible due to the high customization of magnetic parameters of this class of materials controlling their structure in the nanometer scale, made possible by tweaking the stoichiometry and thermal annealing.

A material is considered amorphous in absence of a periodic structure. In real conditions though, there is no such thing as a completely disordered structure. Inevitably small crystalline volumes are formed, with random preferred magnetization directions. In the case of ferromagnets, due to the strength of the exchange interaction, there is a minimum distance at which spins are allowed to tilt from neighboring ones - called the exchange length. If the crystalline volumes are then smaller than the exchange length, the magnetization is not able to follow its local anisotropy directions. In the case of Co or Fe, the resultant crystalline anisotropy energies are of the order of $1 \times 10^{-1} \sim 1 \times 10^{-6} \text{ J/m}^3$. Consequently, incredibly low coercivities are found, wielding very soft magnetic materials [49].

The main principle to take in consideration when trying to produce amorphous metals is the viscosity η . In the liquid state, η is at the order of 10^{-2} Nsm^{-2} against 10^{11} Nsm^{-2} when in the solid state. If the quenching rate is sufficiently low to consider each temperature step at equilibrium, the sample will fully crystallize near the melting temperature. Since this temperature is quite high, the amplitude of thermal vibrations will allow the metal atoms to move and form metallic bonds in on a longer scale, producing large crystals. On the contrary, if the quenching rate is high, the liquid will solidify in a lower glass temperature. In the interval between the melting and glass temperature, the system is in a thermal meta-stable equilibrium, forming an under cooled liquid. In this liquid state, the viscosity does rises exponentially from the melting to glass temperature. As such, when the solidification occurs, the atoms are not allowed to move much and form many bonds. Thus the crystals formed have negligible size, resulting in

a amorphous state. In order to attain such fast quenching rates, the lower the melting point temperature the better. This is achieved by looking at the eutectic points in alloys combining transition metals and metalloids in a ratio of approximately 80 to 20. Lower melting temperatures combined with atom size difference and non metallic bonds formed by the metalloids introduction both contribute to the amorphisation process [49].

By using Fe, Co or Ni, as TM, one then can make amorphous magnetic alloys. At the cost of a decrease in the magnetic moment due to the d-shell electrons being occupied by the metalloids, the crystalline anisotropy becomes negligible. Nevertheless, the internal stresses created during the quenching process give rise to magnetostriction - contributing to its own anisotropy. In Fe alloys, this may reach $10^3 Jm^{-3}$. The internal stresses can be relaxed by thermal annealing below the recrystallization temperature. Also, in these amorphous alloys, the magnetostriction of the amorphous matrix and the grains have opposite signs, and can be tuned to compensate each other, even with nanometer scale grains. Thus one can fine tune grain growth by adding a small amount of non magnetic TM, such as Cu or Ta - increasing the nucleation rate and hindering the growth rate. The result is near zero total magnetic anisotropy, high permeability and higher magnetic moment compared to the fully amorphous counterparts. Another consequence is high resistivity, making them ideal materials for inductive applications such as inductors and transformers.

These materials were mostly investigated in structures like tapes or wires, facilitated by the production method and with industrial applications in mind. The fabrication process consists on the melt spinning technique, in which a drum rotates rapidly receiving the melted alloy in one side and is water cooled in the opposite side. The process produces meters and meters long samples, and the annealing can be done in commercial ovens, making the whole field extremely industrially friendly.

Thin films or flat wires, may also be fabricated by deposition. The thin films deposition techniques naturally have fast quenching rates, since the film is formed from the gaseous directly to the solid state. If the substrate is kept at a constant low temperature, by water cooling, amorphisation can be achieved. The reduced thickness opens up several new phenomena such as interfacial effects and strong shape anisotropy. Due to the sample high tunability of magnetic parameters, amorphous magnetic thin films are excellent specimens for research. For example, one can eliminate the crystalline and isolate the competition of shape and magnetostriction anisotropy or reduce the thickness to a few nm range, so interfacial effects become dominant.

One of the most studied amorphous magnetic thin films is CoFeB, that presents near zero magnetostriction and crystalline anisotropy. The presence of Co decreases the total magnetic moment, resulting in a weaker in-plane anisotropy due to shape. Together with the reduced thickness and with the addition of an adjacent oxide or heavy metal layer, interfacial anisotropy effects are enhanced by spin orbit coupling, allowing

the out-of-plane anisotropy to overcome the in-plane anisotropy, forming a perpendicularly magnetized anisotropy (PMA) film¹. CoFeB/MgO PMAs have been extensively used to investigate new physical phenomena like spin orbit torques and Dzyaloshinskii-Moriya Interaction, resulting in new technologies that might be applied in the sensors and digital storage market. However, the spike in Co demand has high economical, social and environmental costs. Thus research in finding Co free alternative alloys might not only be useful in reducing producing costs, but also solving potential political conflicts.

4.1.1 Fe-Si-B amorphous alloys

Fe-Si-B alloys were first investigated in the end of the 1970s, in search of materials to be used as transformers cores and inductors. A major problem with Fe-B amorphous alloys known at the time was their stability at room temperature, due to its low Curie temperature T_c . Typical M_s values decreases of about 22% in the range of 77 ~ 300 K, and the highest value found is 180 emu/g[50].

Si can then be added to make the system more thermally stable, raising the T_c . Consequently, the onset of crystallization is increased by 100 K to a maximum of 750°C [51]. Moreover, Si greatly increases the amorphisation range of conditions. However, it does donate 3d electrons to Fe, which also affects negatively the M_s . By keeping Si content low, one can get only a M_s decrease of only 1% from the optimal $Fe_{80}B_{20}$ at $Fe_{82}Si_6B_{12}$ [50] is observed. A modern study on several ribbons from this family of alloys, by Yue et al [52], investigated the cooling rates thoroughly confirming these old findings. As expected the amorphisation depends on the cooling rate, and ultimately the iron content of 71-86% of Fe. A phase diagram for these alloys can be found in [53].

The rapid cooling of these alloys leaves them in a metastable state, generating internal stresses. In fact, the amorphous phase produces an isotropic magnetostriction, and it was reported positive constants up to $\lambda_s = 36 \times 10^{-6}$ in ribbons [54]. With thermal treatment, the internal stresses can be slowly released, until the onset of crystallization. The nanocrystal's phase may be FeB or $\alpha - Fe(Si)$, depending on the iron content, and typical size is about 17 nm [54, 53].

Thin films can be deposited with these alloys, as long as the substrate is kept at a constant low temperature by water cooling it. They have been widely studied in the thickness range of 100 to 300 nm in [54, 55, 56, 57, 58]. They can achieve magnetostriction constants up to $\lambda_s = 6.50 \times 10^{-6}$ and have the same remarkable tunable magnetic properties by thermal annealing as their melt-spun ribbon counterparts. Coercivities were found as low as 0.4 mT by thermal treatment in the range of 200 ~ 390°C.

A series of works on the commercial composition $Fe_{79}Si_9B_{13}$ amorphous alloys in thin films was published by Coisson et al [59, 59, 60, 61]. They present a well defined

¹The amorphous state is not a prerequisite to PMAs

weak stripe domain structure, with OOP components - that can be tuned by the film thickness and thermal treatment. In the most recent paper, the films were investigated by BB-FMR [61] and a complex set of modes was found when the sample is in the stripe domains state. In this chapter we investigate those modes, together with a fully fledged FMR analysis.

First we summarize the already published results of structural and hysteresis curves characterization, and then we present new data from the BB-FMR and micromagnetic simulations on the modes.

Structural and Composition analysis

The FeSiB thin films were deposited by rf sputtering on a water cooled Si_3N_4 substrate. The base pressure was 10^{-7} and Ar pressure 10^{-2} mbar. Power was kept constant at 50 W. The target consists in amorphous $Fe_{78}Si_9B_{13}$ tapes produced by melt-spinning. Originally they were deposited in thin films ranging from 25 nm to 600 nm thickness. On this thesis only the range of 80 nm to 300 nm will be considered [62].

The constant refrigerating of the substrate due to the water-cooling impedes movement of the cluster of samples arriving at the substrate, keeping their amorphous status from the target. The films internal structure was verified by x-ray diffraction, and no sign of crystallinity was seen below $t = 150nm$. Above $t = 300$ nm some crystalline volume with bcc $\alpha-Fe$ can be seen, but a reliable quantification was only possible above 600 nm [59]. Also, an increase of Fe/Si ratio was observed in the EDS-SEM analysis, indicating a slight B decrease in the deposited samples.

The thickness was verified by measuring a step on the film by both a profilometer and atomic force microscopy.

Static Magnetic Characterization

The magnetic characterization of the set of FeSiB films was performed using an alternating field gradient magnetometer [8] and a magnetic force microscope (MFM).

The hysteresis curves of films with different thickness are shown in Fig4.1 a). All the samples have a dominant in-plane (IP) anisotropy, caused by the demagnetizing field (shape anisotropy). In the films with $t=150, 230$ and 300 nm, the magnetization presents peculiar shape called transcritical loop [63], due to the competition and superposition of an OOP anisotropy on the expected IP one. This effect is evident in the magnetization curve just before reaching magnetic saturation. OOP anisotropy derives from the film magnetostriction and it is driven by the internal stresses quenched in the film during the sputtering deposition and also from the structural mismatch caused by the presence of Si and B atoms which have different crystal lattice parameters, causing an isotropic magneto-elastic (m-e) anisotropy. By annealing the film for 60 min at temperatures T ranging from 200 to 325 °C, temperatures well below the crystallization temperature of 375 °C [59], the system is allowed to relax and the m-e anisotropy progressively

decreases. This effect is shown in Fig.4.1b for the 230 nm thick sample, where the magnetization curve progressively returns to a square shape (with high remanence) after annealing at higher and higher temperatures.

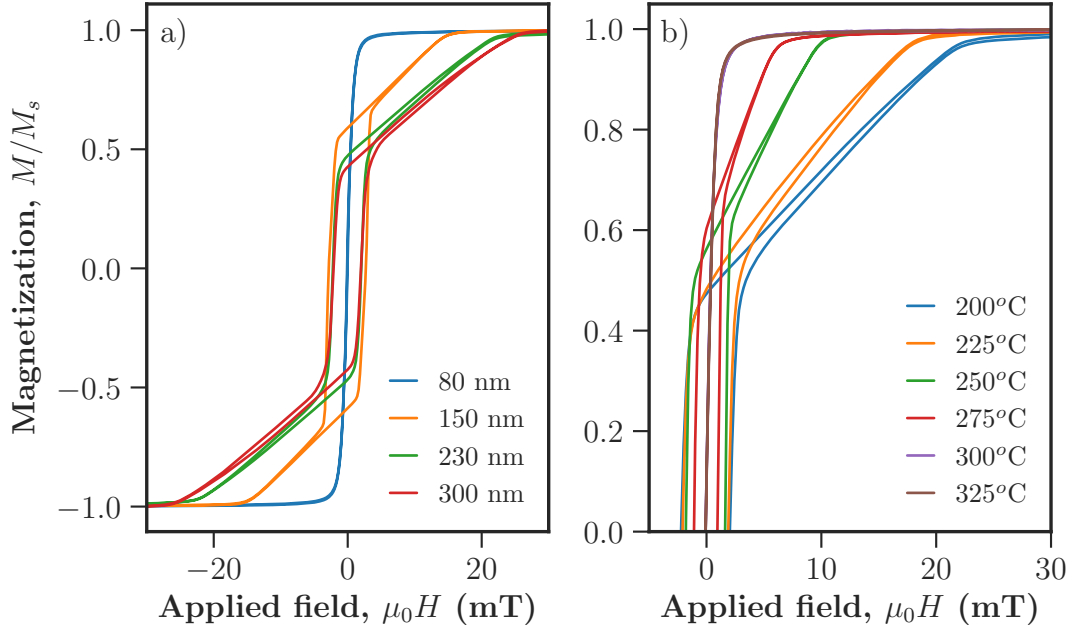


Figure 4.1: Hysteresis curves for a) different film thicknesses and b) different annealing temperatures (60 min) on the 230 nm thick sample.

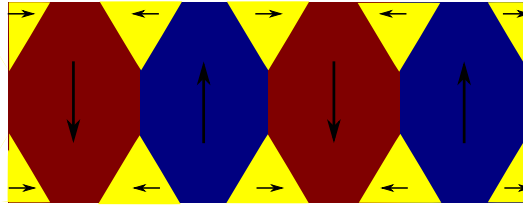


Figure 4.2: Diagram of the expected domain profile in a cross section of the FeSiB film at remanence, in the presence of stripe domains with alternating OOP magnetization.

A further investigation of the origin of this peculiar linear magnetization dependence on field region observed in films with quenched-in stress was conducted by analyzing the magnetic domain patterns using MFM imaging[60, 61]. For samples with $t=150$ and 230 nm, stripe domains were observed, with an OOP magnetization component, and with alternating up and down magnetization regions separated. A sketch of the magnetization directions within magnetic domains is shown in Fig. 4.2.

In summary, increasing the sample annealing temperature decreases the magneto-elastic contribution of the OOP anisotropy. When we have an adequate ratio of OOP anisotropy contribution due to stress and the shape anisotropy, well defined perpendicular stripe domains can develop, as in the $t=150$ and 230 nm, while in the $t=300$ nm these domains are present but not well structured. In the $t=80$ nm samples, due to its reduced volume, no transcritical HxM curves is seen, and consequently no stripe domains structure.

4.2 FeSiB Ferromagnetic Resonance

In this thesis we investigated the microwave magnetic properties of the above mentioned FeSiB film samples through the analysis of magnetic damping and the anisotropy using FMR experimental techniques, which can provide an accurate analysis of magnetic anisotropy and magnetic losses at high frequency (Gilbert damping).

4.2.1 Analysis of FMR results

The FMR experiments were performed by applying a saturating magnetic field of 300 mT parallel to the film surface by means of a variable gap electromagnet and then slowly decreasing the field in 5 mT steps down to 0 mT (80, 300 and 150nm samples) or down to -300 mT (230 nm sample only). At each field step, a frequency sweep was performed using the Vector Network Analyzer, then the VNA data collected at each field step was processed to convert the frequency sweep data to a format equivalent to field sweep data, using the procedure described in the previous Chapter 3. This step was applied in order to remove measurement artefacts frequently observed in frequency sweep data.

The FeSiB thin film samples with $t=150$ nm, 230 nm and 300 nm present stripe domain patterns which were observed by MFM imaging [61]. Here we show, as a representative set, the samples with $t=230$ nm after the six annealing treatments. These films present several FMR absorption modes at low applied field (and corresponding low frequencies), which tend to collapse into a single FMR mode once the sample reaches magnetic saturation (Fig.4.3). The field/frequency value where only a single FMR mode is found tends to decrease with increasing annealing temperature, an indication that the additional modes are connected to internal stresses and magneto elastic energy as spatial magnetic inhomogeneities, preventing the onset of a single uniform FMR mode in the whole sample. It should be noted that multiple absorption modes are only found when stripe domains are present, as is the case with $t=150$ nm, 230 nm and 300 nm samples.

The stresses are induced during the film deposition, due to different thermal expansion coefficients between the silicon nitride substrate and the film material as well

bending of the substrate during deposition due to the mechanical holder. Thermal annealing tends to enlarge the size of stripe domains, and they progressively become irregular with increasing annealing temperature, to the point where the MFM is not able to detect the stripe domain features any longer[61].

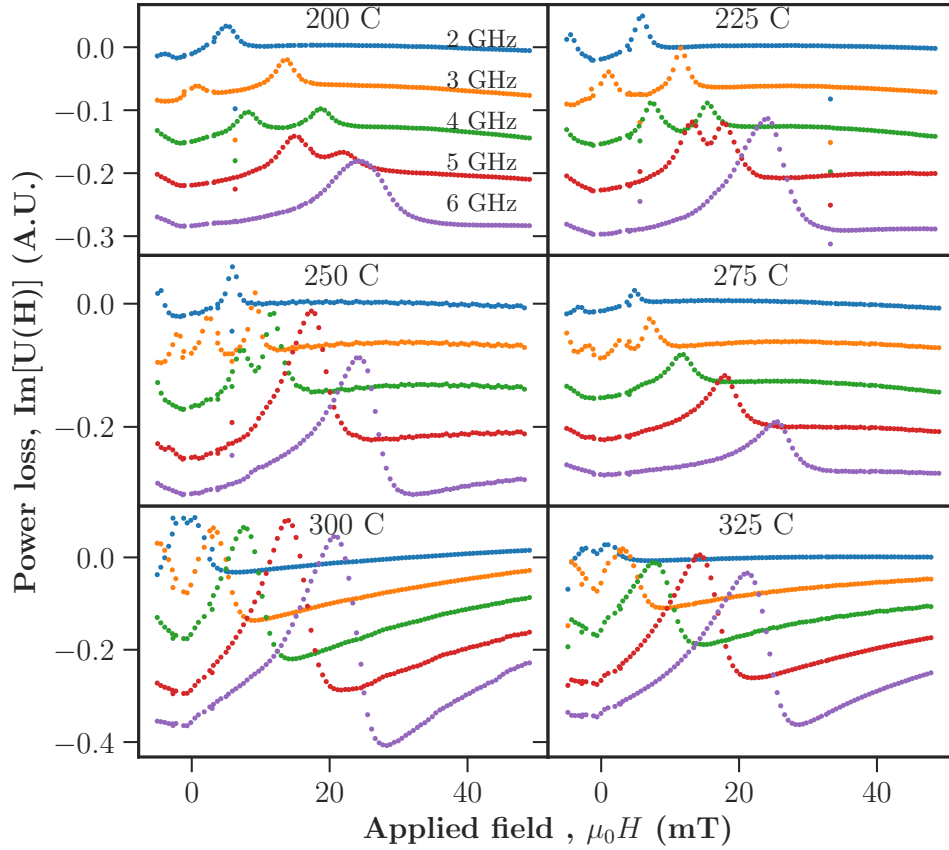


Figure 4.3: Series of FMR absorption peaks measured from 2 to 6 GHz on the $t=230$ nm sample. From left to right, top to bottom: annealing temperatures= 200, 225, 250, 275, 300, 325 °C.

A color plot of the FMR behaviour of the 230 nm thick film after a 200°C annealing is shown in Fig.4.4. Above 6 GHz a single FMR mode is found, and the frequency dispersion corresponds to a typical film sample with a dominant in-plane uniaxial anisotropy, which can be analyzed according to the analytical procedure described in Section 3.2.

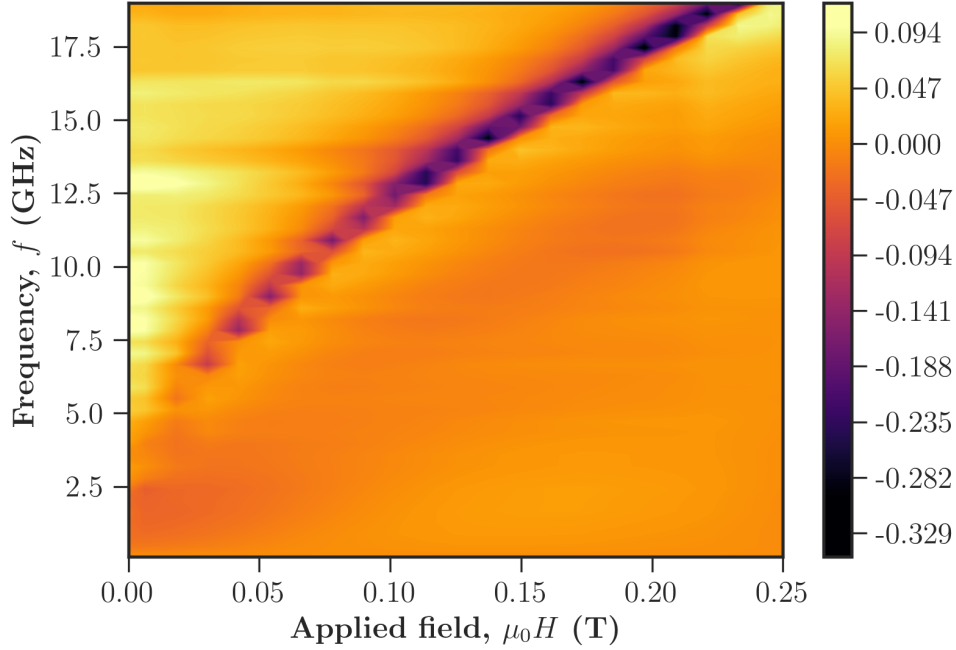


Figure 4.4: Temperature plot of the FMR spectra for the 230 nm thick film with 200⁰C. The square root law of the frequency dispersion shown is typical of films with a dominant in-plane dominant anisotropy component.

4.2.2 Broadband-FMR characterization

In order to analyze the FMR data and extract the uniaxial anisotropy value K_u of the material we used the procedure described in chapter 3. Since the FMR behavior corresponds to a small-amplitude uniform oscillation mode of the film, a uniformly magnetized state without magnetic domains is required for the analysis ($M \approx M_s$). This condition is only reached when full magnetic saturation is achieved, in the range of 10-25 mT. For each frequency, and then a fitting of the real and imaginary part of the uncalibrated permeability $U(f)$ was performed and the resonance field and linewidth is extracted².

For the 230 nm thick film sample annealed at 200⁰C, the fitting of one resonance near $f= 12$ GHz is shown in Fig.4.5 and the corresponding fitting values are shown in Table 4.1. Once a set of resonance peaks measured at different field/frequencies is available (Fig.4.6), their dispersion relation can be fitted using equation 3.22. In this case a good data fit was obtained using a fixed $\gamma/2\pi = 29.145$ GHz/T value corresponding to the bulk iron one[64]. The results of the fit define a uniaxial anisotropy field value

²The full detailed process is described in Chapter 3

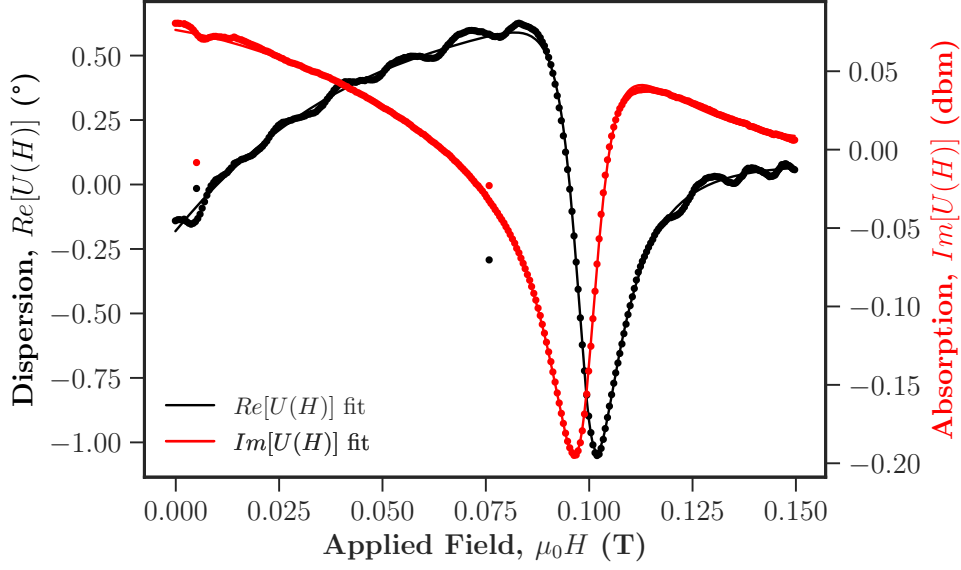


Figure 4.5: Non-linear fit of the resonances for the 230 nm thick film with 200°C. Fixed $\gamma/2\pi = 29.25$ GHz/T and $\mu_0 H_a = 1.582 \pm 0.003$ T

of $\mu_0 H_a = -1.582 \pm 0.003$ T. The discussion of the anisotropy values will be presented in section 4.3.

$U(H)$	A (10^{-3})	$\mu_0 H_{res}$ (mT)	$\mu_0 \Delta H$ (mT)	$\Delta\phi$ (rad)
Re	2.05 ± 0.05	99.5 ± 0.1	6.5 ± 0.1	-5.44 ± 0.2
Im	0.33 ± 0.04	99.54 ± 0.08	6.71 ± 0.08	-5.43 ± 0.01

Table 4.1: Parameters obtained from the peak fit of the 230 nm thick sample at 12 GHz

To obtain the magnetic losses, another fitting procedure is applied on the linewidths of the FMR peaks, using equation 3.23. They give for this sample $\Delta H_0 = 4 \pm 1$ mT and $\alpha = 2.9 \pm 0.2 \times 10^{-3}$ (Fig.4.7)

The procedure is then repeated to all the sample sets, annealed from 200°C to 325°C. The summary of the results can be seen in Table. 4.2

4.2.3 Discussion

Anisotropy of the FeSiB films

A summary of the values of anisotropy fields found for the set of four FeSiB thin film samples with thickness ranging from 80 nm to 300 nm, each annealed at different temperatures is shown in column H_a of Table 4.2. The -1.6 T value is almost constant across

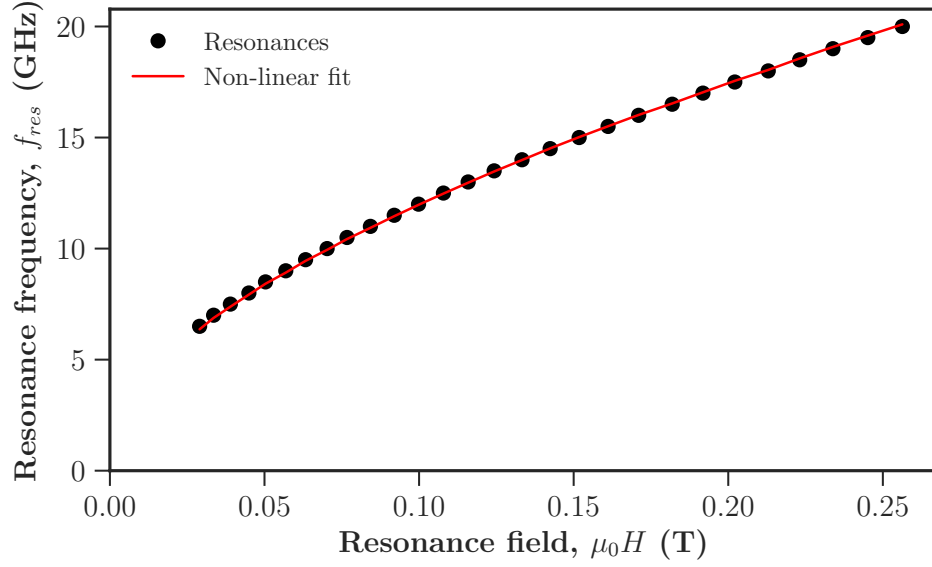


Figure 4.6: Non-linear fit (Eq. 2.53) of the resonances for the 230 nm thick film with 200⁰C. Fixed $\gamma/2\pi = 29.25$ GHz/T and the output $\mu_0 H_a = 1.582 \pm 0.003$ T

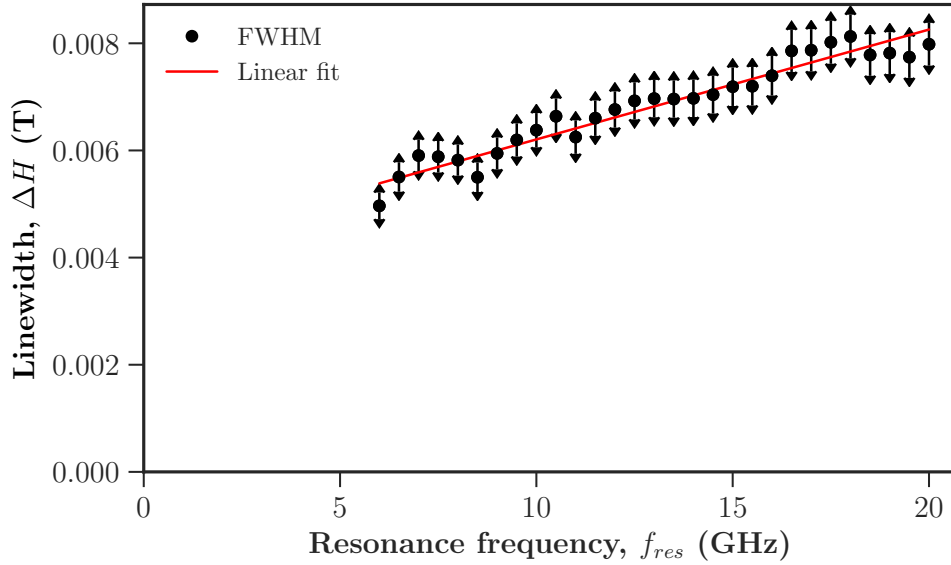


Figure 4.7: Non-linear fit of the linewidths for the 230 nm thick film with 200⁰C. Fixed $\gamma/2\pi = 29.25$ GHz/T, $\mu_0 \Delta H_0 = 4 \pm 1$ mT and $\alpha = 2.9 \pm 0.2 \times 10^{-3}$

the whole set of samples and annealing temperatures, and the small variations should reflect the effect of stress relief by annealing. Negative values of the anisotropy field

		H_a (T)	ΔH_0 (mT)	α (1e-3)
80 nm	200°C	-1.656 ± 0.004	2.8 ± 1.9	2.3 ± 0.2
	225°C	-1.658 ± 0.002	5.6 ± 0.4	2 ± 0.1
	250°C	-1.659 ± 0.002	6.7 ± 0.7	1.8 ± 0.1
	300°C	-1.671 ± 0.002	8.2 ± 0.5	1.9 ± 0.1
	325°C	-1.687 ± 0.002	5.7 ± 0.9	2.2 ± 0.1
150 nm	200°C	-1.638 ± 0.003	0.2 ± 0.1	3.4 ± 0.2
	225°C	-1.646 ± 0.005	0.1 ± 0.2	3.7 ± 0.3
	275°C	-1.678 ± 0.003	0.2 ± 0.2	4.3 ± 0.5
230 nm	200°C	-1.582 ± 0.003	4.0 ± 0.1	2.9 ± 0.1
	225°C	-1.653 ± 0.004	2 ± 0.2	3.8 ± 0.2
	250°C	-1.602 ± 0.003	1.7 ± 0.6	3.2 ± 0.1
	275°C	-1.614 ± 0.002	1.4 ± 0.1	3.5 ± 0.1
	300°C	-1.613 ± 0.004	2.5 ± 0.1	3 ± 0.1
	325°C	-1.597 ± 0.004	2.0 ± 0.2	3.8 ± 0.2
300 nm	200°C	-1.660 ± 0.002	3.3 ± 0.2	2.9 ± 0.3
	225°C	-1.664 ± 0.003	2.9 ± 0.2	3.4 ± 0.3
	250°C	-1.653 ± 0.003	1.5 ± 0.2	3.5 ± 0.2
	275°C	-1.669 ± 0.002	2.7 ± 0.2	3.5 ± 0.2
	300°C	-1.671 ± 0.002	2.5 ± 0.2	2.9 ± 0.2
	325°C	-1.669 ± 0.002	1.6 ± 0.2	2.9 ± 0.4

Table 4.2: Summary of the magnetic anisotropy and damping constants obtained from the Broadband FMR experiments. The uncertainties are an indication of the quality of the fit, and not of the constant value itself. The plots are presented in Figs. 4.8 and 4.9

H_a indicate that the dominant anisotropy component present is IP.

The slight decrease of the negative H_a found in the t=80 nm sample by increasing the annealing temperature, indicates a trend toward a more favorable in-plane magnetization due to the progressive disappearance of the small OOP anisotropy component of magneto-elastic origin. This relaxation effect is present up to 325°C and it was not directly visible in previous data using hysteresis curves in [59, 59, 60, 61]. This result shows that FMR can be a very sensitive technique for anisotropy analysis.

The t=230 nm set of samples also presents a similar behavior although some oscillation of the results is observed and the increase in the negative value of the anisotropy field seems to saturate at 300°C.

As mentioned in Chapter 2, the anisotropy field is defined by $\mu_0 H_a = 2K_u/\mu_0 M_s$, where K_u is the sum of different uniaxial contributions. The samples are expected to be amorphous, with internal stresses due to the deposition process, so $K_u = K_{shape} + K_{m-e}$ where $K_{shape} = -\mu_0 M_s^2/2$ and the values of K_{m-e} are positive as verified by the decrease of K when internal stresses are removed, and also in the hysteresis loops[62, 59]. So the

minima H_a values found for each sample correspond to the their M_s value associated to K_{shape} alone.

a) In the case of the $t=80$ nm sample set, the minimum of H_a was found at 325°C and we can estimate its saturation magnetization being $\mu_0 M_s = 1.687$ T. This value is higher than the FeSiB bulk value of 1.45 T. This result can be associated to the high Fe/Si ratio observed by EDS on the deposited films [59], and should anyhow be noted that similar results with $\mu_0 M_s = 1.52 - 1.68$ T were recently reported for FeSiB amorphous ribbons in the eutectic composition by [52]. The value found for the 80 nm thick film samples is representative for the whole sample thickness and annealing set, as it can be seen in Fig. 4.8

b) the 150 nm sample set also presents decreasing anisotropy field values with increasing annealing temperature, although only a few results are present since a reduced number of annealed samples was available.

c) In the case of the set of $t= 230$ nm film samples, the analysis of the anisotropy and saturation magnetization is not immediate. The expected decreasing trend of the anisotropy value observed in the previous film sets is not strictly followed by the films annealed at 225°C and 325° . The most likely cause of the fluctuation of the observed values is connected to the uncertainty on the anisotropy field H_a values, which is higher than the uncertainty reported by the fitting procedure alone.

A few important notes are required to understand which measurement uncertainties are intrinsic in our instrumental setup. The gap between the electromagnet poles is larger than the pole radius, so the field homogeneity region is rather small. To circumvent this problem, the sample was positioned in the center of the gap on the axis of the poles. The gaussmeter probe was positioned as close as possible to the sample (on top). During each sample change the probe was removed and replaced as close as possible to its original position. A slight change in position (or rotation) of the probe, combined with the field inhomogeneity could easily cause an offset of a few mT in the field readings from sample to sample. If one considers a generic 2% error on the resonance field (ΔH_{res}), equivalent to 1.6 mT at 11 GHz, as it will be described in the following error propagation section, would lead to $\Delta H_a = 35\text{mT}$, which is a rather large value if compared to the m-e anisotropy contribution.

The summary of $\mu_0 H_a$ of all the characterized samples with $\Delta H_{res} = 2\%$, is shown on Fig.4.8. The decreasing trend due to the relaxations are still visible, but the errors do not allow to trace a more detailed quantitative analysis. Nonetheless, If one takes the difference between the films at 200°C and 300°C for 230 nm thickness, the out-of-plane anisotropy field contribution is of 35 mT and $K_{m-e} = 23$ kJ/m³. Considering the higher M_s value found of 1.65 mT, the anisotropy values found here K_{m-e} are in line with those derived from the hysteresis loop data in [59].

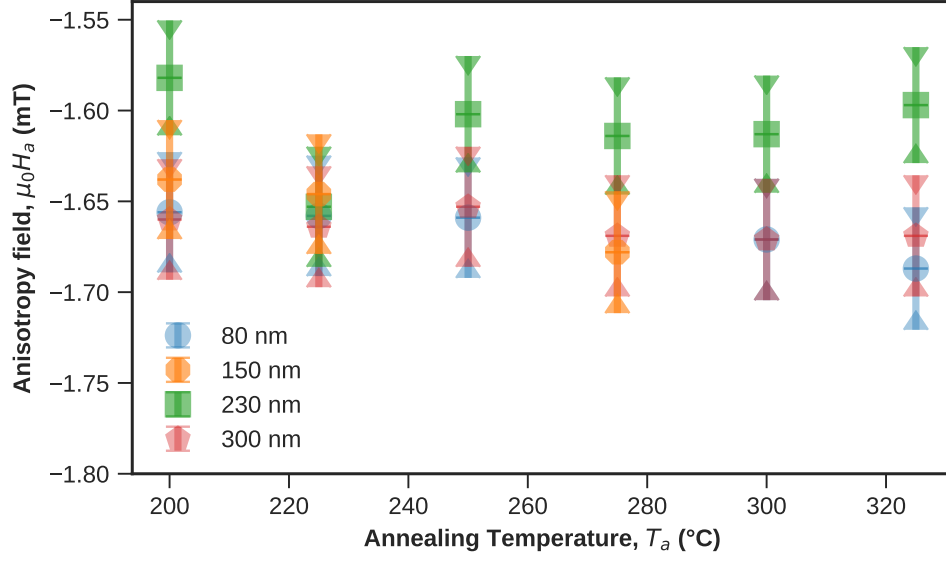


Figure 4.8: Summary of the obtained anisotropy field values for all the samples. The error was propagated for $\Delta H_{res} = 2\%$.

FMR Linewidths and magnetic damping

An example of the fitting of the linewidths by Eq. 3.23 is shown in Figure 4.7. The summary of the α and ΔH_0 parameters obtained by the fitting procedure for all the samples can be seen in Table 4.2. Since both the linewidth and the damping are independent of the exact value of applied magnetic field their uncertainty should not be affected by the probe positioning issue mentioned on the last section.

The main source of uncertainty for the linewidths are the field fluctuations at each new field step. In order to keep the error to a minimum, small applied field steps of 0.5 mT and a delay of 3 s were used before each frequency sweep measurement. Thus, we chose to keep the fit affidability values, as seen in Table 4.2.

The α Gilbert damping value has to be corrected for the capacitive coupling between the sample and the CPW as described in [64] (radiative damping):

$$\alpha_{rad} = \frac{\gamma M_s \mu_0^2 t l}{16 Z_0 w_{cc} c} \quad (4.1)$$

where l is the sample length on the waveguide (10 mm), t is the sample thickness, Z_0 the characteristic coplanar waveguide impedance (50 Ω), w_{cc} the CPW central conductor width (1 mm). The correction determines a reduction of the damping, in the range of $4 \times 10^{-4} \sim 1.4 \times 10^{-3}$ for $t = 80 \sim 300$ nm.

On all of the samples, the radiative damping corrections leads to α damping values in the range of $1.5 \sim 2.7 \times 10^{-3}$. No well defined trend was observed with the annealing

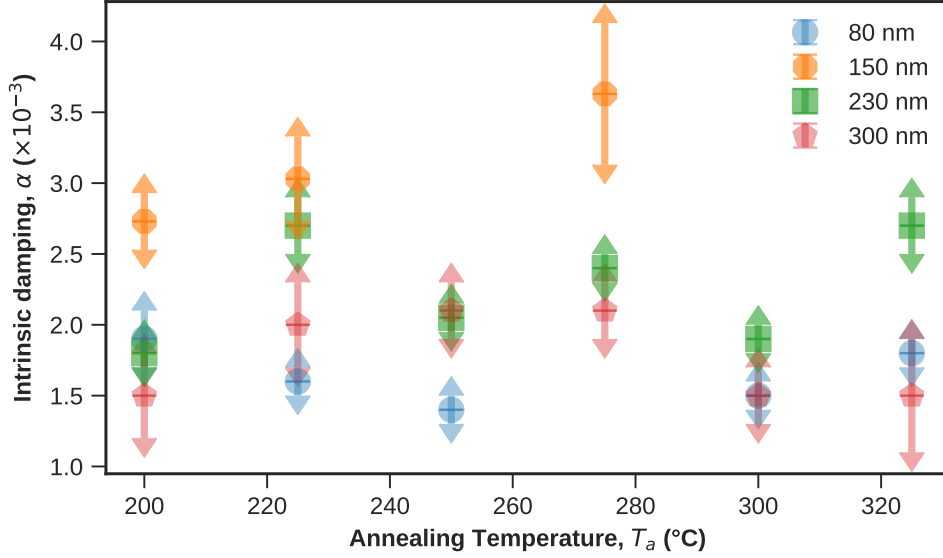


Figure 4.9: Summary of the obtained intrinsic damping values found for all the samples. They were corrected for the capacitive coupling between the sample and the CPW

temperature. It is interesting that the values on these samples are similar to values typically found in literature for bcc Fe 20 nm thin films with damping $\alpha = 1.9 - 2.7 \times 10^{-3}$ [64, 65, 66]. However, the amorphous films in this analyzed in this thesis are 4 to 10 times thicker. The low damping found here, despite of the large thickness is connected to the higher resistivity and the lack of a long range crystalline structure, which reduces the efficiency of the spin precession dissipation into phonons. The effect of surface irregularities and pinning centers is also reduced due to the higher sample thickness.

We conclude that both the annealing temperature and sample thickness (on the range of 80-300nm) may be used to modify the anisotropy, keeping the damping properties constant. The low damping of $\approx 2 \times 10^{-3}$ found in combination with the high $\mu_0 M_s = 1.65$ T at higher thickness (230 nm) makes them a viable candidate to substitute CoFeB for spin-wave propagation investigations.

4.2.4 Error Propagation

In the paper by Coisson et al. [59] the range of values obtained for the m-e anisotropy energy density is $K_{m-e} = 13 - 23$ kJ/m³ in FeSiB samples with thicknesses between 150 and 300 nm. Converting these energy densities to field values, we obtain a range between $H_a = 22.5 - 39.9$ mT³. Hence, the uncertainty in the anisotropy field ΔH_a

³The conversion is done using $\mu_0 H_a = 2K_u/M_s$

needs to be in the order of a few mT to a proper quantitative analysis of the stress release by thermal annealing.

Ignoring possible correlations between the variables, the propagated error $\Delta f(x, y)$ of a function $f(x, y)$ is given by:

$$\Delta f(x, y) = \sqrt{\left(\frac{\partial f(x, y)}{\partial x}\right)^2 \Delta x^2 + \left(\frac{\partial f(x, y)}{\partial y}\right)^2 \Delta y^2}, \quad (4.2)$$

where Δx and Δy are the respective variable errors. Rewriting equation 2.20 to be in the form $H_a(f_{res}, H_{res}, \gamma)$:

$$H_a(f_{res}, H_{res}, \gamma) = H_{res} - \frac{1}{H_{res}} \frac{f_{res}^2}{\gamma^2}. \quad (4.3)$$

Since γ was fixed, the uncertainty is then given by:

$$\Delta H_a = \sqrt{\left(1 - \frac{1}{H_{res}} \frac{f_{res}^2}{\gamma^2}\right)^2 \Delta H_{res}^2 + \left(\frac{2}{H_{res}} \frac{f_{res}}{\gamma^2}\right)^2 \Delta f_{res}^2}. \quad (4.4)$$

One needs then to evaluate the uncertainties ΔH_{res} and Δf_{res} to compute ΔH_a . The fittings of resonance field H_{res} are obtained with a negligible error, but ΔH_{res} can be estimated from the difference between the values obtained from the fitting of the $\text{Re}[U(H)]$ and $\text{Im}[U(H)]$ spectra. They are on average $\sim 0.2\%$, which is associated to an uncertainty of $\Delta H_{res} \sim 10^{-4}$ mT. The uncertainty on the frequency Δf_{res} depends on the VNA internal filter, which was set to 1 KHz giving an uncertainty smaller than 10^{-6} for frequencies above 1 GHz, thus Δf_{res} can be neglected.

In Fig.4.10a) it can be seen the uncertainty ΔH_a plotted for dataset of the sample with $t = 230\text{nm}$ and 225°C as a function of the resonance frequency F_{res} . Below 8 GHz, there is a divergence, most likely by the absence of full magnetic saturation, invalidating the uniaxial anisotropy equation.

In order to verify the effect of ΔH_{res} in ΔH_a , they are plotted in Fig.4.10b). It can be see that ΔH_a grows almost linearly with ΔH_{res} , apart from the divergences already mentioned.

The average ΔH_a can be kept below 5 mT as long as the sample is fully saturated and ΔH_{res} is below 0.6 mT. This results confirms that the procedure can be employed to investigate the m-e energy and the source of uncertainty in the anisotropy field is due to the field inhomogeneities mentioned on Sec 4.2.3. Thus, we have enough sensitivity, but not enough accuracy to properly quantify the release of the stresses.

4.3 Micromagnetic Simulations

The multiple FMR peak structures observed in the field sweep of the FeSiB films presented in Fig. 4.3 may be connected to the presence of stripe domains. The stripe domains state, as opposed to the saturated state, allows for the presence of a multiplicity

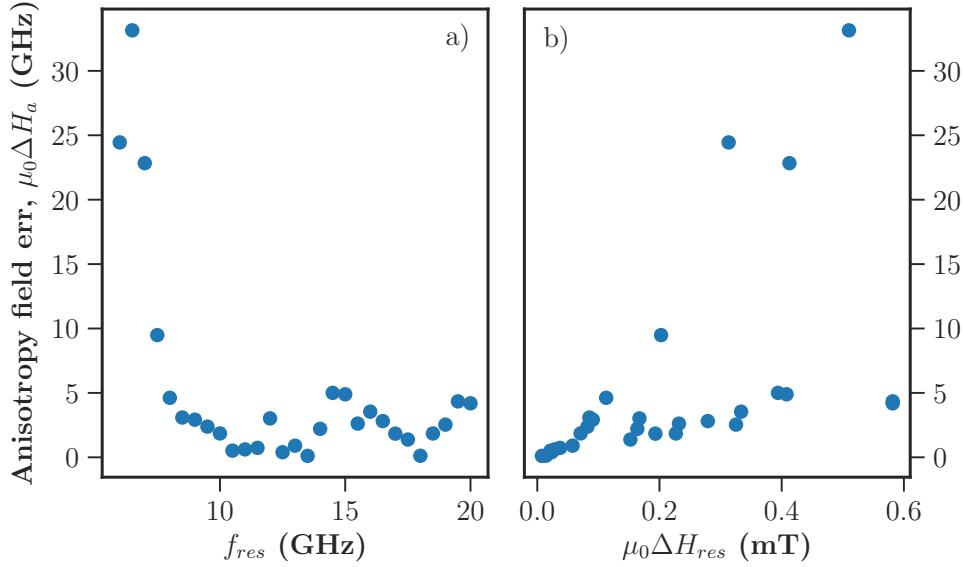


Figure 4.10: Propagated uncertainty in the anisotropy field $\mu \Delta H_a$ as a function of a) the resonance frequency f_{res} and b) the uncertainty of the resonance field $\mu_0 \Delta H_{res}$

of resonance conditions. This system can be solved analytically using a system of coupled Smit-Beljers equations (Eq. 2.47) for each different magnetic region (domains and domain walls). However, these calculations are quite complex and many assumptions and simplifications have to be made in order to find a solution.

The alternative approach to the study of this complex magnetic system with stripe domains is to use micromagnetic simulations. In these simulations, the sample is subdivided in small volumes, each representing a group of strongly phase-coupled spins, and for each of those cells, the effective field is calculated using the gradient of the magnetic energy (see section 2.3) defined by the user. The Landau Lifshitz Gilbert equation is then solved numerically for each of the volumes, obtaining in the end a detailed 3d map, in time, of the dynamics of the magnetization in a sample with a complex domain structure.

The micromagnetic program chosen for this task was the MuMax3 [67] package, which uses the finite differences method optimized for parallel computing graphics cards (GPU). The use of graphic cards allow for the simultaneous solution of all the cells (volumes), decreasing by several orders of magnitude the time required for the simulation (of the order of 10^6). The software also calculates the demagnetizing field using a GPU optimized fast fourier transform package.

4.3.1 Mumax3 simulation parameters

In order to guarantee that the results of the simulation have physical meaning, the first consideration is on the cell size. If only dipolar and exchange interactions are present, the cell size has to be similar to the correlation length. This is the maximum distance at which neighboring spins have such a strong attraction to behave as one. The correlation length can be defined as [9] :

$$l_{ex} = \sqrt{\frac{2A}{\mu_0 M_s^2}} \quad (4.5)$$

where A is the exchange interaction constant and M_s the saturation magnetization. For the FeSiB, if we use the standard value for $A = 4 \times 10^{-12}$ J/m and the value equivalent to⁴ $\mu_0 M_s = 1.65$ T from the previous chapter as well as from [60], we obtain $L_{ex} \sim 2$ nm, so we fix the cell size at the same value.

The second consideration is the total size of the sample. The chose shape must large and flat enough to guarantee that we are in the thin film geometry approximation for the demagnetizing field ($n_c \sim 1$), but we cannot simulate the whole sample 1 cm^2 , since it would require 10^{14} cells. To overcome this limitation we can use a smaller $0.25 \text{ } \mu\text{m}^2$ sample, in which only a few stripe domains can be formed, and repeat the pattern to calculate the demagnetizing field using periodic boundary conditions (PBC). For an oblate ellipsoid, the demagnetizing field as a function of the PBC is given in⁵ :

$$n_c = \frac{m^2}{m^2 - 1} \left[1 - \frac{1}{\sqrt{(m^2 - 1)}} \arcsin\left(\frac{\sqrt{(m^2 - 1)}}{m}\right) \right] \quad (4.6)$$

where m is the ratio between thickness and length. On Fig.4.11, one can see that the use of 250 PBC is sufficient in most cases. Finally the simulation size used was of $250 \times 250 \times 75$ cells (x,y,z), and the surface of the sample seen by the demagnetizing field after applying the PBC is of 0.156 mm^2 .

The third consideration is the magnetic constants to be used. We used $A = 4 \times 10^{-12}$ J/m and $\mu_0 M_s = 1.85$ T as mentioned before. The Gilbert damping constant $\alpha = 5 \times 10^{-3}$ was taken in consideration due to the fact that the simulation is in a perfectly homogeneous sample. We also introduced an uniaxial OOP anisotropy $K = 23 \text{ kJ/m}^3$ as reported in [59], to account for the magneto-elastic contribution.

⁴The actual value used was 1.85 T. Since the gyromagnetic ratio is kept at the free electron value in Mumax by default, the M_s has to be rescaled.

⁵This is a more detailed solution of the integral described in section 2.3.1. For a more detailed description, please refer to [8, 9, 68]

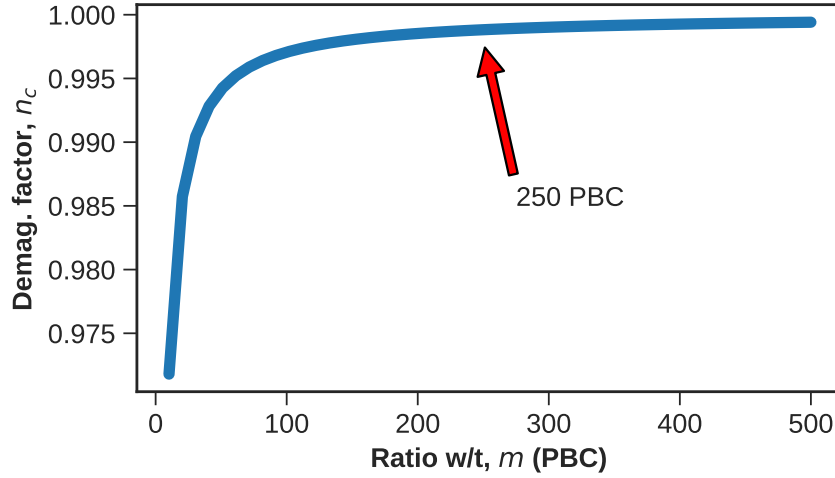


Figure 4.11: Change in the demagnetizing factor as a function of the ratio of width to thickness. $n_c = 1$ in the ideal oblate ellipsoid. 250 PBC gives around $n_c = 0.999$.

4.3.2 Simulation Procedures

Two sets of simulations were performed in this thesis. One set was used to reproduce the $M(H)$ curves from [59] and evaluate the validity of our model. The other set of simulations was performed to reproduce the frequency dispersion results from the Broadband-FMR experiments, and further investigate which physical conditions give rise to the experimentally observed absorption modes when the stripe domains are present.

In the first set of simulations, related to the $M(H)$ curves, each point corresponds to a simulation. As a first step a field value (e.g. $H = 0$) is applied, the system is initialized with out-of-plane (OOP) stripe domains alternating in the up and down direction, in absence of any closure domains. The system is then allowed to relax to a local energy minimum⁶ at zero field with a random thermal noise at $T = 300$ K. In the next field step ($H = 0 + \Delta H$), one starts with the system in the previously relaxed state, and the system is allowed to relax reaching a new equilibrium state in the presence of the newly applied field and the thermal noise. In the next steps the procedure is repeated until the hysteresis loop is completed.

In the second set of simulations, related to finding the high frequency oscillation modes of the system, a similar procedure is applied: at first we start with a stripe domain configuration and a magnetic field is applied, which has the DC field directed along longitudinal to the stripes, and a $\text{Sin}(t)/t$ pulse directed along \hat{x} . The sin cardinal

⁶The function relax from MuMax3 searches for a local minima, and has dynamic time steps to optimize the computational cost.

function has a square shape in the frequency domain, and it excites simultaneously and with the same intensity the whole chosen frequency range set to 20 GHz. The system is then let to run for a few nanoseconds, at fixed time steps. The amplitude of the sin cardinal field pulse was set to $H_{ac} = 0.5mT$, to guarantee the $M \approx M_s$ approximation to be kept. After the simulation, an FFT (fast fourier transform) of the time domain results (i.e. $m_x(t), m_y(t), m_z(t)$ etc.) obtained at each imposed DC field value is performed to obtain the frequency spectra where the microwave modes are found.

To reduce the computation time, the film thickness chosen for the simulation was the $t=150$ nm, which also presents the same transcritical $M(H)$ curves and stripe domains as the $t=230$ nm one [59]. Even with this reduced sample thickness, each simulation required 50-100 hours, generating datasets from about 100 MB to 10 GB. It is also very important to reduce the data to a minimum, to allow for proper post-processing of the simulated data.

4.3.3 Results and Discussion

In Fig.4.12a) we show a 3d representation with the magnetic domains and domain walls present at the remanence state with zero applied field, which corresponds to the stripe domains structure also observed by MFM imaging by Coisson et al in [61].

The simulated hysteresis loop qualitatively reproduce the experimental transcritical ones of [59] (Fig. 4.12b). The remanence and saturation field are closely matched, although the coercivity is not. This may be due to the high number of pinning points and defects in the real sample, or other anisotropy contributions which remains to be investigated. Nevertheless, the results are satisfactory as a first model.

It is interesting to note that the magnetization of the domains points out of the plane only in its core, and smoothly becomes in-plane at the surface. Closure domains can also be seen on the surface between the stripes. When the applied field increased, the stripe domains start to tilt from the OOP direction to the field direction, progressively enlarging the more favorably oriented domains, merging near saturation.

Once the simulation parameters were able to reproduce the static magnetization behavior of the film, we proceeded to simulate the dynamic behavior. The simulation set is summarized in Fig.4.13. Several modes can be seen in the stripe domain regime. Looking closer at a fixed field 10 mT slice in Fig.4.14, one can see actually two well defined modes, followed by a series of smaller ones. Here it is also plotted the experimental frequency sweep of the 150 nm sample annealed at 200⁰ C, and the best match with frequency of the modes is found at 3 mT. This indicates that the anisotropy value used in the simulation is likely higher than the experimental value.

In order to investigate the multiple the frequency modes in more detail, and to define the corresponding spatial configurations in the film volume, simulations were also performed with a fixed frequency. The frequencies were chosen corresponding to the maxima of the main absorption modes of Fig.4.14 at $f_1 = 2.34$ GHz and $f_2 = 4.15$ GHz.

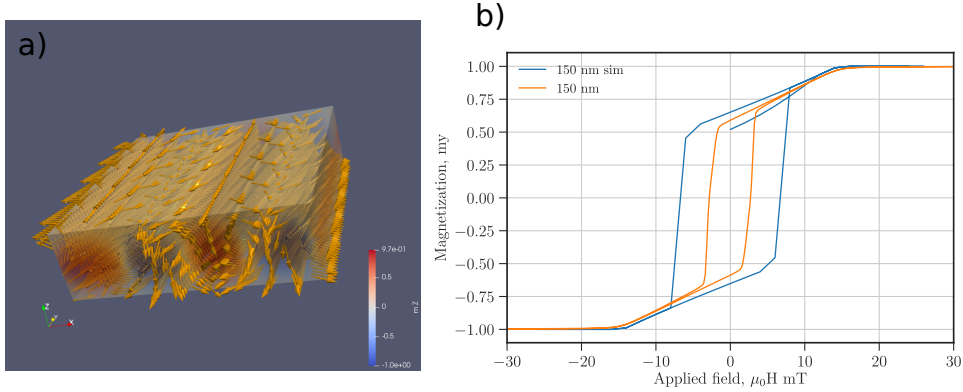


Figure 4.12: a) Cross section of the 150 nm thick film with the domain structure simulated at remanence. The yellow arrows indicate the magnetization direction. The stripe domains have a magnetization that points in the out-of-plane direction only in the center of the domain (red and blue areas) and then becomes parallel to the film surface. b) Hysteresis curves. Orange is the experimental data, and blue the simulated one. Both have a transcritical shape, with the remanence and saturation field closely matched.

A phase sequence was built at $\Delta t = \pi/6T$ (one quarter of a period) steps and the magnetization in the sample zx cross section can be seen in Fig.4.15a) for $f_1 = 2.34$ GHz and Fig.4.15b) for $f_2 = 4.15$ GHz.

In both figures, the stripe domains can be seen at the center circles, surrounded by the closure domains. At f_1 (Fig.4.15a)), the neighboring stripe domains pulses out of phase, and show a change in amplitude concentrated in the y direction (perpendicular to the cross section of the sample and longitudinal to the stripes direction). This indicates that the oscillation is mostly happening in the yz plane. The closure domains follow the same pattern, but in a much smaller amplitude.

At f_2 (Fig.4.15b)) it can be seen a much higher oscillation amplitude, and some circular movements on the stripe domains and longitudinal for the closure domains. Thus, the oscillations now are tilted from the yz plane, with x components. Qualitatively it indicates to be oscillating around the equilibrium magnetization direction, which tilts the OOP components of the stripe domains in the applied field direction (y).

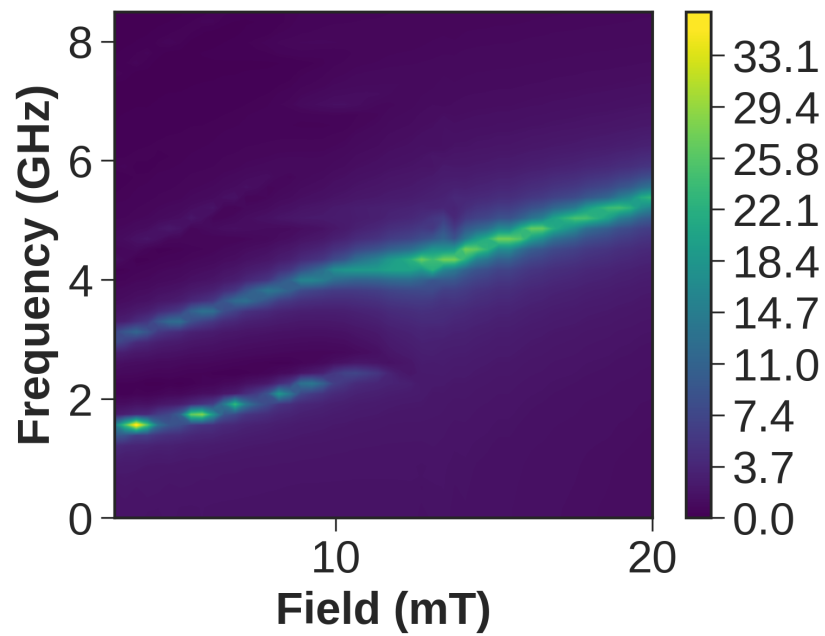


Figure 4.13: Temperature plot of the dynamics simulation of the $t=150$ nm film with applied field up to 20 mT. Multiple FMR modes are observed at low applied field.

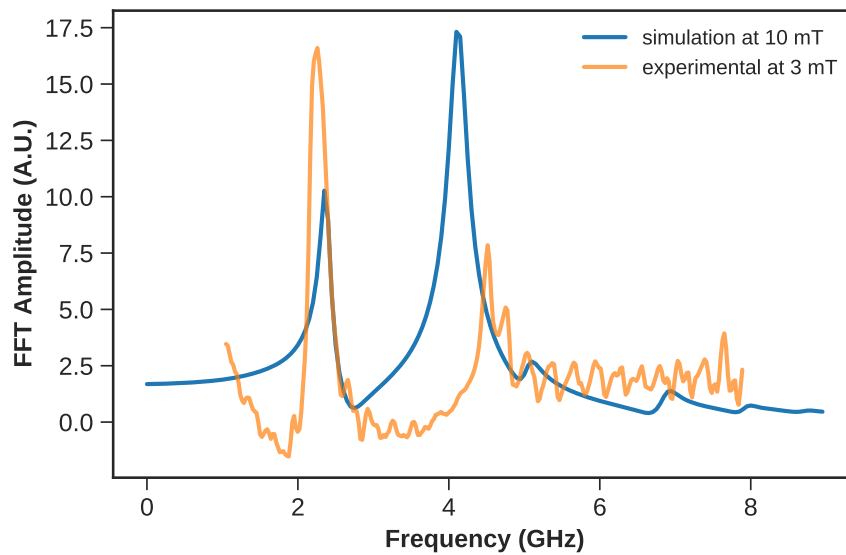


Figure 4.14: Slice of frequency modes at 10mT (simulation) and 3 mT (experimental).

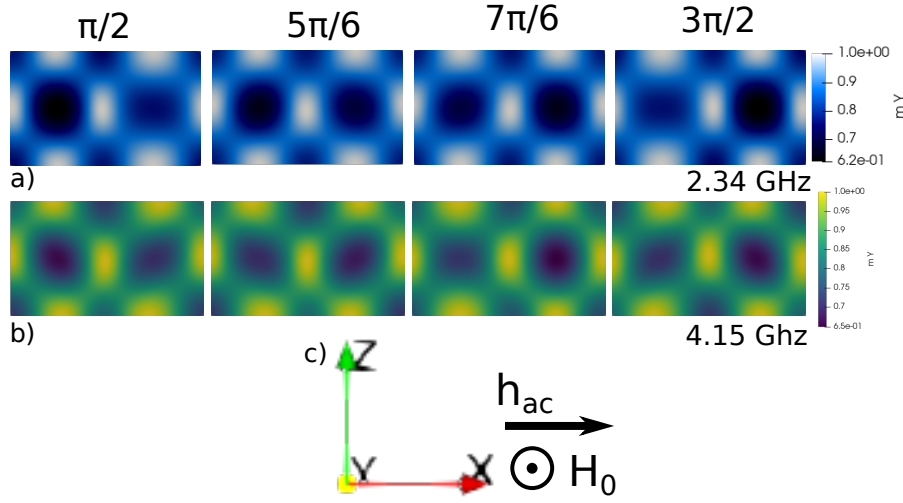


Figure 4.15: Cross section of the temporal progression of a half a period for a) 2.34 GHz and b) 4.15 GHz. c) Vector directions for reference.

4.4 Conclusion and future perspectives

In this work, a framework was developed to investigate the dynamics of FeSiB amorphous thin films exhibiting stripe domains, combining micromagnetic simulations and experimental results.

It was shown that the amorphous FeSiB thin films present a high saturation of magnetization and magneto-elastic energy due to quenched in stresses.

The magnetic anisotropy was investigated by Ferromagnetic resonance experiments, finding results consistent with previously published static magnetic characterization. More work maybe needed for a more precise quantitative analysis of the release of thermal stresses. The low magnetic damping found is very interesting for a potential application of these alloys. Thus, for in-plane anisotropy applications, it was shown that the FeSiB family of alloys can be a viable and more economical substitute to CoFeB thin films.

The micromagnetic simulations were able to reproduce qualitatively the experimental results. The two major oscillation modes were identified and discussed, and it was shown that the smaller mode corresponds to mostly oscillations of the core of the stripe domains.

The developed methods can be used to investigate more complex dynamics in stripe domain systems with the support of micromagnetic simulations. Since these films present a large thickness above 100 nm, a high saturation magnetization and low damping are attractive for the development of magnonic devices, where spin waves can be propagated within the magnetic domain structure.

Chapter 5

Field Free switching spintronic devices

5.1 Introduction

This chapter presents a pure theoretical and numerical simulation work developed in this thesis. The work was carried out in parallel with the experimental activities of the previous chapters. In this chapter we present the activities performed to analyze and compare two classes of materials here used to generate a spin current used to switch a ferromagnetic layer without the need for an external magnetic field.

This investigation resulted in a publication on the Journal of Magnetism and Magnetic Materials [69]. This chapter is an extended version of the published article. It starts with an introduction of the need for new technologies for magnetic storage devices, and then an analysis is presented of field-free magnetic switching of memory nanoelements by spin-orbit torque and the limitations associated to this approach. We then present our comparison of two possible approaches to the switching of memory nanoelements without an external magnetic field, based on both an analytical and a numerical analysis of the dynamics of this process. The merits and issues associated to each process will be discussed.

5.1.1 Magnetic recording devices

Magnetic recording devices have always been of paramount importance to society, as they supplied and still supply the demand for higher and higher data storage capacity. Until recently, the data was stored with magnetic domains, written by a localized applied field and read by induction. One can choose materials with adequate magnetic properties to make smaller and smaller bits, to increase the amount of data that can be stored in a device.

The thermal stability of each memory element depends on the ratio between the anisotropy energy barrier and the thermal energy $EV/k_B T$. To obtain a high memory

density device, the volume of the magnetic "bit" is decreased, but it has a minimum threshold due to the thermal agitation $k_b T$. Also, the smaller the device the smaller the readout signal, which depends on the magnetic induction caused by the transition between the magnetic domains, and proportional to the saturation magnetization the associated volume. Increasing the anisotropy energy allows the use of smaller volume devices, but makes the writing of a magnetic "bit" harder, and requires a higher and more localized field. On the other hand, increasing the magnetization may increase the demagnetizing field, which in turn may increase or decrease the energy stability barrier height. This is the well known magnetic recording trilemma [70]: conflicting requirements between the thermal stability, readability and writeability.

Several scientific breakthroughs in the past two decades have allowed to improve dramatically the data density and speed of magnetic storage devices. First, Co based granular out-of-plane anisotropy thin films with superior energy barriers [70] than its in-plane counterparts. The decrease in readability is solved by the discovery of the giant magnetoresistance [21, 22], improving drastically the readout component. However, the writing component still is done by an applied field. The newest hard drives uses thermally assisted switching, in which the bit volume is locally heated by a laser, decreasing the necessary field. A more exciting development is the recent findings in spintronics [71], that allowed magnetization switching by an electric current, in absence of an external magnetic field.

5.1.2 Spin orbit torques devices

Novel magnetic phenomena like spin transfer torque (STT) have also been successfully used to produce memory devices such as the non-volatile magnetic random access memory (MRAM)[72, 73].

Spin orbit torques [74, 75, 76, 77, 15] (SOTs) are an effective way to switch the magnetization of perpendicularly magnetized thin nanoelements by means of electric currents. Imposing an electric current on a heavy metal layer (HM), a spin current is generated by the spin Hall effect and its moments can be transferred to an adjacent ferromagnetic (FM) layer, causing a torque on its magnetization. The strength of the torque depends on the transferred spin current density, which is directly proportional to the spin hall angle θ_{SH} :

$$\theta_{SH} = \frac{2e \sigma_{sh}}{\hbar \sigma_0} \quad (5.1)$$

where e is the electron charge, \hbar the Planck constant, σ_0 the electric conductivity and σ_{sh} the spin hall conductivity. The spin hall angle is thus a direct measure of the efficiency of the conversion from the charge current to the actual torque exerted on the FM. Typical values range from 0.032 for Al, up to 33 in some heavy metals as Ta and Pt [78].

Alternatively, the electric current also generates an accumulation of polarized spin density at the interface between the HM and FM, causing a torque on the adjacent FM

layer by the exchange interaction[78]. This effect is known as the inverse spin galvanic effect. In both previous cases, the spin current produces the damping-like and field like torque as in STTs (see section 2.6). These phenomena are of great interest for data storage devices, where they can potentially substitute the present writing systems - especially for racetrack memories and magnetic logic devices.

In such applications, there are size scalability advantages by using perpendicular anisotropy materials (PMA). To invert the magnetization of the bit of hypothetical memory, the current induced torque needs to overcome the energy barrier. For PMAs, the shape anisotropy contribution was already compensated by the out-of-plane anisotropy, and thus the current needed is directly proportional to the anisotropy. More so, in the in-plane device the current needs also to best the shape anisotropy, which raises the current and does not contribute to the thermal stability[79].

However, to achieve deterministic magnetic switching in PMAs, one needs to perturb the energy landscape[79] of the system. The simplest way to perturb the energy and obtain SOT switching uses an external bias field. Unfortunately, although deterministic switching has been successfully attained in [74, 80, 75, 81, 82, 83], applying an external in-plane (IP) field undermines the technological advantages of utilizing SOT for practical purposes.

In the context of practical use for SOT-MRAM three terminal devices [79, 84, 85, 86, 15], where the magnetic-tunnel junction readout block is ferromagnetically uncoupled, a minimum stacking of layers is desired. A first solution compatible with SOT switching is to generate an IP bias field adding an extra magnetic layer: either an uncoupled FM layer on the stack or an HM antiferromagnet layer such as PtMn[87, 88] or IrMn[89], two materials which can simultaneously provide the spin current and the necessary bias field. A second solution to obtain SOT switching, is to modify the energy landscape by breaking the spatial symmetry of the PMA energy barrier, which introduces an angular tilt in the out-of-plane (OOP) anisotropy axis. Torrejon et al.[90] and You et al.[91] engineered the anisotropy tilt using film-thickness gradients on either the FM or the MgO oxide layer, and obtained a field-free deterministic switching on HM/FM/MgO trilayers.

It is worth mentioning that other field free switching methods have been recently proposed to achieve the system symmetry-breaking. Some of them are: extra in-plane shape anisotropy due to a elongated FM shape [92] and extra input current terminal on the \mathbf{x} direction [93, 92, 94]; extra field-like torque caused by a thickness gradient of the oxide layer [95, 96]; RKKY coupling with a second FM layer [97, 98]; laterally attached in-plane anisotropy FM structures [99], switching by induction of domain nucleation [100] ; the creation of a T type structure[101]; composite free-layer composed by antiferromagnetically coupled layers [102] and Co/Pt/Co trilayers with orthogonal easy axis between Co layers[103]. Nonetheless, these methods cannot be implemented easily or without the introduction of additional layers in the three-terminal architecture device. As a matter of technological applicability, the in-plane bias field or anisotropy tilt methods remain of great interest and potential.

Until now, it is still unclear if an in-plane bias field or an anisotropy tilt would only help the SOT switching or would also interfere with the energy barrier height and critical current values: in the scenario of a reduction of the energy barrier, the possible miniaturization of the devices would be jeopardized, because the memory elements would become thermally unstable. Since the relationship between the energy barrier and the critical current is extremely important for SOT based data storage applications, it needs to be investigated thoroughly.

To this end, in this chapter we focus on the writing performance of both methods described above to achieve field-free SOT magnetization switching. Namely a fixed bias field such as the AFM/FM bilayers (bias case) and an anisotropy tilt caused by a structural asymmetry (tilt case). The writing performance is analyzed with respect to two requirements of magnetic recording: a large energy barrier for thermal stability and a small critical current for power efficient switching. As such, the results may be useful independently of the chosen reading method for specific three-terminal applications.

The investigation was done first by analyzing analytically the effects of a bias field induced by an AFM/FM layer or an anisotropy tilt using an HM/FM system on the free magnetic energy landscape. We then proceed to solve numerically the Landau-Lifshitz-Gilbert equation on a macrospin approximation either at several different in-plane field values or with different anisotropy tilt angles, interpreting the results in the light of the effective bilayer energy landscape. Finally, we investigate the effect of the current pulse duration, equivalent to the speed of operation of an hypothetical SOT switching device.

5.2 Energy barrier modeling

The discussion begins by presenting a simple model for the magnetic energy of the two mechanisms (see Fig.5.1(a) and (b)). The energy density of a perpendicular anisotropy system is $F = E/V = -K_u m_z^2$ where K_u is the effective uniaxial anisotropy constant, m_z is the third component of the normalized magnetization \vec{m} and V is the volume of the ferromagnetic layer. Here, the anisotropy constant is the resultant of the out-of-plane anisotropy K_{oop} and the shape anisotropy $K_u = K_{oop} - \mu_0 M_s^2/2$, where μ_0 the vacuum permeability and M_s the saturation magnetization. The two systems in consideration have out-of-plane anisotropy and, thus, K_u is strictly positive. The energy landscape is symmetric as it is shown in Fig.5.1(c). The saddle points corresponds to the equator and the minima to the poles of the sphere.

For the bias case, a ferromagnet in contact with an antiferromagnet as depicted in Fig.5.1(a). In a simple approximation we can model it with a unidirectional field, representing the strength of the exchange field bias. The energy density of the system becomes:

$$F = -K_u m_z^2 - \mu_0 M_s m_x H_X, \quad (5.2)$$

where H_X is the exchange bias field. The energy landscape corresponding to such energy density is shown in Fig.5.1(d).

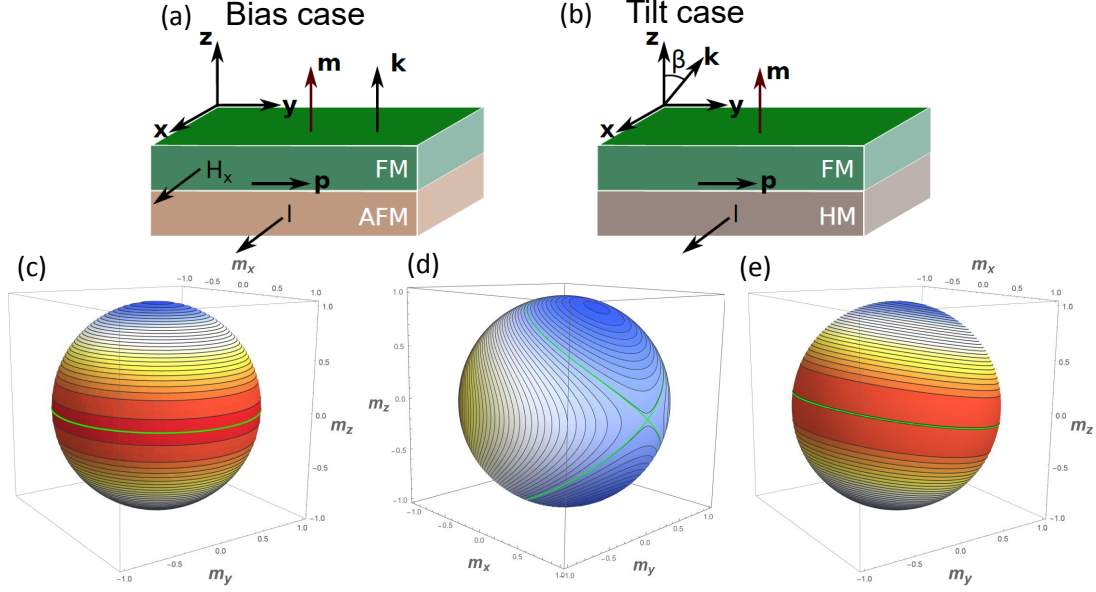


Figure 5.1: (a) Vector diagram of the bias case and (b) tilt case. The anisotropy tilt angle is in the yz plane for the tilt case. Energy landscape for (c) Perpendicular anisotropy, (d) Bias case and (e) Tilt case. In the graphs, the blue color is the minimum value and red is the maximum value. The magnetization may switch if the applied current is sufficient to traverse the separatrix line plotted in green. Energy-conserving trajectories are shown in black.

In the other mechanism, which we label as the tilt anisotropy case, the energy is modeled by adding a tilt angle on the anisotropy axis (see diagram in Fig.5.1(b)). Under this assumption the energy density becomes:

$$F = -K_u(\vec{m} \cdot \vec{k})^2, \quad (5.3)$$

where \vec{k} is the anisotropy axis and has the form $\vec{k} = (0, \sin\beta, \cos\beta)$ where β is the tilt angle. We plot the landscape of such case in Fig.5.1(e) (right).

For now, it can be noted that the energy landscapes of the tilt and standards are similar, albeit for a rotation caused by the tilt. On the other hand, the bias case presents not only a rotation, but also several new high energy zones, with its saddle points not being directly over the equator.

5.2.1 Equilibrium positions

To obtain the equilibrium positions, one needs to find the minima on equations 5.2 and 5.3. This is done by obtaining the first derivative and setting the value to zero, and checking the signal of the second derivative to determine if it is a maxima ou minima.

For the tilt case, the results are straightforward and the equilibrium positions follow the tilt angle on the z axis projection. The equilibrium state is aligned to the anisotropy axis and then $\vec{m}_{eq} = (0, \pm \sin\beta, \pm \cos\beta)$.

In the bias case, it is considered a bias field H_X smaller than the anisotropy field $H_k = 2K_u/\mu_0 M_s$, as to not cause a field dependent switching of the magnetization. The system then has two equilibrium positions with positive and negative projection on the z axis (top and bottom). Their values in polar coordinates are:

$$\theta_{eq} = \arcsin\left(\frac{H_X}{H_k}\right). \quad (5.4)$$

These equilibrium positions correspond to the linear part of the hard axis IP hysteresis loop with perpendicular anisotropy, with $m_x = H_X/H_k$. There are two valleys corresponding to such minima as shown Fig.5.1(d). There is also a high energy region, which contains the global energy maximum. This region corresponds to the white and yellowish regions of Fig.5.1(d). Both the minima valleys and the high energy regions are partitioned by the separatrix (green line) as can be seen in Fig.5.1(d). In the anisotropy tilt case the separatrix is rotated by the tilt angle and there are no other equilibrium regions apart from the two minima (see Fig.5.1(e)). The existence of the high energy region in the bias case will change the behavior of that system. In the anisotropy tilt case, once the current is switched off the magnetization will evolve to the minimum corresponding to the nearest valley and will relax to the corresponding energy minimum. In the bias case, if at the end of the current pulse the magnetization is in a minimum valley, the magnetization will spontaneously evolve to the corresponding minimum, due to energy relaxation. However, if at the end of the current pulse, the magnetization is in the high energy region, the final state of the magnetization will depend on the exact point of the high energy region where it was at the time of current removal. This will result in a bias case switching diagram more dependent on the values of the parameters (current value or pulse duration) as will be discussed in the following sections.

5.2.2 Energy barriers of the two systems

The simplest thermal switching mechanism corresponds to coherent rotation: the rotation of the magnetization as a whole, without domains formation. To obtain the energy barriers of the system one needs to determine the position of the saddle points.

In the bias case, the saddle points correspond to the polar coordinates $\phi = 0$ and $\theta = \pi/2$, associated to the crossing of the separatrix line (see Fig.5.1(d)). The vector coordinates for the saddle points thus are $m_{saddle} = (1, 0, 0)$. The bias field H_X is fixed on the \hat{x} , so $(H_X, 0, 0)$. The equilibrium position is determined by eq.5.4, so $m_{eq} = (\sin\theta_{eq}, 0, \cos\theta_{eq})$. Remembering the anisotropy is on the \hat{z} direction and the bias field H_X is fixed on the \hat{x} , the energy barrier can be calculated introducing these quantities on eq.5.2 for the saddle and equilibrium points. The energy barrier F_B for coherent

rotation of the tilt case then becomes:

$$F_B = F_{saddle} - F_{eq} \quad (5.5)$$

$$F_B = \frac{\mu_0 M_s V (H_k - H_X)^2}{2H_k} = K_u \left(1 - \frac{H_X}{H_k}\right)^2. \quad (5.6)$$

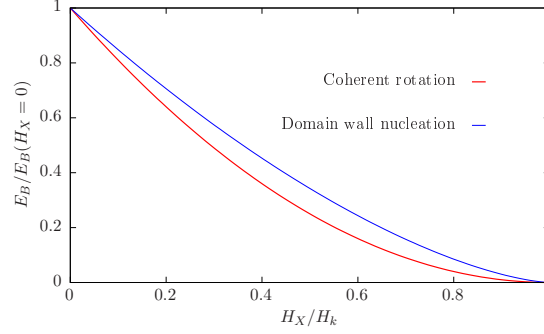


Figure 5.2: Energy barrier for coherent rotation and domain wall nucleation as a function of the exchange-bias field.

Using the same principles, the energy barrier when there is no bias field (tilt case), yields $F_B = K_u \cos^2 \beta$. For small values of β , $\cos \beta \approx 1$, and as such it is obtained the typical value of $E_B = K_u V$. Using an effective anisotropy constant $K_u = 2.65 \times 10^4 \text{ J/m}^3$ and an element of volume $100 \times 100 \times 1 \text{ nm}^3$, the thermal stability factor has the value $E_B/k_B T_{Room} = 64$. This value is close to the standard value $E_B/k_B T_{Room} = 60$ in magnetic recording[104] for thermal stability of ten years. In the anisotropy tilt case, the energy barrier height for coherent rotation (as well as the stability factor) is maintained because the tilt corresponds to a rigid rotation of the energy landscape without variations of its value. From the comparison of the coherent rotation value in zero field with Eq.5.6, one can conclude that the introduction of an antiferromagnetic layer, which produces a bias field orthogonal to the anisotropy axis, tends to reduce the energy barrier by a factor of $(1 - H_X/H_k)^2$.

Energy barriers for nucleation of a domain wall

The thermal switching process which is most likely to occur is the process with the minimum energy barrier. As we increase the size of the element, volume grows, and other switching processes with a smaller energy barrier become available, such as the thermal switching by nucleation and propagation of a domain wall. In order to consider this process the exchange energy $F_{ex} = A[(\nabla m_x)^2 + (\nabla m_y)^2 + (\nabla m_z)^2]$ (where A is the exchange constant) term needs to be introduced in eqs. 5.3 and 5.2¹.

¹The demonstrations are done in detail on section 3.6 of [105]

For the tilt case, the free energy of the system then becomes:

$$F_{tilt} = A\dot{\theta}^2 + K \cos^2 \theta \quad (5.7)$$

And the linear density of energy contained in a domain wall is given by:

$$F_w = \int_{-\infty}^{+\infty} [A\dot{\theta}^2 + K \cos^2 \theta] dx \quad (5.8)$$

where \hat{x} is the film plane and perpendicular to the domain wall. Solving by Euler-Lagrange equations, one finds:

$$F_w = \int^{2\pi} [A \frac{K}{A} \cos^2 \theta + K \cos^2 \theta] \frac{1}{\cos \theta} \sqrt{\frac{A}{K}} d\theta \quad (5.9)$$

$$= 4\sqrt{AK} \quad (5.10)$$

For the tilt case the energy barrier of a 180 degree wall then is[105]:

$$E_B = 4S\sqrt{AK_u} \quad (5.11)$$

where S is the smallest cross section of the device [105]. The saddle point configuration for that energy barrier corresponds to a 180° wall. For an element of cross section $S = 100nm^2$, an effective anisotropy constant $K_u = 2.65 \times 10^4 J/m^3$ and exchange constant $A = 1.5 \times 10^{-11} J/m$, the thermal stability factor becomes $E_B/k_B T_{Room} = 60.88$. The value of the energy barrier in the anisotropy tilt case is preserved because the saddle point configuration is also a 180° wall.

In the bias case, when a bias field H_x is present, the domains are tilted and the energy of the domain wall is reduced due to the smaller rotation of the magnetization inside the wall. The saddle point configuration then contains a domain wall of $\pi - 2\theta_{eq}$ as defined in Eq. 5.4. Following a similar procedure than the one in the tilt case, but with the energy density defined as:

$$F_{bias} = A\dot{\theta}^2 + K \cos^2 \theta + \mu_0 H_x M_s \quad (5.12)$$

The energy barrier for a domain wall in the bias case is then given by:

$$E_B = 4S\sqrt{AK_u} \left(\sqrt{1 - \left(\frac{H_x}{H_k}\right)^2} + \frac{2H_x}{H_k} \arctan\left(\frac{H_x - H_k}{\sqrt{H_k^2 - H_x^2}}\right) \right) \quad (5.13)$$

which is equivalent to the formula already found in literature [105]. The energy barrier for coherent rotation and domain wall nucleation is shown in Fig.5.2 as a function of the exchange bias field H_X . In both cases the energy barrier is reduced with respect to the tilt case (zero bias field) case. The energy barrier has to be calculated more precisely in the general case, where inhomogenities of the magnetization can play a role.

For the bias case, the domain wall width of the saddle configuration is field dependent and has the value

$$\Delta = \frac{\Delta_0(H_X + H_k)}{\sqrt{H_k^2 - H_X^2}} \quad (5.14)$$

where is $\Delta_0 = \sqrt{A/K_u}$. For such calculations the criterion of the derivative at the middle of the wall has been used. The thin films comprised of multilayers of HM/FM can also posses a chiral exchange of interfacial origin known as Dzyaloshinskii-Moriya interaction (DMI)[106]. In the presence of interfacial DMI the energy barrier corresponding to a DW nucleation will be reduced by a factor $-\pi DS$ [107] where D is the DMI constant. This is in agreement with some numerical calculations showing that DMI actually reduces the energy barrier for switching in magnetic nanoelements [108, 109].

In summary, the introduction of a bias field or DMI reduces the energy barrier, while the anisotropy tilt preserves it, independently of the type of thermal switching mechanism. However, the thermal mechanism does not determine the dynamical switching and has to be analyzed separately with numerical modeling. For this reason we explore the dynamics under applied current in the next sections.

5.3 Critical currents

Following the analytical discussion in the previous section we now investigate the effect of a current pulse on the SOT device using numerical calculations of the dynamics of magnetization as a function of the applied current induced damping like torque a_j and pulse time duration t_p . We use the same dynamics and torque equations for both the bias case and anisotropy tilt case, changing only the variable of interest: the bias field H_X for the bias case and the tilt angle β for the anisotropy tilt case (see Fig.5.1(a) and (b)). We focus on identifying the minimum necessary value of the dc current generated damping like torque a_j to obtain SOT switching, i.e. the critical current. We then interpret the results in light of the energy landscape obtained in the previous section².

The dynamics of the magnetization was calculated using the Landau-Lifshitz-Gilbert equation with the additional terms corresponding to the field-like and damping-like

²We have chosen to use the current torque in field units, since the macrospin problem can be normalized to the anisotropy field values and the actual value depends on the related material conditions.

spin orbit torques

$$\frac{d\hat{m}}{dt} = -\gamma\hat{m} \times (\vec{H}_{\text{eff}} + a_j(\hat{m} \times \hat{p}) + b_j \times \hat{p}) + \alpha\hat{m} \times \frac{d\hat{m}}{dt} \quad (5.15)$$

where γ is the gyromagnetic ratio and α is the Gilbert damping parameter. $\vec{H}_{\text{eff}} = -(1/\mu_0 M_s)\partial(E/V)/\partial\vec{m}$. We also use here the macrospin approach, where the magnetization is considered to be homogeneous in the magnetic layer. This approach has been shown to be valid as long as no strong DMI[110] is present or large applied currents are used[111]. For such situations, the switching is mediated by inhomogeneities like domain walls[110] and full micromagnetic simulations are required. The effective field contains the anisotropy field and in the bias case, the bias field is introduced inside \vec{H}_{eff} as an additional external field $H_X\hat{x}$. We consider the polarization direction of the spin Hall current to be $\hat{p} = (0,1,0)$. The ratio between field-like torque induced by the b_j current and damping-like torque connected to a_j is b_j/a_j and depends on the material; since in AFM/FM bilayers (bias case) it has been reported to be affected by the order of the stack [112], while in HM/FM bilayers (tilt case) it depends on interface effects on the ferromagnet, we have considered for simplicity three possible scenarios for the field like torque b_j : $b_j = a_j$; $b_j = 0$ and $b_j = -a_j$. The current pulse time and subsequent relaxation is governed by the step-like Heaviside function, since typical rise and fall times of pulse generators are in the range from about 20 to 100 ps and no capacitive or reactive phenomena are considered. The anisotropy constant corresponds to $\mu_0 H_k = 0.053 T$ as in Ref.[90]. The damping value, which can vary due to the different interfaces of the bias and anisotropy tilt cases, was anyhow fixed to be $\alpha = 0.05$ to be able to compare the various results.

In order to determine the critical current values for the SOT switching in the tilt and bias cases we start with the magnetization in the equilibrium state corresponding to the positive Z direction, then we apply a single $t_p = 100$ ns current pulse a_j and the results are shown in Figs. 5.3(a-c) bias case and 5.3(g-i) tilt case. The stability of both cases are also analyzed by letting the magnetization relax after the 100 ns pulse in Fig. 5.3(d-f) for the bias case and 5.3(j-l) for the anisotropy tilt case.

5.3.1 Anisotropy tilt case

For the anisotropy tilt case, we vary the amplitude of the $t_p = 100$ ns current pulse a_j and the angle β while fixing for simplicity the b_j values as described in the previous paragraph. In Fig. 5.3(g-i) we show the magnetization state right after the end of the pulse duration t_p . Here, since the energy landscape is not distorted but only rigidly rotated by an angle β (see Fig.5.1 (e)), the switching is rather robust.

The damping like torque caused by the applied current (a_j) pulls the magnetization to the plane of the sample ($m_z = 0$), and may be assisted by the field like torque b_j or the anisotropy tilt β depending on its respective directions (see blue trajectory on Fig.5.4(a)).

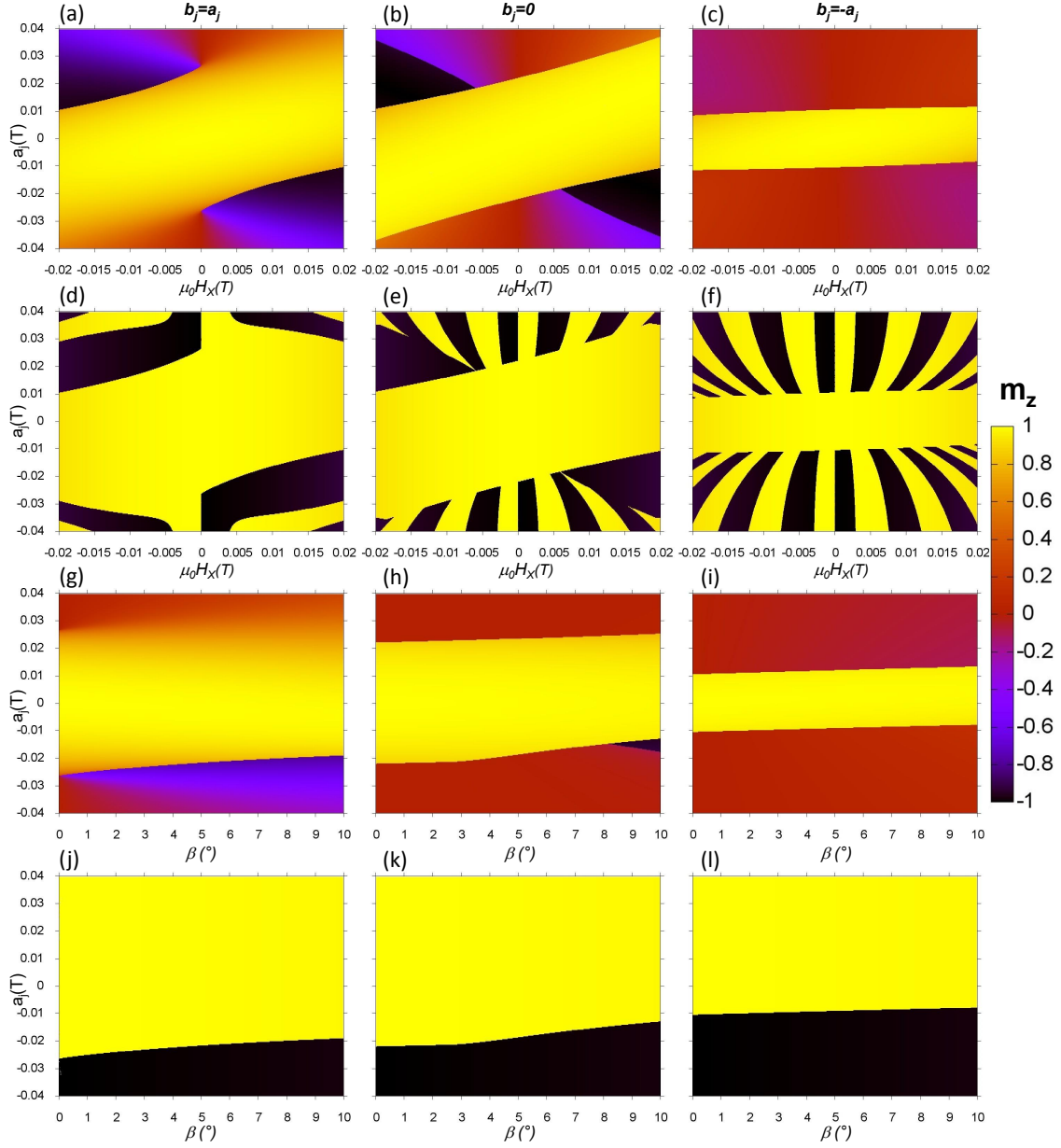


Figure 5.3: OOP magnetization map (m_z color coded) with different b_j values $b_j = a_j$; $b_j = 0$; $b_j = -a_j$ as a function of the intensity a_j of a current pulse lasting t_p : from a) to c) m_z is the bias case as a function of the bias in plane field (H_X) at the end of current pulse time $t_p = 100ns$, d) to f) the relaxed m_z for the bias case after 100 ns ($t = 2 * t_p$) upon removal of the current pulse; g) to i) Anisotropy tilt case as a function of the anisotropy tilt angle β at the end of current pulse time $t_p = 100ns$, j) to l) the relaxed m_z for the tilt case after 100 ns ($t = 2 * t_p$) upon removal of the current pulse;. Column-wise we observe the effect of the field-like torque b_j in the systems.

For $b_j = 0$ (Fig.5.3(h)), about 0.02 T of $|a_j|$ is enough to redirect the magnetization to the plane, and it is assisted by the anisotropy tilt for negative values. The necessary current for the redirection decreases increasing the tilt at negative values, and on the contrary increases for positive values. Meanwhile for $b_j = a_j$ the field like torque also opposes the switching, as it can be seen for the higher currents of Fig.5.3(g). On the contrary, the field like torque works in favor of the switching for $b_j = -a_j$ (Fig.5.3(g)).

With the magnetization on the plane of the sample, once the current pulse is removed, the system is in a high energy state, and it has to relax to a low energy one. If the adequate conditions are met, the magnetization can then evolve from $m_z \approx 0$ to $m_z = -1$ (red trajectory on Fig.5.4(a)). The bottom row of Fig.5.3 (j-l) shows the system state after the removal of the current pulse and subsequent relaxation. The switching occurs only for negative values of a_j , since in this direction it is bolstered by the rigid energy landscape rotation caused by the tilt, while for negative values no switching happens because for that current polarity, tilt and current torque work in opposite directions. The minimum absolute values of a_j for the switching, in other words the critical current, increases from positive to negative values of b_j , suggesting that the field like torque b_j assists the switching when it has a direction antagonistic to the damping like torque Fig.5.3(l).

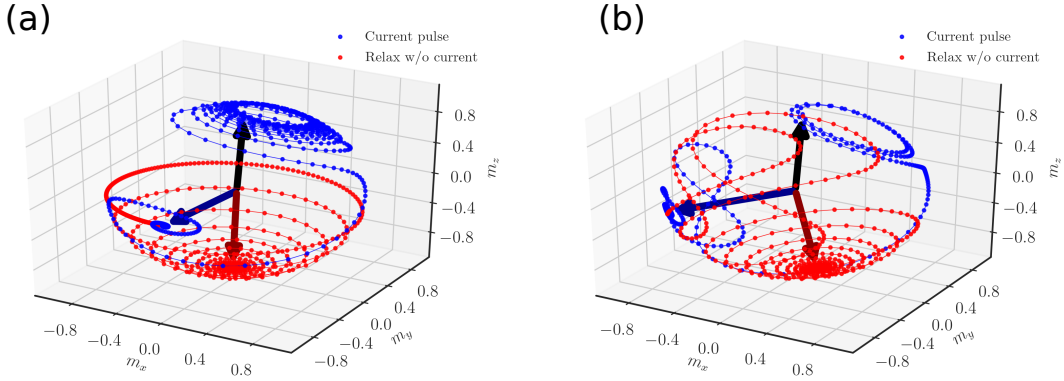


Figure 5.4: Simulation of the magnetization trajectory for field free switching with $a_j = -10$ mT and $b_j = -a_j$. Black arrow indicates the initial state, blue lines and dots dynamics with the current pulse and red lines and dots the relaxation upon removing of the current. a) Tilt case, $\beta = 3.5^\circ$. b) Bias case, $H_X = -10$ mT.

5.3.2 Bias case

In the numerical calculations of the bias case, we vary the applied current a_j and the bias field H_X . In Fig.5.3(a) to (c) one sees the final magnetization m_z right after the t_p pulse.

After the current pulse, the magnetization diagrams resemble to the ones obtained in the tilt case. Opposite signs between the bias field H_X and damping like torque a_j

are needed to pull the magnetization in-plane. The field like torque b_j influence, besides $b_j = -a_j$ (Fig. 5.3(c)), is different though. Generally less current is required to pull the magnetization in the film plane and it can even achieve switching with the help of $|H_X|$, as verified by the black regions of Figs.5.3(a) and 5.3(b).

However, after the removal of the current pulse, the relaxation is not so straightforward as in the tilt case. Since the energy landscape is distorted by H_X , the magnetization has to be also in condition to follow the right path through the lower energy landscape valleys, as evidenced by the lines in Fig.5.1(d) and the red trajectory of Fig.5.4(b). For $b_j = a_j$ and $b_j = 0$ (Figs.5.3 (d) and e)), if the system has already switched it still holds, but not necessarily if the magnetization has to evolve from close to the in-plane condition. Surprisingly, regions that were unlikely to switch do so, as the ones with same signs of H_X and a_j . On the other hand, if the magnetization is close to in-plane, the system does not follow the simple continuous behavior, which was verified before on the tilt case, and alternating regions with successful and unsuccessful switching are found.

This is the consequence of a complicated interplay between the spin orbit torques and the current pulse duration, which has been already pointed out by Mangin et al.[79] and discussed by Miron et al.[74]. During the precession period, each of the spin orbit torques (a_j and b_j) changes their directions in reference to the magnetization. Thus their actual role in either aiding or obstructing the magnetization switching will depend not only on their intensity and relative directions, but also on the state of the magnetization itself at any given instant. In the simulations just discussed above, large current-pulse-times were used to guarantee a quasi-stationary behavior (net torque equal to zero). The effect of the pulse duration will be further analyzed in section 5.4.

5.3.3 SOT switching efficiency

Looking at the critical current values $a_{j,c}$ associated to the sign changing of m_z in Fig.5.3, it may seem that the bias case is a more energy efficient method to achieve SOT magnetization switching for memory applications. Nevertheless, to properly compare the bias and anisotropy tilt switching methods, one needs to normalize the value of the critical current $a_{j,c}$ applied during the $t_p = 100$ ns pulse, used to reach the final relaxed state with respect to the energy barrier E_B encountered in the switching process as defined in Eq. 5.6. To this end in Fig. 5.5 we plot the ratio between the module of the critical current and the relevant energy barrier ($|a_{j,c}|/E_B$) as a figure of merit representing the efficiency of both the bias and the tilt cases.

Comparing Figs.5.5(a) and (b), in the tilt case we find an evident decrease of the ratio $|a_{j,c}|/E_B$ when the tilt angle β increases; on the contrary, an increase of the ratio $|a_{j,c}|/E_B$ is observed when H_X increases in the bias case. Since in both cases there is a reduction of $a_{j,c}$ with increasing values of the relevant input parameter H_X or β as shown in 5.3, we can deduce that the decrease in the energy barrier height E_B with increasing H_X in the bias case, must be larger than the reduction of the critical current

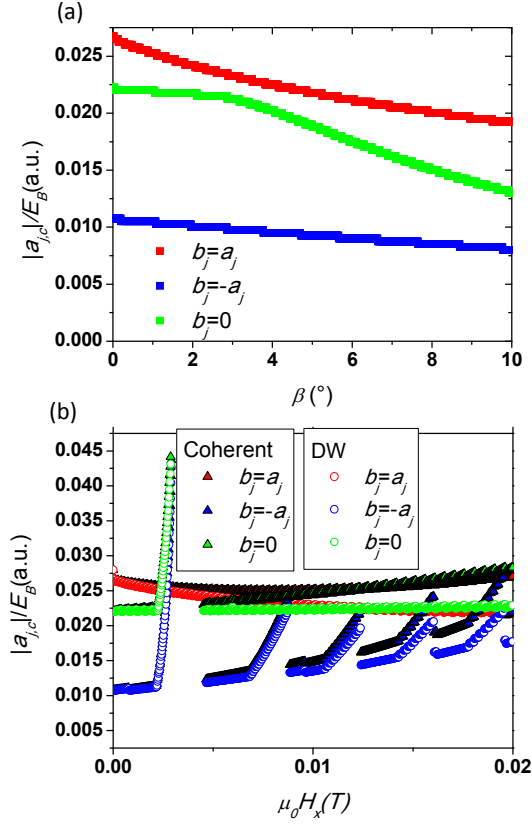


Figure 5.5: Figure of merit $a_{j,c}/E_B$ for (a) Tilt case as a function of the tilt angle β and (b) Bias case as function of the bias field H_X .

$|a_{j,c}|$ with H_X .

This means that in the bias case we observe an important degrading in the energy barrier. Although this still corresponds to smaller energy requirements on the SOT switching of a possible device, it also entails a lower thermal stability and also limits the degree of miniaturization. On the other hand, a larger $|a_{j,c}|$ current needed to switch the magnetization direction in the tilt case would also generate more heat by Joule effect, and this might compromise miniaturization as well. So specific optimization choices are needed in each case for the tailored development of specific SOT applications.

5.4 Switching dependence on pulse duration

Another important feature which we need to include in the analysis of hypothetical SOT devices is the ultimate speed of operation. To this end we show here the effect of different current pulse durations t_p on the final magnetization state achieved after a $t = 10t_p$ relaxation time, see Fig. 5.6. The current a_j is fixed at a value where switching

is achieved, and close to the critical current $|a_{j,c}|$ and then we vary both the tilt angle β or the bias field H_x and also the pulse duration t_p . After relaxation without applied current for $t = 10t_p$, we draw a black dot in the graph if the switching takes place or a white one if switching does not occur. Fig.5.6(a) to (c) shows switching speed for

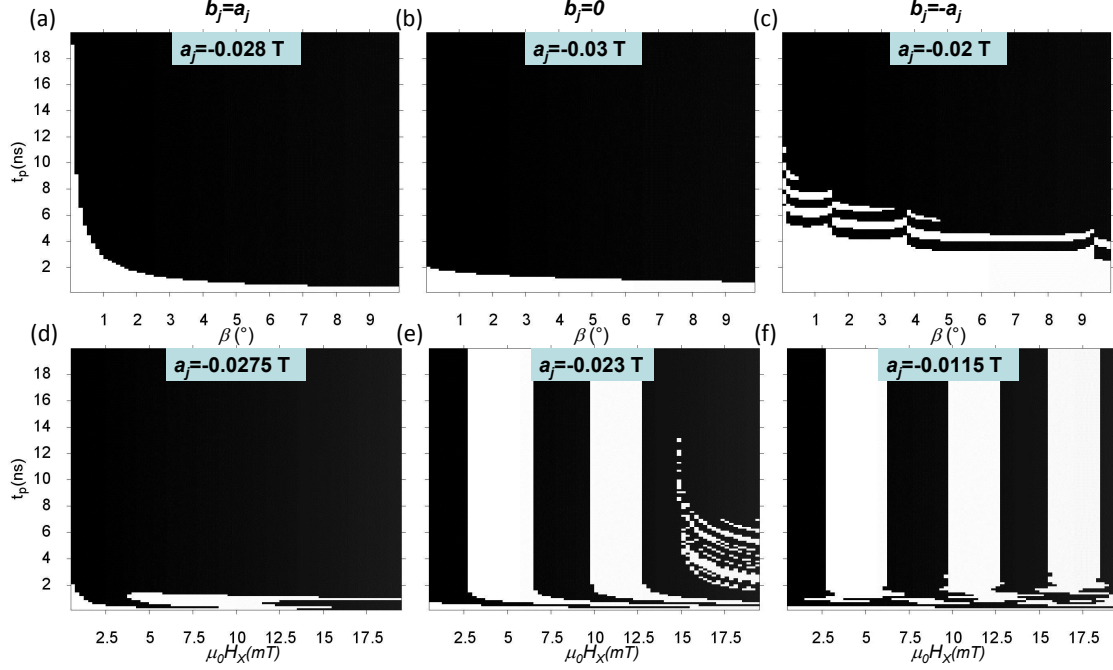


Figure 5.6: SOT switching in the tilt case for different pulse duration t_p as a function of tilt angle β for (a) field-torque equal to damping-torque $b_j = a_j$ (b) no field-like torque $b_j = 0$ (c) and inverted sign between torques $b_j = -a_j$. In the next row, SOT switching in the bias case for different pulse duration t_p as a function of the bias field H_x for (d) field-torque equal to damping-torque $b_j = a_j$ (e) no field-like torque $b_j = 0$ (f) and inverted sign between torques $b_j = -a_j$. Black dot means switched state and white dot not switched.

the tilt case. For both $b_j = a_j$ and $b_j = 0$ the switching is permanent for a pulse duration $t_p > 3$ ns. With the exception of the much slower $b_j = -a_j$ case, the performance of a tilt based device results far faster than an AFM/FM stack with bias field. However the fastest speed here is found when $b_j = 0$, a condition which is unlikely to be achieved in real samples, due to the fact that the physical phenomena which tend to generate the damping-like torque b_j also tend to produce a field-like one a_j [77].

Fig 5.6(d) to (f) shows the bias case. Here the $b_j = a_j$ case behaves quite well and manages to be stable. There are some instabilities near zero field, which are expected due to the necessity of perturb the energy landscape with an external field to obtain a field-free switching system. The other two cases $b_j = 0$, and $b_j = -a_j$ present considerable areas where switching does not occur. Particularly, the $b_j = 0$ case is mostly unstable

above 15 mT.

The pulse duration analysis shows that extra care is needed to choose the operating current value. Not only the minimum switching current has to be considered, but also how the system evolves and relaxes with time. As mentioned above, the field-like and damping-like torque have different signs during the precession period, and the specific instant at which they are removed interferes with the trajectory taken by the magnetization m_z to the final state.

5.5 Conclusions

We have analyzed the field-free switching by spin-orbit torques for two different mechanism that yield to a deterministic behavior with HM/FM with tilted anisotropy and AFM/FM bilayers with bias field. While in the tilt case the energy barrier is preserved with increasing anisotropy tilt angles, we have found a significant reduction of the anisotropy energy barrier for the bias case caused by the bias field. For a comparison the Landau-Lifshitz-Gilbert equation was also solved numerically in a macrospin approximation with added damping-like and field-like torques as a function of the variable of interest for each case (tilt angle or bias field).

Our numerical simulations confirmed the analytical results of a reduction of the energy barrier for the AFM/FM bias field case. On the other hand, in the HM/FM anisotropy tilt case, we have shown the switching to be specially robust with small variations of the tilt angle. Moreover, this method also tolerates a certain flexibility on the chosen HM layer, allowing to employ novel materials with giant spin Hall angles (as the oxygen doped W and Ta) [113, 75, 114, 115, 116] and consequently to lower the required current densities. Since most of the other -more complex- switching methods proposed, and not considered in this paper, also present a coupling with another layer, and hence a potential energy barrier reduction, we thus believe that the tilt case to be a strong contender towards future practical magnetic memory applications. The missing piece is then to find a way to systematically generate a small anisotropy tilt on the FM layer. This may be done, for example, by tweaking the deposition process, introducing an inhomogeneity of the sputtering on the target or causing a mismatch in the crystalline axis of the layers in the interface.

Chapter 6

Final Remarks

In this thesis soft magnetic thin films were investigated by magnetization dynamics. The experimental characterization was done by ferromagnetic resonance and the theoretical by macrospins simulations supported by analytical solutions.

The experimental part, concerning the ferromagnetic resonance experimental technique was deeply studied, both from the instrumentation point of view (with the interferometer implementation) and the characterization of FeSiB amorphous thin films. Moreover, micromagnetic simulations were performed to identify the non-linear modes presented in the stripe domains regime of the films. The results were presented at the Joint Magnetic Symposium, held in Uppsalla, from 26-29 of August of 2019. After solving the field accuracy issue, we intend to publish the results.

The theoretical part investigates the dynamics of magnetic switching of thin film by spin orbit torque. The work is of great importance in the field of spintronics, where we hope it play a role in identifying the proper field-free switching method for three-terminal applications. The investigation was conducted by the candidate and was published in the Journal of Magnetism and Magnetic materials [69].

Recently, there have been reports of controlling the propagation of spin waves in stripe domains by means of spin currents. One can rotate the longitudinal direction of the stripe domains, by applying a static field. This rotation can also be achieved by means of an spin current, in absence of an external field. One them needs to combine both the approaches of chapters 4 and 5, opening a lot of possibilities for novel electronic devices.

In summary, the PhD were of great didactic value to the candidate, where he could learn and apply a wide variety of experimental and theoretical skills: ferromagnetic resonance characterization and instrumentation, micromagnetic and macrospin simulations supported by analytical solutions. Those skills will be of great value in the future for the candidate career.

Bibliography

- [1] William Gilbert. *De Magnete, Magneticisque Corporibus, et de Magno Magnete Tellure*. 1600.
- [2] Walther Gerlach and Otto Stern. “Der experimentelle Nachweis der Richtungsquantelung im Magnetfeld”. In: *Zeitschrift für Physik* 9.1 (1922), pp. 349–352. ISSN: 0044-3328. DOI: [10.1007/BF01326983](https://doi.org/10.1007/BF01326983). URL: <https://doi.org/10.1007/BF01326983>.
- [3] Walther Gerlach and Otto Stern. “Das magnetische Moment des Silberatoms”. In: *Zeitschrift für Physik* 9.1 (1922), pp. 353–355. ISSN: 0044-3328. DOI: [10.1007/BF01326984](https://doi.org/10.1007/BF01326984). URL: <https://doi.org/10.1007/BF01326984>.
- [4] Friedel Weinert. “Wrong theory—Right experiment: The significance of the Stern-Gerlach experiments”. In: *Studies in History and Philosophy of Science Part B: Studies in History and Philosophy of Modern Physics* 26.1 (1995), pp. 75–86. ISSN: 1355-2198. DOI: [https://doi.org/10.1016/1355-2198\(95\)00002-B](https://doi.org/10.1016/1355-2198(95)00002-B). URL: <http://www.sciencedirect.com/science/article/pii/S135521989500002B>.
- [5] L.D. Landau and E.M. Lifshitz. “Theory of the dispersion of magnetic permeability in ferromagnetic bodies”. In: *Phys. Z. Sowietunion* 8 (1935), p. 151.
- [6] Anonymous. “Abstracts of Papers to be Presented at the 1955 Thanksgiving Meeting at the University of Chicago, Chicago, Illinois, November 25 and 26, 1955”. In: *Phys. Rev.* 100 (4 Nov. 1955), pp. 1235–1235. DOI: [10.1103/PhysRev.100.1235](https://link.aps.org/doi/10.1103/PhysRev.100.1235). URL: <https://link.aps.org/doi/10.1103/PhysRev.100.1235>.
- [7] GT Rado and JR Weertman. “Spin-wave resonance in a ferromagnetic metal”. In: *Journal of Physics and chemistry of solids* 11.3-4 (1959), pp. 315–333.
- [8] C. D. Graham B. D. Cullity. *Introduction to magnetic materials*. 2nd ed. Wiley-IEEE Press, 2008.
- [9] Giorgio Bertotti. *Hysteresis in magnetism : for physicists, materials scientists, and engineers*. Electromagnetism. Academic Press, 1998.

-
- [10] John David Jackson. *Classical electrodynamics*. 3rd ed. New York, NY: Wiley, 1999. ISBN: 9780471309321. URL: <http://cdsweb.cern.ch/record/490457>.
- [11] S. V. Vonsovskii. *Ferromagnetic Resonance*. 1966.
- [12] Daniel D. Stancil (auth.) Anil Prabhakar. *Spin waves: theory and applications*. 1st ed. Springer US, 2009. URL: <http://gen.lib.rus.ec/book/index.php?md5=3c13a5e70eb37f0148db885c3b7846f7>.
- [13] J Smith and HJ Beljers. “Ferromagnetic resonance absorption in BaFe₁₂O₁₉, a highly anisotropic crystal”. In: *Philips Res. Rep* 10 (1955), pp. 113–130.
- [14] D.C. Ralph and M.D. Stiles. “Spin transfer torques”. In: *Journal of Magnetism and Magnetic Materials* 320.7 (2008), pp. 1190–1216. ISSN: 0304-8853. DOI: <https://doi.org/10.1016/j.jmmm.2007.12.019>. URL: <http://www.sciencedirect.com/science/article/pii/S0304885307010116>.
- [15] A. Manchon et al. “Current-induced spin-orbit torques in ferromagnetic and antiferromagnetic systems”. In: *Rev. Mod. Phys.* 91 (3 Sept. 2019), p. 035004. DOI: [10.1103/RevModPhys.91.035004](https://doi.org/10.1103/RevModPhys.91.035004). URL: <https://link.aps.org/doi/10.1103/RevModPhys.91.035004>.
- [16] L. Berger. “Low-field magnetoresistance and domain drag in ferromagnets”. In: *Journal of Applied Physics* 49.3 (1978). cited By 320, pp. 2156–2161. DOI: [10.1063/1.324716](https://doi.org/10.1063/1.324716).
- [17] L. Berger. “Domain drag effect in the presence of variable magnetic field or variable transport current”. In: *Journal of Applied Physics* 50.B3 (1979). cited By 33, pp. 2137–2139. DOI: [10.1063/1.327083](https://doi.org/10.1063/1.327083).
- [18] P.P. Freitas and L. Berger. “Observation of s-d exchange force between domain walls and electric current in very thin Permalloy films”. In: *Journal of Applied Physics* 57.4 (1985). cited By 131, pp. 1266–1269. DOI: [10.1063/1.334524](https://doi.org/10.1063/1.334524).
- [19] C.-Y. Hung and L. Berger. “Exchange forces between domain wall and electric current in permalloy films of variable thickness”. In: *Journal of Applied Physics* 63.8 (1988). cited By 86, pp. 4276–4278. DOI: [10.1063/1.340201](https://doi.org/10.1063/1.340201).
- [20] P. Grünberg et al. “Layered Magnetic Structures: Evidence for Antiferromagnetic Coupling of Fe Layers across Cr Interlayers”. In: *Phys. Rev. Lett.* 57 (19 Nov. 1986), pp. 2442–2445. DOI: [10.1103/PhysRevLett.57.2442](https://doi.org/10.1103/PhysRevLett.57.2442). URL: <https://link.aps.org/doi/10.1103/PhysRevLett.57.2442>.
- [21] M.N. Baibich et al. “Giant magnetoresistance of (001)Fe/(001)Cr magnetic superlattices”. In: *Physical Review Letters* 61.21 (1988). cited By 7013, pp. 2472–2475. DOI: [10.1103/PhysRevLett.61.2472](https://doi.org/10.1103/PhysRevLett.61.2472).

-
- [22] G. Binasch et al. “Enhanced magnetoresistance in layered magnetic structures with antiferromagnetic interlayer exchange”. In: *Physical Review B* 39.7 (1989), cited By 2805, pp. 4828–4830. DOI: [10.1103/PhysRevB.39.4828](https://doi.org/10.1103/PhysRevB.39.4828).
- [23] J.C. Slonczewski. “Current-driven excitation of magnetic multilayers”. In: *Journal of Magnetism and Magnetic Materials* 159.1-2 (1996), cited By 4767, pp. L1–L7. DOI: [10.1016/0304-8853\(96\)00062-5](https://doi.org/10.1016/0304-8853(96)00062-5).
- [24] Ya G Dorfman. “On the mechanics of magnetic phenomena z”. In: *Phys* 17 (1923), p. 98.
- [25] S Al’tshuler, YK Zavoisky, and BM Kozyrev. “New method to study paramagnetic absorption”. In: *Zhurn. Eksperiment. Teoret. Fiziki* 14.10-11 (1944), pp. 407–409.
- [26] Cornelis Jacobus Gorter. *Paramagnetic relaxation*. Elsevier Publishing Company, 1947.
- [27] J. H. E. GRIFFITHS. “Anomalous High-frequency Resistance of Ferromagnetic Metals”. In: *Nature* 158.4019 (1946), pp. 670–671. ISSN: 1476-4687. DOI: [10.1038/158670a0](https://doi.org/10.1038/158670a0). URL: <https://doi.org/10.1038/158670a0>.
- [28] E Zavoisky. “Spin magnetic resonance in the decimetre-wave region”. In: *J. Phys. USSR* 10 (1946), pp. 197–198.
- [29] Charles Kittel. “Interpretation of Anomalous Larmor Frequencies in Ferromagnetic Resonance Experiment”. In: *Phys. Rev.* 71 (4 Feb. 1947), pp. 270–271. DOI: [10.1103/PhysRev.71.270.2](https://link.aps.org/doi/10.1103/PhysRev.71.270.2). URL: <https://link.aps.org/doi/10.1103/PhysRev.71.270.2>.
- [30] Charles Kittel. “On the Theory of Ferromagnetic Resonance Absorption”. In: *Phys. Rev.* 73 (2 Jan. 1948), pp. 155–161. DOI: [10.1103/PhysRev.73.155](https://doi.org/10.1103/PhysRev.73.155). URL: <https://link.aps.org/doi/10.1103/PhysRev.73.155>.
- [31] J. H. Van Vleck. “Concerning the Theory of Ferromagnetic Resonance Absorption”. In: *Phys. Rev.* 78 (3 May 1950), pp. 266–274. DOI: [10.1103/PhysRev.78.266](https://doi.org/10.1103/PhysRev.78.266). URL: <https://link.aps.org/doi/10.1103/PhysRev.78.266>.
- [32] Brian C. Wadell. *Transmission line design handbook*. Addison-Wesley, 1991. ISBN: 0-89006-436-9.
- [33] M. D. Pozar. *Microwave engineering*. 2012.
- [34] W. Barry. “A Broad-Band, Automated, Stripline Technique for the Simultaneous Measurement of Complex Permittivity and Permeability”. In: *IEEE Transactions on Microwave Theory and Techniques* 34.1 (Jan. 1986), pp. 80–84. ISSN: 1557-9670. DOI: [10.1109/TMTT.1986.1133283](https://doi.org/10.1109/TMTT.1986.1133283).

- [35] Sangita S. Kalarickal et al. “Ferromagnetic resonance linewidth in metallic thin films: Comparison of measurement methods”. In: *Journal of Applied Physics* 99.9 (2006), p. 093909. DOI: [10.1063/1.2197087](https://doi.org/10.1063/1.2197087). eprint: <https://doi.org/10.1063/1.2197087>. URL: <https://doi.org/10.1063/1.2197087>.
- [36] C. Bilzer et al. “Vector network analyzer ferromagnetic resonance of thin films on coplanar waveguides: Comparison of different evaluation methods”. In: *Journal of Applied Physics* 101.7 (2007), p. 074505. DOI: [10.1063/1.2716995](https://doi.org/10.1063/1.2716995). eprint: <https://doi.org/10.1063/1.2716995>. URL: <https://doi.org/10.1063/1.2716995>.
- [37] George B. Arfken, Hans J. Weber, and Frank E. Harris. “Chapter 5 - Vector Spaces”. In: *Mathematical Methods for Physicists (Seventh Edition)*. Ed. by George B. Arfken, Hans J. Weber, and Frank E. Harris. Seventh Edition. Boston: Academic Press, 2013, pp. 251–297. ISBN: 978-0-12-384654-9. DOI: <https://doi.org/10.1016/B978-0-12-384654-9.00005-0>. URL: <http://www.sciencedirect.com/science/article/pii/B9780123846549000050>.
- [38] Ivan S. Maksymov and Mikhail Kostylev. “Broadband stripline ferromagnetic resonance spectroscopy of ferromagnetic films, multilayers and nanostructures”. In: *Physica E: Low-dimensional Systems and Nanostructures* 69 (2015), pp. 253–293. ISSN: 1386-9477. DOI: <https://doi.org/10.1016/j.physe.2014.12.027>. URL: <http://www.sciencedirect.com/science/article/pii/S1386947714004664>.
- [39] Justin M. Shaw et al. “Precise determination of the spectroscopic g-factor by use of broadband ferromagnetic resonance spectroscopy”. In: *Journal of Applied Physics* 114.24 (2013), p. 243906. DOI: [10.1063/1.4852415](https://doi.org/10.1063/1.4852415). eprint: <https://doi.org/10.1063/1.4852415>. URL: <https://doi.org/10.1063/1.4852415>.
- [40] C. Gonzalez-Fuentes, R. K. Dumas, and C. García. “Systematic errors in the determination of the spectroscopic g-factor in broadband ferromagnetic resonance spectroscopy: A proposed solution”. In: *Journal of Applied Physics* 123.2 (2018), p. 023901. DOI: [10.1063/1.5003408](https://doi.org/10.1063/1.5003408). eprint: <https://doi.org/10.1063/1.5003408>. URL: <https://doi.org/10.1063/1.5003408>.
- [41] IE Dzialoshinskii. “Thermodynamic theory of weak ferromagnetism in antiferromagnetic substances”. In: *Soviet Physics JETP-USSR* 5.6 (1957), pp. 1259–1272.
- [42] Tôru Moriya. “Anisotropic superexchange interaction and weak ferromagnetism”. In: *Physical Review* 120.1 (1960), p. 91.
- [43] Seung-Jae Lee et al. “Spin-wave propagation in the presence of inhomogeneous Dzyaloshinskii-Moriya interactions”. In: *Phys. Rev. B* 96 (18 Nov. 2017), p. 184433. DOI: [10.1103/PhysRevB.96.184433](https://doi.org/10.1103/PhysRevB.96.184433). URL: <https://link.aps.org/doi/10.1103/PhysRevB.96.184433>.

-
- [44] S. Sievers et al. “Microwave Interferometry for High Sensitivity VNA-FMR Measurements”. In: *IEEE Transactions on Magnetics* 53.4 (Apr. 2017), pp. 1–4. ISSN: 1941-0069. DOI: [10.1109/TMAG.2016.2623839](https://doi.org/10.1109/TMAG.2016.2623839).
- [45] S. Tamaru et al. “Vector network analyzer ferromagnetic resonance spectrometer with field differential detection”. In: *Review of Scientific Instruments* 89.5 (2018), p. 053901. DOI: [10.1063/1.5022762](https://doi.org/10.1063/1.5022762). eprint: <https://doi.org/10.1063/1.5022762>. URL: <https://doi.org/10.1063/1.5022762>.
- [46] Eric Montoya et al. “Broadband ferromagnetic resonance system and methods for ultrathin magnetic films”. In: *Journal of Magnetism and Magnetic Materials* 356 (2014), pp. 12–20. ISSN: 0304-8853. DOI: <https://doi.org/10.1016/j.jmmm.2013.12.032>. URL: <http://www.sciencedirect.com/science/article/pii/S0304885313009256>.
- [47] Y. Khivintsev et al. “Nonlinear ferromagnetic resonance in permalloy films: A nonmonotonic power-dependent frequency shift”. In: *Phys. Rev. B* 81 (5 Feb. 2010), p. 054436. DOI: [10.1103/PhysRevB.81.054436](https://link.aps.org/doi/10.1103/PhysRevB.81.054436). URL: <https://link.aps.org/doi/10.1103/PhysRevB.81.054436>.
- [48] Dustin M. Lattery et al. “Low Gilbert Damping Constant in Perpendicularly Magnetized W/CoFeB/MgO Films with High Thermal Stability”. In: *Scientific Reports* 8.1 (2018), p. 13395. ISSN: 2045-2322. DOI: [10.1038/s41598-018-31642-9](https://doi.org/10.1038/s41598-018-31642-9). URL: <https://doi.org/10.1038/s41598-018-31642-9>.
- [49] Paola Tiberto and Franco Vinai. *Magnetic Amorphous Alloys: Structural Magnetic and Transport Properties*. 2003.
- [50] F. Luborsky et al. “Formation and magnetic properties of Fe-B-Si amorphous alloys”. In: *IEEE Transactions on Magnetics* 15.4 (1979), pp. 1146–1149.
- [51] K. Hoselitz. “Magnetic properties of iron-boron-silicon metallic glasses”. In: *Journal of Magnetism and Magnetic Materials* 20.2 (1980), pp. 201–206. ISSN: 0304-8853. DOI: [https://doi.org/10.1016/0304-8853\(80\)90457-6](https://doi.org/10.1016/0304-8853(80)90457-6). URL: <http://www.sciencedirect.com/science/article/pii/S0304885380904576>.
- [52] Shiqiang Yue et al. “Magnetic and thermal stabilities of FeSiB eutectic amorphous alloys: Compositional effects”. In: *Journal of Alloys and Compounds* 776 (2019), pp. 833–838. ISSN: 0925-8388. DOI: <https://doi.org/10.1016/j.jallcom.2018.10.331>. URL: <http://www.sciencedirect.com/science/article/pii/S0925838818340234>.
- [53] J. Jiao et al. “The use of eutectic Fe-Si-B alloy as a phase change material in thermal energy storage systems”. In: *Materials* 12.14 (2019). cited By 2. DOI: [10.3390/ma12142312](https://doi.org/10.3390/ma12142312).

- [54] Z.G Sun et al. "Magnetic properties and domain structures of FeSiB thin films prepared by RF-sputtering method". In: *Journal of Magnetism and Magnetic Materials* 272-276 (2004). Proceedings of the International Conference on Magnetism (ICM 2003), pp. 1160–1161. ISSN: 0304-8853. DOI: <https://doi.org/10.1016/j.jmmm.2003.12.764>. URL: <http://www.sciencedirect.com/science/article/pii/S0304885303016779>.
- [55] Z.G. Sun, H. Kuramochi, and H. Akinaga. "Domain structures of nanocrystalline Fe₇₈Si₁₀B₁₂ thin films". In: *Applied Surface Science* 244.1 (2005). 12th International Conference on Solid Films and Surfaces, pp. 489–493. ISSN: 0169-4332. DOI: <https://doi.org/10.1016/j.apsusc.2004.09.155>. URL: <http://www.sciencedirect.com/science/article/pii/S0169433204017507>.
- [56] M. Dobromir et al. "Magnetic properties of Fe-based amorphous thin films". In: *Journal of Optoelectronics and Advanced Materials* 10.2 (2008). cited By 2, pp. 410–412. URL: <https://www.scopus.com/inward/record.uri?eid=2-s2.0-40549100417&partnerID=40&md5=8d782e9d72157709495d1fd62f18a047>.
- [57] M. Dobromir et al. "Surface and bulk magnetic behavior of Fe–Si–B amorphous thin films". In: *Journal of Magnetism and Magnetic Materials* 316.2 (2007). Proceedings of the Joint European Magnetic Symposia, e904–e907. ISSN: 0304-8853. DOI: <https://doi.org/10.1016/j.jmmm.2007.03.136>. URL: <http://www.sciencedirect.com/science/article/pii/S030488530700488X>.
- [58] Maria Neagu et al. "The surface magnetism investigation of FeSiB amorphous thin films obtained by evaporation technique". In: *Sensors and Actuators A: Physical* 129.1 (2006). EMSA 2004, pp. 172–175. ISSN: 0924-4247. DOI: <https://doi.org/10.1016/j.sna.2005.11.037>. URL: <http://www.sciencedirect.com/science/article/pii/S0924424705006874>.
- [59] Marco Coïsson et al. "Stripe domains and spin reorientation transition in Fe₇₈B₁₃Si₉ thin films produced by rf sputtering". In: *Journal of Applied Physics* 104.3 (2008), p. 033902. DOI: [10.1063/1.2960454](https://doi.org/10.1063/1.2960454). eprint: <https://doi.org/10.1063/1.2960454>. URL: <https://doi.org/10.1063/1.2960454>.
- [60] M. Coïsson et al. "Magnetic properties of FeSiB thin films displaying stripe domains". In: *Journal of Magnetism and Magnetic Materials* 321.7 (2009). cited By 50, pp. 806–809. DOI: [10.1016/j.jmmm.2008.11.072](https://doi.org/10.1016/j.jmmm.2008.11.072).
- [61] Marco Coïsson et al. "Rotatable magnetic anisotropy in Fe₇₈Si₉B₁₃ thin films displaying stripe domains". In: *Applied Surface Science* 476 (2019), pp. 402–411. ISSN: 0169-4332. DOI: <https://doi.org/10.1016/j.apsusc.2019.01.126>. URL: <http://www.sciencedirect.com/science/article/pii/S0169433219301412>.
- [62] P. Tiberto et al. "Spin Reorientation Transition in Amorphous FeBSi Thin Films Submitted to Thermal Treatments". In: *IEEE Transactions on Magnetics* 44.11 (2008), pp. 3921–3924.

- [63] Jun Yu et al. “Thermal annealing effect on FeCoB soft underlayer for perpendicular magnetic recording”. In: *Journal of Applied Physics* 91.10 (2002), pp. 8357–8359. DOI: [10.1063/1.1452279](https://doi.org/10.1063/1.1452279). eprint: <https://aip.scitation.org/doi/pdf/10.1063/1.1452279>. URL: <https://aip.scitation.org/doi/abs/10.1063/1.1452279>.
- [64] Martin A. W. Schoen et al. “Magnetic properties in ultrathin 3d transition-metal binary alloys. II. Experimental verification of quantitative theories of damping and spin pumping”. In: *Phys. Rev. B* 95 (13 Apr. 2017), p. 134411. DOI: [10.1103/PhysRevB.95.134411](https://doi.org/10.1103/PhysRevB.95.134411). URL: <https://link.aps.org/doi/10.1103/PhysRevB.95.134411>.
- [65] Mikihiro Oogane et al. “Magnetic Damping in Ferromagnetic Thin Films”. In: *Japanese Journal of Applied Physics* 45.5A (May 2006), pp. 3889–3891. DOI: [10.1143/jjap.45.3889](https://doi.org/10.1143/jjap.45.3889).
- [66] C. Scheck, L. Cheng, and W. E. Bailey. “Low damping in epitaxial sputtered iron films”. In: *Applied Physics Letters* 88.25 (2006), p. 252510. DOI: [10.1063/1.2216031](https://doi.org/10.1063/1.2216031). eprint: <https://doi.org/10.1063/1.2216031>. URL: <https://doi.org/10.1063/1.2216031>.
- [67] Arne Vansteenkiste et al. “The design and verification of MuMax3”. In: *AIP Advances* 4.10 (2014), p. 107133. DOI: [10.1063/1.4899186](https://doi.org/10.1063/1.4899186). eprint: <https://doi.org/10.1063/1.4899186>. URL: <https://doi.org/10.1063/1.4899186>.
- [68] Fausto Fiorillo. *Characterization and Measurement of Magnetic Materials (Electromagnetism)*. Academic Press, 2005. ISBN: 0122572513,9780122572517.
- [69] F. Garcia-Sanchez, G. Soares, and M. Pasquale. “A comparison of two different mechanisms for deterministic spin orbit torque magnetization switching”. In: *Journal of Magnetism and Magnetic Materials* 508 (2020), p. 166700. ISSN: 0304-8853. DOI: <https://doi.org/10.1016/j.jmmm.2020.166700>. URL: <http://www.sciencedirect.com/science/article/pii/S0304885319337680>.
- [70] Hans Jürgen Richter. “Recent advances in the recording physics of thin-film media”. In: *Journal of Physics D: Applied Physics* 32.21 (Oct. 1999), R147–R168. DOI: [10.1088/0022-3727/32/21/201](https://doi.org/10.1088/0022-3727/32/21/201).
- [71] Matthias Eschrig. “Spin-polarized supercurrents for spintronics: a review of current progress”. In: *Reports on Progress in Physics* 78.10 (Sept. 2015), p. 104501. DOI: [10.1088/0034-4885/78/10/104501](https://doi.org/10.1088/0034-4885/78/10/104501). URL: <https://doi.org/10.1088/0034-4885/78/10/104501>.
- [72] D. Apalkov, B. Dieny, and J. M. Slaughter. “Magnetoresistive Random Access Memory”. In: *Proceedings of the IEEE* 104.10 (Oct. 2016), pp. 1796–1830. DOI: [10.1109/JPROC.2016.2590142](https://doi.org/10.1109/JPROC.2016.2590142).

-
- [73] Andrew D. Kent and Daniel C. Worledge. “A new spin on magnetic memories”. In: *Nature Nanotechnology* 10 (Mar. 2015), p. 187. URL: <https://doi.org/10.1038/nnano.2015.24>.
- [74] Ioan Mihai Miron et al. “Perpendicular switching of a single ferromagnetic layer induced by in-plane current injection”. In: *Nature* 476.7359 (2011), pp. 189–193. ISSN: 1476-4687. DOI: [10.1038/nature10309](https://doi.org/10.1038/nature10309). URL: <https://doi.org/10.1038/nature10309>.
- [75] Luqiao Liu et al. “Spin-Torque Switching with the Giant Spin Hall Effect of Tantalum”. In: *Science* 336.6081 (2012), pp. 555–558. ISSN: 0036-8075. DOI: [10.1126/science.1218197](https://doi.org/10.1126/science.1218197). eprint: <https://science.sciencemag.org/content/336/6081/555.full.pdf>. URL: <https://science.sciencemag.org/content/336/6081/555>.
- [76] Kevin Garello et al. “Ultrafast magnetization switching by spin-orbit torques”. In: *Applied Physics Letters* 105.21 (2014), p. 212402. DOI: [10.1063/1.4902443](https://doi.org/10.1063/1.4902443). eprint: <https://doi.org/10.1063/1.4902443>. URL: <https://doi.org/10.1063/1.4902443>.
- [77] Rajagopalan Ramaswamy et al. “Recent advances in spin-orbit torques: Moving towards device applications”. In: *Applied Physics Reviews* 5.3 (2018), p. 031107. DOI: [10.1063/1.5041793](https://doi.org/10.1063/1.5041793). URL: <https://app.dimensions.ai/details/publication/pub.1106708349%20and%20http://arxiv.org/pdf/1808.06829>.
- [78] Jairo Sinova et al. “Spin Hall effects”. In: *Rev. Mod. Phys.* 87 (4 Oct. 2015), pp. 1213–1260. DOI: [10.1103/RevModPhys.87.1213](https://doi.org/10.1103/RevModPhys.87.1213). URL: <https://link.aps.org/doi/10.1103/RevModPhys.87.1213>.
- [79] S. Mangin et al. “Current-induced magnetization reversal in nanopillars with perpendicular anisotropy”. In: *Nature Materials* 5.3 (2006), pp. 210–215. ISSN: 1476-4660. DOI: [10.1038/nmat1595](https://doi.org/10.1038/nmat1595). URL: <https://doi.org/10.1038/nmat1595>.
- [80] Luqiao Liu et al. “Current-Induced Switching of Perpendicularly Magnetized Magnetic Layers Using Spin Torque from the Spin Hall Effect”. In: *Phys. Rev. Lett.* 109 (9 Aug. 2012), p. 096602. DOI: [10.1103/PhysRevLett.109.096602](https://doi.org/10.1103/PhysRevLett.109.096602). URL: <https://link.aps.org/doi/10.1103/PhysRevLett.109.096602>.
- [81] Can Onur Avci et al. “Magnetization switching of an MgO/Co/Pt layer by in-plane current injection”. In: *Applied Physics Letters* 100.21 (2012), p. 212404. DOI: [10.1063/1.4719677](https://doi.org/10.1063/1.4719677). eprint: <https://doi.org/10.1063/1.4719677>. URL: <https://doi.org/10.1063/1.4719677>.

- [82] Can Onur Avcı et al. “Fieldlike and antidamping spin-orbit torques in as-grown and annealed Ta/CoFeB/MgO layers”. In: *Phys. Rev. B* 89 (21 June 2014), p. 214419. DOI: [10.1103/PhysRevB.89.214419](https://doi.org/10.1103/PhysRevB.89.214419). URL: <https://link.aps.org/doi/10.1103/PhysRevB.89.214419>.
- [83] Miao Jiang et al. “Efficient full spin-orbit torque switching in a single layer of a perpendicularly magnetized single-crystalline ferromagnet”. In: *Nature Communications* 10.1 (2019), p. 2590. ISSN: 2041-1723. DOI: [10.1038/s41467-019-10553-x](https://doi.org/10.1038/s41467-019-10553-x). URL: <https://doi.org/10.1038/s41467-019-10553-x>.
- [84] K. Jabeur et al. “Compact model of a three-terminal MRAM device based on Spin Orbit Torque switching”. In: *2013 International Semiconductor Conference Dresden - Grenoble (ISCDG)*. Sept. 2013, pp. 1–4. DOI: [10.1109/ISCDG.2013.6656320](https://doi.org/10.1109/ISCDG.2013.6656320).
- [85] Murat Cubukcu et al. “Spin-orbit torque magnetization switching of a three-terminal perpendicular magnetic tunnel junction”. In: *Applied Physics Letters* 104.4 (2014), p. 042406. DOI: [10.1063/1.4863407](https://doi.org/10.1063/1.4863407). eprint: <https://doi.org/10.1063/1.4863407>. URL: <https://doi.org/10.1063/1.4863407>.
- [86] M. Cubukcu et al. “Ultra-Fast Perpendicular Spin–Orbit Torque MRAM”. In: *IEEE Transactions on Magnetism* 54.4 (Apr. 2018), pp. 1–4. ISSN: 1941-0069. DOI: [10.1109/TMAG.2017.2772185](https://doi.org/10.1109/TMAG.2017.2772185).
- [87] Shunsuke Fukami et al. “Magnetization switching by spin-orbit torque in an antiferromagnet-ferromagnet bilayer system”. In: *Nature Materials* 15 (Feb. 2016). Article, p. 535. URL: <https://doi.org/10.1038/nmat4566>.
- [88] A. Kurenkov et al. “Device-size dependence of field-free spin-orbit torque induced magnetization switching in antiferromagnet/ferromagnet structures”. In: *Applied Physics Letters* 110.9 (2017), p. 092410. DOI: [10.1063/1.4977838](https://doi.org/10.1063/1.4977838). eprint: <https://doi.org/10.1063/1.4977838>. URL: <https://doi.org/10.1063/1.4977838>.
- [89] Young-Wan Oh et al. “Field-free switching of perpendicular magnetization through spin-orbit torque in antiferromagnet/ferromagnet/oxide structures”. In: *Nature Nanotechnology* 11 (July 2016). Article, p. 878. URL: <https://doi.org/10.1038/nnano.2016.109>.
- [90] Jacob Torrejon et al. “Current-driven asymmetric magnetization switching in perpendicularly magnetized CoFeB/MgO heterostructures”. In: *Phys. Rev. B* 91 (21 June 2015), p. 214434. DOI: [10.1103/PhysRevB.91.214434](https://doi.org/10.1103/PhysRevB.91.214434). URL: <https://link.aps.org/doi/10.1103/PhysRevB.91.214434>.

- [91] Long You et al. “Switching of perpendicularly polarized nanomagnets with spin orbit torque without an external magnetic field by engineering a tilted anisotropy”. In: *Proceedings of the National Academy of Sciences* 112.33 (2015), pp. 10310–10315. ISSN: 0027-8424. DOI: [10.1073/pnas.1507474112](https://doi.org/10.1073/pnas.1507474112). eprint: <https://www.pnas.org/content/112/33/10310.full.pdf>. URL: <https://www.pnas.org/content/112/33/10310>.
- [92] Zhaohao Wang et al. “Field-free spin–orbit-torque switching of perpendicular magnetization aided by uniaxial shape anisotropy”. In: *Nanotechnology* 30.37 (June 2019), p. 375202. DOI: [10.1088/1361-6528/ab2831](https://doi.org/10.1088/1361-6528/ab2831).
- [93] R.L. de Orio et al. “Robust magnetic field-free switching of a perpendicularly magnetized free layer for SOT-MRAM”. In: *Solid-State Electronics* (2019), p. 107730. ISSN: 0038-1101. DOI: <https://doi.org/10.1016/j.sse.2019.107730>. URL: <http://www.sciencedirect.com/science/article/pii/S0038110119307336>.
- [94] Viktor Sverdlov, Alexander Makarov, and Siegfried Selberherr. “Two-pulse subns switching scheme for advanced spin-orbit torque MRAM”. In: *Solid-State Electronics* 155 (2019). Selected Papers from the Future Trends in Microelectronics (FTM-2018) Workshop, pp. 49–56. ISSN: 0038-1101. DOI: <https://doi.org/10.1016/j.sse.2019.03.010>. URL: <http://www.sciencedirect.com/science/article/pii/S0038110118305070>.
- [95] Guoqiang Yu et al. “Switching of perpendicular magnetization by spin-orbit torques in the absence of external magnetic fields”. In: *Nature Nanotechnology* 9.7 (2014), pp. 548–554. ISSN: 1748-3395. DOI: [10.1038/nnano.2014.94](https://doi.org/10.1038/nnano.2014.94). URL: <https://doi.org/10.1038/nnano.2014.94>.
- [96] Baoshan Cui et al. “Field-Free Spin–Orbit Torque Switching of Perpendicular Magnetization by the Rashba Interface”. In: *ACS Applied Materials & Interfaces* 11.42 (2019). PMID: 31603641, pp. 39369–39375. DOI: [10.1021/acsami.9b13622](https://doi.org/10.1021/acsami.9b13622). eprint: <https://doi.org/10.1021/acsami.9b13622>. URL: <https://doi.org/10.1021/acsami.9b13622>.
- [97] E. A. Tremsina, N. Roschewsky, and S. Salahuddin. “Micromagnetic analysis and optimization of spin-orbit torque switching processes in synthetic antiferromagnets”. In: *Journal of Applied Physics* 126.16 (2019), p. 163905. DOI: [10.1063/1.5121167](https://doi.org/10.1063/1.5121167). eprint: <https://doi.org/10.1063/1.5121167>. URL: <https://doi.org/10.1063/1.5121167>.
- [98] Yong-Chang Lau et al. “Spin-orbit torque switching without an external field using interlayer exchange coupling”. In: *Nature Nanotechnology* 11.9 (2016), pp. 758–762. ISSN: 1748-3395. DOI: [10.1038/nnano.2016.84](https://doi.org/10.1038/nnano.2016.84). URL: <https://doi.org/10.1038/nnano.2016.84>.

- [99] Long You et al. “Switching of perpendicularly polarized nanomagnets with spin orbit torque without an external magnetic field by engineering a tilted anisotropy”. In: *Proceedings of the National Academy of Sciences* 112.33 (2015), pp. 10310–10315. ISSN: 0027-8424. DOI: [10.1073/pnas.1507474112](https://doi.org/10.1073/pnas.1507474112). eprint: <https://www.pnas.org/content/112/33/10310.full.pdf>. URL: <https://www.pnas.org/content/112/33/10310>.
- [100] Neil Murray et al. “Field-free spin-orbit torque switching through domain wall motion”. In: *Phys. Rev. B* 100 (10 Sept. 2019), p. 104441. DOI: [10.1103/PhysRevB.100.104441](https://doi.org/10.1103/PhysRevB.100.104441). URL: <https://link.aps.org/doi/10.1103/PhysRevB.100.104441>.
- [101] W. J. Kong et al. “Spin-orbit torque switching in a T-type magnetic configuration with current orthogonal to easy axes”. In: *Nature Communications* 10.1 (2019), p. 233. ISSN: 2041-1723. DOI: [10.1038/s41467-018-08181-y](https://doi.org/10.1038/s41467-018-08181-y). URL: <https://doi.org/10.1038/s41467-018-08181-y>.
- [102] Xiaoguang Li et al. “Ultrafast field-free magnetization switching using bi-directional spin Hall current and antiferromagnetic interlayer exchange”. In: *Applied Physics Letters* 114.1 (2019), p. 012403. DOI: [10.1063/1.5063423](https://doi.org/10.1063/1.5063423). eprint: <https://doi.org/10.1063/1.5063423>. URL: <https://doi.org/10.1063/1.5063423>.
- [103] Stanisław Łazarski et al. “Field-Free Spin-Orbit-Torque Switching in Co/Pt/Co Multilayer with Mixed Magnetic Anisotropies”. In: *Phys. Rev. Applied* 12 (1 July 2019), p. 014006. DOI: [10.1103/PhysRevApplied.12.014006](https://doi.org/10.1103/PhysRevApplied.12.014006). URL: <https://link.aps.org/doi/10.1103/PhysRevApplied.12.014006>.
- [104] D. Weller and Moser A. “Thermal effect limits in ultrahigh-density magnetic recording”. In: *IEEE Transactions on Magnetics* 35.6 (Nov. 1999), pp. 4423–4439. ISSN: 1941-0069. DOI: [10.1109/20.809134](https://doi.org/10.1109/20.809134).
- [105] A. Hubert, R. Schäfer, and A. Rudolf Schafer. *Magnetic Domains: The Analysis of Magnetic Microstructures*. Springer, 1998. ISBN: 9783540641087. URL: <https://books.google.it/books?id=pBE421LYs-MC>.
- [106] A.R. Fert. “Magnetic and Transport Properties of Metallic Multilayers”. In: *Metallic Multilayers*. Vol. 59. Materials Science Forum. Trans Tech Publications Ltd, Jan. 1991, pp. 439–480. DOI: [10.4028/www.scientific.net/MSF.59-60.439](https://doi.org/10.4028/www.scientific.net/MSF.59-60.439).
- [107] S. Pizzini et al. “Chirality-Induced Asymmetric Magnetic Nucleation in Pt/Co/AlO_x Ultrathin Microstructures”. In: *Phys. Rev. Lett.* 113 (4 July 2014), p. 047203. DOI: [10.1103/PhysRevLett.113.047203](https://doi.org/10.1103/PhysRevLett.113.047203). URL: <https://link.aps.org/doi/10.1103/PhysRevLett.113.047203>.

-
- [108] J. Sampaio et al. “Disruptive effect of Dzyaloshinskii-Moriya interaction on the magnetic memory cell performance”. In: *Applied Physics Letters* 108.11 (2016), p. 112403. DOI: [10 . 1063 / 1 . 4944419](https://doi.org/10.1063/1.4944419). eprint: <https://doi.org/10.1063/1.4944419>. URL: <https://doi.org/10.1063/1.4944419>.
- [109] Daniele Gastaldo et al. “Impact of Dzyaloshinskii-Moriya interactions on the thermal stability factor of heavy metal/magnetic metal/oxide based nano-pillars”. In: *Journal of Applied Physics* 126.10 (2019), p. 103905. DOI: [10 . 1063 / 1 . 5109484](https://doi.org/10.1063/1.5109484). eprint: <https://doi.org/10.1063/1.5109484>. URL: <https://doi.org/10.1063/1.5109484>.
- [110] Eduardo Martinez et al. “Universal chiral-triggered magnetization switching in confined nanodots”. In: *Scientific Reports* 5.1 (2015), p. 10156. ISSN: 2045-2322. DOI: [10.1038/srep10156](https://doi.org/10.1038/srep10156). URL: <https://doi.org/10.1038/srep10156>.
- [111] G. Finocchio et al. “Switching of a single ferromagnetic layer driven by spin Hall effect”. In: *Applied Physics Letters* 102.21 (2013), p. 212410. DOI: [10 . 1063 / 1 . 4808092](https://doi.org/10.1063/1.4808092). eprint: <https://doi.org/10.1063/1.4808092>. URL: <https://doi.org/10.1063/1.4808092>.
- [112] Yongxi Ou et al. “Strong spin Hall effect in the antiferromagnet PtMn”. In: *Phys. Rev. B* 93 (22 June 2016), p. 220405. DOI: [10 . 1103 / PhysRevB . 93 . 220405](https://link.aps.org/doi/10.1103/PhysRevB.93.220405). URL: <https://link.aps.org/doi/10.1103/PhysRevB.93.220405>.
- [113] E. Derunova et al. “Giant intrinsic spin Hall effect in W₃Ta and other A15 superconductors”. In: *Science Advances* 5.4 (2019). DOI: [10 . 1126 / sciadv . aav8575](https://doi.org/10.1126/sciadv.aav8575). eprint: <https://advances.sciencemag.org/content/5/4/eaav8575.full.pdf>. URL: <https://advances.sciencemag.org/content/5/4/eaav8575>.
- [114] Kai-Uwe Demasius et al. “Enhanced spin-orbit torques by oxygen incorporation in tungsten films”. In: *Nature Communications* 7.1 (2016), p. 10644. ISSN: 2041-1723. DOI: [10 . 1038 / ncomms10644](https://doi.org/10.1038/ncomms10644). URL: <https://doi.org/10.1038/ncomms10644>.
- [115] Qiang Hao, Wenzhe Chen, and Gang Xiao. “Beta (β) tungsten thin films: Structure, electron transport, and giant spin Hall effect”. In: *Applied Physics Letters* 106.18 (2015), p. 182403. DOI: [10 . 1063 / 1 . 4919867](https://doi.org/10.1063/1.4919867). eprint: <https://doi.org/10.1063/1.4919867>. URL: <https://doi.org/10.1063/1.4919867>.
- [116] Lijun Zhu, Daniel. C. Ralph, and Robert A. Buhrman. “Highly Efficient Spin-Current Generation by the Spin Hall Effect in Au_{1-x}Pt_x”. In: *Phys. Rev. Applied* 10 (3 Sept. 2018), p. 031001. DOI: [10 . 1103 / PhysRevApplied . 10 . 031001](https://link.aps.org/doi/10.1103/PhysRevApplied.10.031001). URL: <https://link.aps.org/doi/10.1103/PhysRevApplied.10.031001>.

This Ph.D. thesis has been typeset by means of the \TeX -system facilities. The typesetting engine was Lua \LaTeX . The document class was `toptesi`, by Claudio Beccari, with option `tipotesi=scudo`. This class is available in every up-to-date and complete \TeX -system installation.